PNAS RESEARCH ARTICLE | EARTH, ATMOSPHERIC, AND PLANETARY SCIENCES

Plate motion and a dipolar geomagnetic field at 3.25 Ga

Alec R. Brenner[a,1], Roger R. Fu[a], Andrew R. C. Kylander-Clark[b], George J. Hudak[c], and Bradford J. Foley[d]

Edited by Lisa Tauxe, University of California San Diego, La Jolla, CA; received June 14, 2022; accepted September 21, 2022

The paleomagnetic record is an archive of Earth's geophysical history, informing reconstructions of ancient plate motions and probing the core via the geodynamo. We report a robust 3.25-billion-year-old (Ga) paleomagnetic pole from the East Pilbara Craton, Western Australia. Together with previous results from the East Pilbara between 3.34 and 3.18 Ga, this pole enables the oldest reconstruction of time-resolved lithospheric motions, documenting 160 My of both latitudinal drift and rotation at rates of at least 0.55°/My. Motions of this style, rate, and duration are difficult to reconcile with true polar wander or stagnant-lid geodynamics, arguing strongly for mobile-lid geodynamics by 3.25 Ga. Additionally, this pole includes the oldest documented geomagnetic reversal, reflecting a stably dipolar, core-generated Archean dynamo.

Archean geodynamics | plate tectonics | geodynamo | hydrothermal alteration | paleomagnetism

Significance

The modern Earth is geologically dynamic. Convection in its rocky mantle drives plate tectonics that reshapes its surface, and currents inside its metallic core generate a strong planetary magnetic field. However, it is uncertain whether these processes had begun to shape Earth in its deep past. Our measurements of magnetic signals preserved in 3.25-billion-year-old rocks provide the earliest quantitative evidence of both rapidly moving crust—a hallmark of plate tectonics—and a stable ancient magnetic field that episodically alternated polarity. These observations suggest that the early Earth was remarkably geologically mature from its surface to its deep interior, potentially contributing to stable surface conditions for the evolution of early life.

Plate tectonics describes the partitioning of the Earth's lithosphere into multiple mobile plates. The horizontal and vertical motions of these plates exert fundamental controls on Earth's surface and interior evolution. Despite its importance, it is unclear whether plate tectonics operated in Earth's deep past (1), particularly during the Archean Eon (4.0–2.5 billion years ago [Ga]), when the first life arose and evolved. What little evidence survives of Earth's earliest geodynamics resides in cratons, which are the metamorphosed remnants of the Archean crust.

Quantifying past cratonic motions may reveal whether the early Earth hosted "mobile-lid" plate tectonics or alternative "sluggish-" or "stagnant-lid" regimes (1). Ninety percent of modern plate motion rates, expressed as lateral speeds, fall within ∼0.1–1.5°/My (2) and locally can attain rates over 9°/My (3). Meanwhile, stagnant-lid regimes, in which the lithosphere acts as a single global plate that must rotate all at once, are expected to suppress lithospheric motion to order ∼0.1°/My typically and <0.3–1.5°/My in extreme scenarios (*SI Appendix*, *Appendix S5*).

Paleomagnetism, which enables the construction of the apparent polar wander (APW) path of the ancient geomagnetic pole relative to a given crustal block, is the only tool that can quantitatively reconstruct the motions of cratons through time, thereby inferring the ancient Earth's tectonic regime. The sparse Archean rock record has thus far yielded no pre-2.8 Ga APW paths with sufficient temporal resolution to discriminate between these regimes [see review in Brenner et al. (4)]. The East Pilbara Craton of Western Australia (Fig. 1*A*) hosts the most complete pre-2.8 Ga paleomagnetic record (*SI Appendix*, *Appendix S2*), with robust paleomagnetic poles at 3.47 Ga ["DFM" (5)], 3.34 Ga ["EBm" (6)], and 3.18 Ga ["HEBh" (4)]. Due to the slow minimum drift rate and the possibility of true polar wander (TPW), it is uncertain whether mobile- or stagnant-lid processes drove a major latitudinal shift between poles EBm and HEBh (4).

The dynamics of Earth's deep interior during the Archean are likewise uncertain. The inner core had likely not begun to crystallize, eliminating the major driving power source of today's dynamo. Even so, rocks as old as ∼3.5 Ga carry coherent magnetizations, implying a stable local magnetic field (7). This has led to several proposals of exotic dynamo driving mechanisms, including light-element exsolution and a silicate mantle-hosted dynamo (8, 9).

To expand the pre-2.8 Ga paleomagnetic record, we sampled weakly metamorphosed (∼330 °C) komatiitic lavas of the ∼3.275–3.249 Ga Kunagunarrina Formation within the Soanesville Syncline (SVS) of the East Pilbara Craton (Fig. 1 and *SI Appendix*, Fig. S1), taking 117 samples from 11 cooling units (i.e., paleomagnetic "sites") across three localities (KUA, KUB, and KUT). We recovered a paleomagnetic pole and conducted reversal, fold, and conglomerate tests as well as micromagnetic imaging and U-Pb titanite petrochronology to constrain its age of magnetization.

Paleomagnetic Directions and Their Origins

Stepwise alternating field and thermal demagnetization up to 590 °C on all specimens revealed four components of ancient magnetization with unblocking temperatures

Author affiliations: [a]Department of Earth and Planetary Sciences, Harvard University, Cambridge, MA 02138; [b]Department of Earth Science, University of California, Santa Barbara, CA 93106; [c]Natural Resources Research Institute, University of Minnesota, Duluth, MN 55812; and [d]Department of Geosciences, The Pennsylvania State University, State College, PA 16802

Author contributions: A.R.B. led the study with interpretive and analytical contributions from R.R.F., who played a supervisory role; A.R.B. and R.R.F. conducted field sampling; A.R.B. performed paleomagnetic analyses; A.R.C.K.-C. performed geochronology analyses and interpreted them along with A.R.B. and R.R.F.; A.R.B., R.R.F., and G.J.H. contributed to alteration system interpretations; A.R.B., R.R.F., and B.J.F. contributed to scaling derivations for stagnant-lid motions; and A.R.B. wrote the paper with interpretive input from all authors.

The authors declare no competing interest.

This article is a PNAS Direct Submission.

[1]To whom correspondence may be addressed. Email: alecbrenner@g.harvard.edu.

This article contains supporting information online at http://www.pnas.org/lookup/suppl/doi:10.1073/pnas.2210258119/-/DCSupplemental.

Published October 24, 2022.

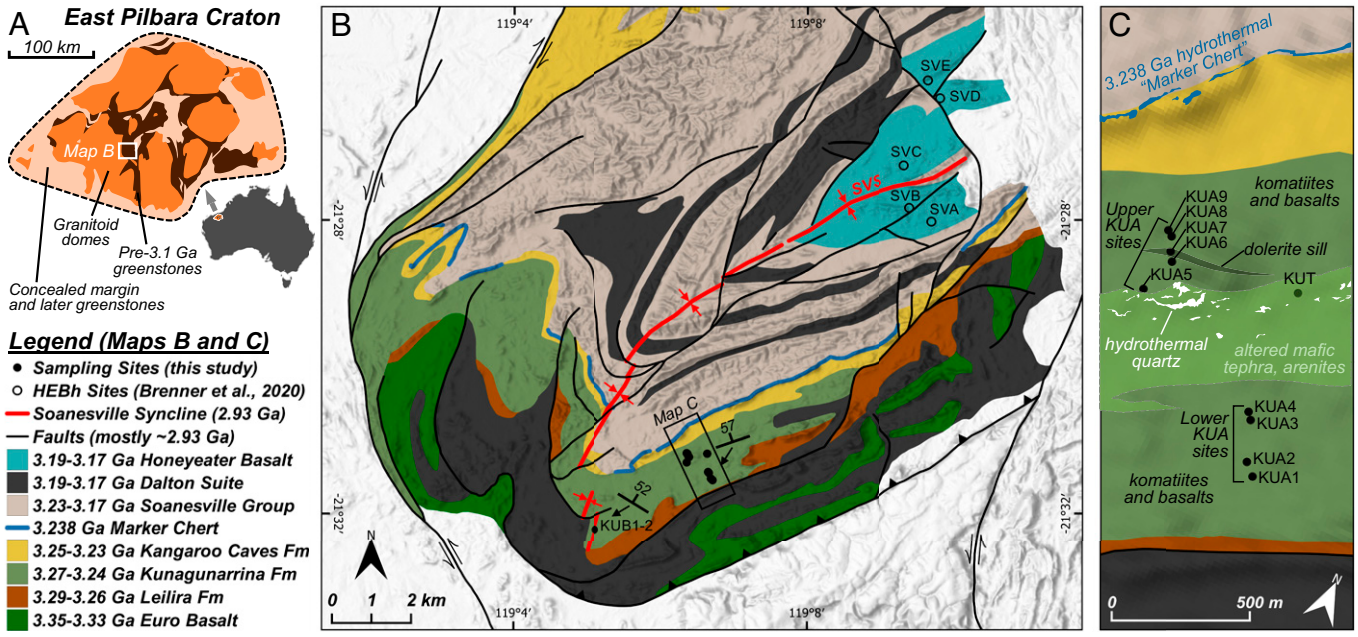

Fig. 1. Map of the Soanesville Syncline with sampling sites. (*A*) Reference map of the East Pilbara Craton. (*B*) The Kunagunarrina Formation (medium green) sampled in this study (filled points) is well preserved along the southeast limb of the Soanesville Syncline (SVS), along with the overlying Honeyeater Basalt (blue-green) from which the HEBh paleomagnetic pole was measured [hollow points (4)]. (*C*) Map details sites from locality KUA, as well as a dolerite sill (sampled at site KUA7) and a prominent marker bed of komatiitic volcaniclastic rocks (sampled at locality KUT). Note that our sampling at KUA is grouped into "Lower" and "Upper" groups of sites within the volcanic stratigraphy. Also noteworthy are two horizons associated with hydrothermalism, one in the central Kunagunarrina Formation (white) and another called the "Marker Chert" capping the overlying Kangaroo Caves Formation (medium blue).

between 75 and 580 °C (Fig. 2 *A*–*C* and *SI Appendix*, Figs. S2*A* and S3; see *SI Appendix*, Table S1 for component directions and statistics and *SI Appendix*, *Appendix S1* for detailed interpretations). The first three thermal demagnetization components ("L2," "M," and "M2") can be tied to resetting events at ∼0.54, ∼2.2–1.7, and ∼2.78 Ga, respectively, based on paleopole comparisons (10–12) and failing fold tests (L2 and M components only; *SI Appendix*, Table S1).

The final component, termed "H", is present in 44 of 117 samples as an origin-trending, site-coherent magnetization unblocking above ∼500 °C in 9 out of 11 sites (Fig. 2 and *SI Appendix*, Table S1). Site-mean directions of this component converge following correction for local structural tilt and rotation, passing a fold test (13) and indicating that the H magnetization predates 2.93 Ga folding of the SVS (Fig. 3 and *SI Appendix*, Fig. S2*B*; see *SI Appendix*, *Appendix S3* for details of regional structure). Additionally, H components from sites KUA5-9 ("Upper KUA") are antipodal within 20° to those from all other sites, statistically consistent with antipodality. While the number of sites limits the statistical power of the reversal test ["indeterminate" in the classification of McFadden et al. (14); see *SI Appendix*, *Appendix S3.2*], the proximity to antipodal directions, similarity in thermal demagnetization behavior, and lithostratigraphic, petrographic, and geochronological context of the H component (see below) demonstrate that a 3.25-Ga reversal is the only probable explanation for the polarity groups, implying that the H magnetization was acquired shortly after eruption onto the seafloor.

Micromagnetic examination independently verifies these paleomagnetic field tests and identifies the mechanism of magnetization (*SI Appendix*, Figs. S7–11 and *Appendix S4*). Optical, Raman, and quantum diamond microscopy (QDM) demonstrate that major ferromagnetic grain populations—nearly all magnetites—are ubiquitously derived from replacement of primary minerals and precipitation of new minerals via hydration and Fe mobilization during multistage fluid flow. These reactions included recrystallization of primary titanomagnetite grains and dendrites (*SI Appendix*, Figs. S8 and S12 *B* and *C*), Fe exchange with magmatic Cr-spinels (*SI Appendix*, Fig. S12*D*), and hydration/mobile element exchange with primary ferromagnesian silicates (e.g., olivine, *SI Appendix*, Fig. S12*E*; orthopyroxene, *SI Appendix*, Fig. S12*F*; and volcanic glass). In void spaces (vesicles and fractures), magnetite is closely associated with infill phases, such as calcite after Ca-zeolites and anorthite, which occasionally preserve a complex prograde infill and replacement sequence (*SI Appendix*, Figs. S9–S12). Notably, magnetite grains associated with one such vesicular infill stage exhibit thermal unblocking behavior identical to that of the H component in the bulk sample, robustly indicating that these grains contribute to the H magnetization (Fig. 2*C* and *SI Appendix*, Fig. S10). Later stages in the hydrothermal alteration sequence precipitated many secondary minerals, including the titanites targeted for geochronology (see below) and carbonaceous matter that records peak maturation temperatures between 300 and 330 °C (*SI Appendix*, Fig. S7 *K* and *L*).

Titanite is a suitable mineral for U-Pb petrochronology, so titanite postdating the magnetite crystallization thus offers an opportunity to establish a minimum age for the H component. We performed in situ laser ablation U-Pb analyses of 120 titanite grains formed during late albitization reactions, 93 of which passed selection criteria, defining an array of U-Pb compositions (*SI Appendix*, *Appendix S4.5* and Fig. S11). Excluding analyses affected by minor postcrystallization Pb loss, the remaining data define a lower-intercept age of 3.223 ± 0.023 Ga (2σ).

These analyses directly associate the H component remanence and its carrier minerals to early hydrothermal alteration bracketed by 3.275–3.249 Ga Kunagunarrina eruption and late alteration at 3.223 ± 0.023 Ga. Given the history of mineralization in the East Pilbara, the emplacement of nearby granitic intrusions of the Cleland Supersuite at 3.257–3.235 Ga are most likely responsible for this alteration (15, 16). This voluminous plutonism resulted in extensive metamorphism and subseafloor hydrothermal circulation, which notably formed major

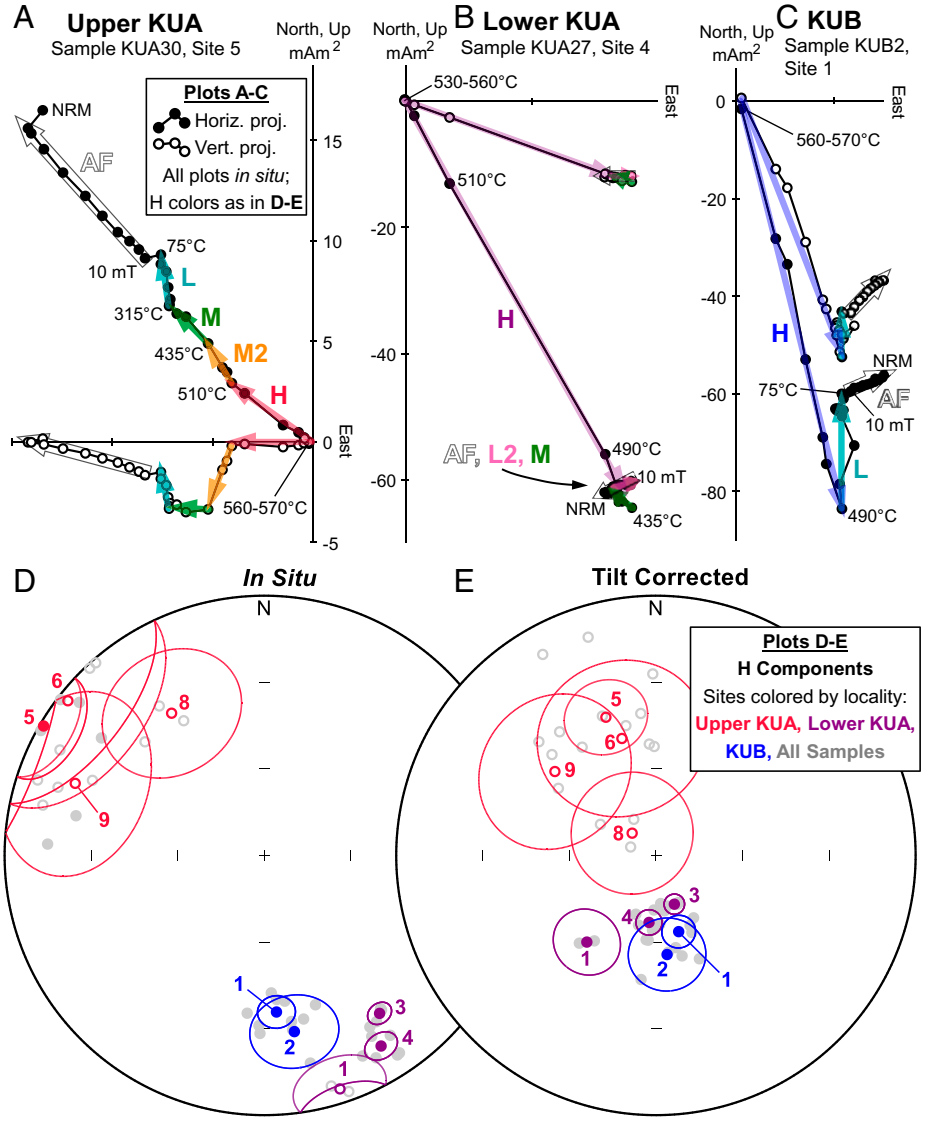

Fig. 2. Paleomagnetic results. (*A–C*) Orthographic plots of demagnetization (in situ coordinates) show multiple magnetization components (arrows). Magnetites hosting the H component in *C* have been directly identified by QDM mapping (*SI Appendix*, Figs. S9 and S10). (*D* and *E*) Stereonets of the highest-temperature "H" component. Site means converge upon tilt correction, indicating a prefolding H magnetization (*SI Appendix*, Fig. S2*B*). Site means from the uppermost sites (red) are antipodal to those below, reflecting a geomagnetic reversal and an H magnetization acquired shortly after deposition.

volcanic-hosted massive sulfide (VHMS) deposits dated to 3.265–3.235 Ga [Fig. 3 and *SI Appendix*, Fig. S1 and *Appendix S4* (15–17)]. These deposits are hosted within "exhalite" horizons, representing the seafloor expressions of pulses of hydrothermal circulation beneath the paleo-seafloor and above the driving intrusions (18). These pulses have durations comparable to the cooling timescale of the intrusions that drive them, driving mineral alteration for up to thousands to hundreds of thousands of years (19, 20). This is long enough that data from a suite of geographically separated sites that were altered (and thus magnetized) at different times by the same protracted VHMS circulation event can be averaged together to sample paleosecular variation (PSV) and record the time-averaged field during alteration. This is supported by the low within-site but higher between-site scatter of our directional data, both within each polarity group of sites and in the compilation of all sites (*SI Appendix*, *Appendix S3.3*). Two stratigraphic horizons in our study area contain deposits of hydrothermal quartz typical of this style of hydrothermal activity, one just above our lowermost "R" polarity sites, and another overlying our uppermost "N" polarity sites (Fig. 1 and *SI Appendix*, Fig. S1). The latter is the 3.241–3.235 Ga "Marker Chert" (Figs. 1 and 3 and *SI Appendix*, Fig. S1), a regionally traceable seafloor exhalative chert horizon associated with intrusion of the Strelley Laccolith north of our study area (21, 22). Since each of these two hydrothermal events cap a lava package hosting a magnetization antipodal to that of the other package, these events, separated by up to ~20 My given the timespan of nearby Cleland Supersuite plutonism, were likely each responsible for imparting one polarity of the reversing thermochemical remanent magnetization that we document.

In brief, the combination of a passing fold test, a probable reversal, magnetic microscopy, and titanite petrochronology shows that the H component is a TCRM acquired during 3.265–3.235 Ga sea-floor alteration shortly after lava emplacement (16, 17, 21). The H magnetization thus defines an ~3.25-Ga paleopole from the East Pilbara (λ, ϕ = 65.6°S, 143.7°E; α_{95} = 16.5°; n = 9; paleolatitude λ_p = 42.7 ± 13.1°), which we term "KUH-R" for "Kunagunarrina high-temperature – reversed" (Fig. 4 and *SI Appendix*, Table S1). Direct comparison to other

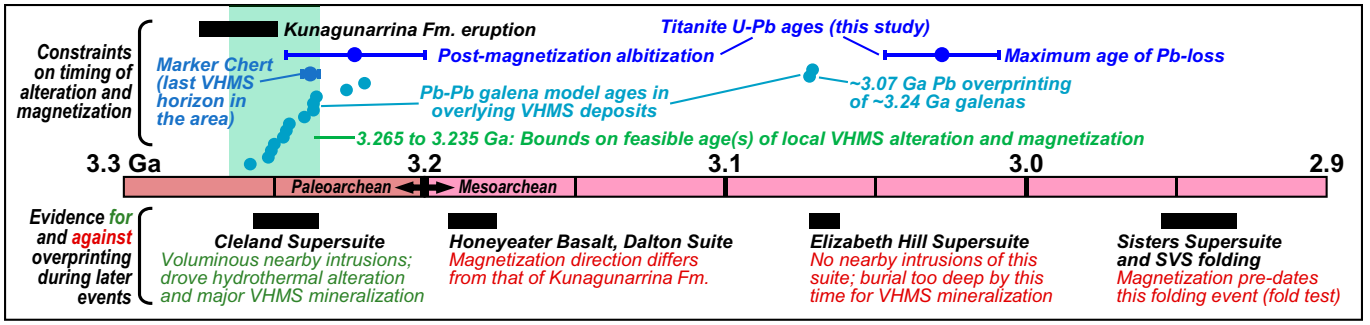

Fig. 3. Constraints on the timing of magnetization. The H component was acquired during seafloor hydrothermal alteration between >3.223 ± 0.023 Ga (U-Pb titanite age of postmagnetization albitization in our samples, *SI Appendix*, Fig. S11 and *Appendix S4.5*) and <~3.275–3.249 Ga [age range of Kunagunarrina Formation eruption from U-Pb zircon ages in the Kunagunarrina and Kangaroo Caves Formations (15, 21, 48)]. This matches the range of U-Pb zircon crystallization ages measured from the nearest granitic intrusions of the Cleland Supersuite from 3.257 to 3.235 Ga (15) and dates from their associated volcanic-hosted massive sulfide (VHMS) hydrothermal mineralization (16, 17, 21). This mineralization is bracketed to between 3.265 Ga, the upper bound on the oldest documented age of the VHMS deposits themselves [$3.257^{+0.008}_{-0.006}$ Ga Pb-Pb galena model age (17)], and 3.235 Ga, the lower bound on the age of the epithermal Marker Chert that overlies our samples [the youngest permissible U-Pb zircon age of the 3.238 ± 0.003 Ga inner-phase Strelley Granite that drove the VHMS mineralization, as well as the mean U-Pb zircon age of a 3.235 ± 0.003 Ga rhyolite that immediately overlies the epithermal horizon (21)]. The H magnetization escaped full overprinting during all later events, including those preceding 2.93-Ga folding that is the basis of our fold test (constrained by U-Pb zircon dates from syn-kinematic granitoids (22, 49)). Thus, the H component dates to VHMS mineralization between 3.265 and 3.235 Ga.

pre-2.8 Ga poles from the Pilbara craton requires correction for an ∼2.93-Ga vertical-axis rotation of the SVS block relative to the rest of the East Pilbara (*SI Appendix*, Fig. S5 Table S1, and *Appendix S2.2*). This rotation is constrained to between 0° (no rotation) and 70° clockwise by the curvature of the fault bounding the SVS to the west (*SI Appendix*, Fig. S5). We consider the full permissible range of this rotation below, noting that it does not affect the relative positions of poles HEBh and KUH-R, since both were sampled from within the SVS.

Surface Motions and Geophysical Drivers

Taken together, poles EBm, KUH-R, and HEBh resolve the East Pilbara APW path at ≤95-My intervals, substantially constraining the range of possible motions between 3.34 and 3.18 Ga and representing the oldest such record available. Due to reversal-state ambiguities between the poles and possible block rotation of the SVS shortly preceding folding at 2.93 Ga, several APW paths and corresponding motion reconstructions are possible. Below, we construct the APW path and reconstruction that minimizes the intervening motion of the East Pilbara (Fig. 4), noting that all other permissible cases imply faster motions, in most cases exceeding 1°/My. For detailed treatment of these less-likely scenarios, see *SI Appendix*, *Appendix S2* and Fig. S6.

In our conservative, preferred scenario, pole EBm samples the opposing reversal state relative to HEBh and KUH-R. Since the positions of SVS poles KUH-R and HEBh relative to pole EBm also depend on how much structural block rotation (between 0° and 70° clockwise) the SVS area experienced, we prescribe the magnitude of this rotation (20° clockwise) that minimizes the distance (and therefore motion) between poles EBm and KUH-R (Fig. 4*A*). These conservative assumptions yield a two-stage reconstruction: first, from 3.34 to 3.25 Ga (∼95 My), the East Pilbara drifted latitudinally at an average rate of $0.55^{+0.19}_{-0.16}$ °/My with no resolvable vertical-axis rotation (Fig. 4*B*). Second, from 3.25 to 3.18 Ga, the East Pilbara rotated counterclockwise by $0.55^{+0.46}_{-0.38}$ °/My with no resolvable latitudinal motion (Fig. 4*B*). We emphasize that, while this reconstruction and its motion rates are not unique—since others are possible due to uncertain reversal states and structure-forming events—the rates are the slowest allowable given these uncertainties, meaning the East Pilbara experienced horizontal motions at least as rapid as those presented above.

Reconciling these ∼0.55°/My rates with permissible motions in a stagnant-lid regime is challenging, especially over a 95-My interval. Lithospheric net rotation has not exceeded 0.75°/My for the last 200 My and averages much less over tens of My timescales [Fig. 5 and *SI Appendix*, *Appendix S5* (23)]. The net rotation speed limit of an Archean stagnant lid is expected to have been less than or comparable to modern rates due to less-efficient lithospheric coupling to mantle flow (*SI Appendix*, *Appendix S5*). However, achieving this speed limit would have simultaneously required a "modern-like" lithospheric structure, a very hot Archean mantle, and a contrived mantle flow pattern that would not have persisted for tens of My, making net rotation an unlikely candidate to drive the observed 0.55°/My motions (Fig. 5 and *SI Appendix*, Fig. S13 and *Appendix S5*). An alternative type of non-plate-tectonic surface motion called TPW requires a Euler pole on the paleoequator, 90° away from the paleopole, thus resulting in paleopoles spread along a great circle (24). The most likely reconstructions all suggest the East Pilbara rotated in place from 3.25 to 3.18 Ga, implying a midlatitude Euler pole. That said, it is technically possible to ascribe all observed motions to two successive TPW events, one during each of the intervals between poles. However, all permissible APW paths would require that the successive TPW rotations were about axes 48° to 90° apart in longitude. In contrast, previously documented examples of interpreted successive TPW events have all involved Euler poles separated by <25° of longitude due to persistence in the geoid shape (25). Therefore, even though TPW may have contributed to some of the motion of the East Pilbara, it is highly unlikely that TPW drove all observed motions.

On the other hand, all observed motions are fully consistent with mobile-lid tectonic processes. For instance, plate rotations often arise today within oroclines (26, 27) and on microplates captured between complex convergent boundaries and associated back-arc rifts (3). One such system contains the Woodlark and Manus Basins on the northeastern Australian plate margin, featuring 0.6°/My latitudinal motion and up to 9°/My rotations (3). These similarities may suggest a tectonically complex convergent margin setting for the East Pilbara around 3.2 Ga, consistent with the craton's stratigraphy and previous assertions of rift (28) and arc (29) settings during this time, although other tectonic settings can host similar motions.

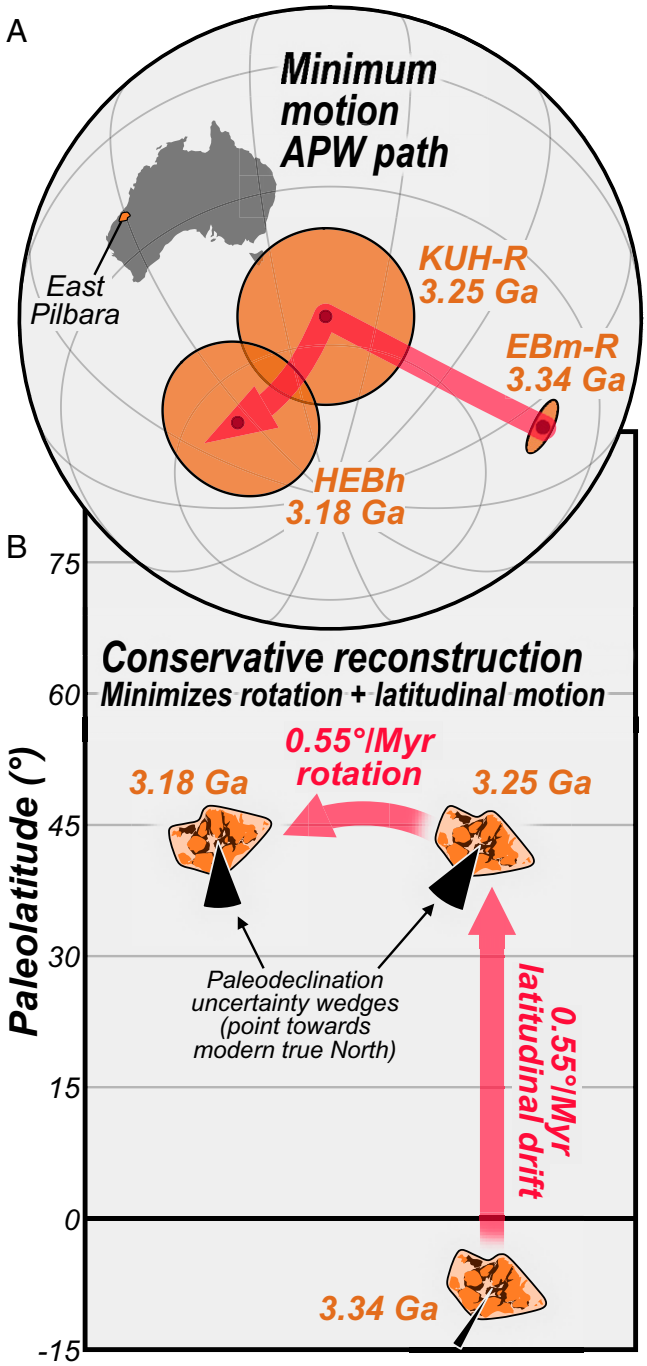

Fig. 4. Minimum-motion reconstruction of the East Pilbara from ~3.34 to 3.18 Ga. (*A*) Apparent polar wander (APW) path constructed to minimize implied motions. Pole EBm samples the opposing reversal state relative to KUH-R and HEBh, and the SVS block is assumed to have rotated 20° clockwise, implying no rotational motion between 3.34 and 3.25 Ga (*SI Appendix, Appendix S2*). (*B*) The simplest motion reconstruction based on this path, starting with 95 My of $0.55^{+0.19}_{-0.16}$ °/My latitudinal motion followed by 65 My of $0.55^{+0.46}_{-0.38}$ °/My rotation. Other reconstructions are possible but require faster motions, most >1°/My; see *SI Appendix*, Fig. S6 for these less-plausible cases.

In summary, the East Pilbara's paleomagnetic record demonstrates that, by ~3.25 Ga, geodynamic processes were driving rapid (≥0.55°/My or ≥6.1 cm/y) lithospheric motions that were sustained for tens of My. Differential motion within a mobile lid is the only mechanism that remains compatible with this record without invoking exceptional circumstances. That said, our observations do not require that modern-like plate tectonics sensu stricto were operating by 3.3 Ga, as sluggish lid, episodically mobile lid, and a variety of transitional regimes may all produce differential surface motions (1). We therefore pose these observations as a challenge to nonuniformitarian geodynamic models of the early Earth, which should seek to explain motions of this rate and duration.

Archean Geodynamo Implications

The apparent polarity reversal provides further insights into early Earth's deep interior. The polarities depart from antipodality by 19.9° with 10.1° of inclination mismatch. However, these "asymmetries" are not resolvably greater than zero within uncertainty and thus remain compatible with a reversal of a geocentric axial dipole (GAD) paleofield. Further, we can test the degree to which departures from this dipolar paleofield are statistically compatible with our polarity observations. This test consists of two constraints on field geometry. First, because stronger nonreversing axial quadrupole ($G2$) and octupole ($G3$) field components relative to the axial dipole result in more reversal asymmetry, the observed inclination asymmetry between polarities can constrain the relative moment of these higher-order geomagnetic field components (*SI Appendix*, Fig. S4*A*). Second, the PSV dispersion of our paleomagnetic directions can be used to estimate the dipolarity of the geomagnetic field when coupled with the empirical dipolarity-dispersion relationship identified by Biggin et al. (30) (*SI Appendix*, Fig. S4*C*). Combining these two constraints permits the calculation of confidence regions in $G2$–$G3$ space that delineate

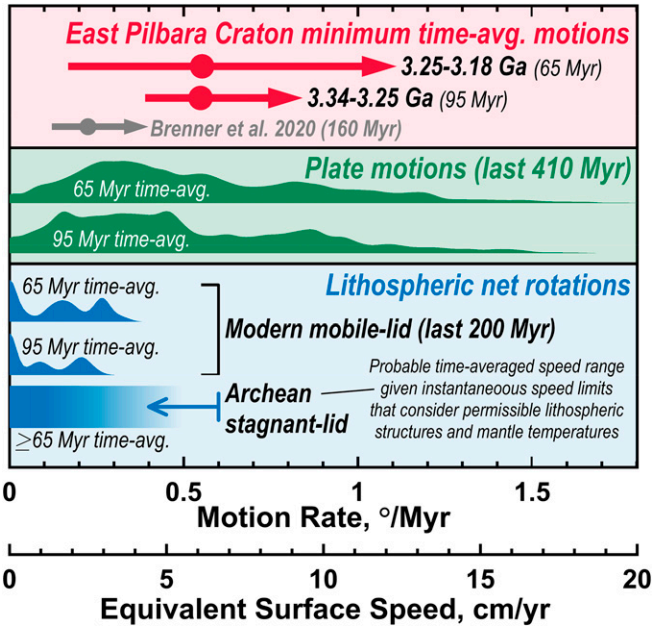

Fig. 5. Comparison of measured East Pilbara motion rates with those of candidate drivers. Rates are expressed in both degrees/My and the equivalent value in cm/y, assuming measurement 90° away from the motion's Euler pole. Measured rates (red, 2σ CIs) are lower bounds time averaged over the indicated intervals, documenting substantial motions between 3.34 and 3.18 Ga (see text and Fig. 4). These are comparable to time-averaged recent plate motions [green distributions (2)] but faster than time-averaged recent net rotations [blue distributions (50)] and expected net rotations of an Archean stagnant lid (blue shaded bar and arrow; *SI Appendix, Appendix S5*). The arrow indicates the expected highest permissible time-averaged rate of stagnant-lid net rotation in a perfect but unrealistic driving scenario, which we calculate as 40% of the expected highest instantaneous rate. This is based on the observation that the fastest 65-My-time-averaged net rotation rate on the modern Earth does not exceed 40% of the theoretical fastest permissible instantaneous rate (*SI Appendix, Appendix S5.3*). Net rotations are therefore most likely insufficient to explain the measured motions, suggesting a plate tectonic driver.

statistically permissible deviations from a pure GAD field given our dataset (Fig. 6 and *SI Appendix*, Fig. S4*D*).

Reproducing the observed polarity inclinations exactly without including their uncertainties would require only a nonreversing axial octupole with 15% of the dipole moment, within the range of estimated field dipolarity since 2.7 Ga [Fig. 6 and *SI Appendix*, Fig. S4 and *Appendix S1* (30–33)]. Additionally, the data strongly argue that the dipole moment exceeds that of all other field components (Fig. 6 and *SI Appendix*, Fig. S4), since a dominantly nondipolar field would fail to reproduce both the high degree of antipodality and low among-flow PSV dispersion of our observed paleofield directions. The lack of observed excursion directions among the 20 sites from poles HEBh and KUH-R also sets a 2σ confidence upper bound of $1\text{-}(0.05)^{1/20}$ ~14% on the fraction of time the paleofield spent in a transitional state, similar to geologically recent periods of relatively unstable yet still strongly dipolar fields (34).

This reversal, predating the oldest high-fidelity example by 480 My [*SI Appendix*, *Appendix S2.1* (35)], constitutes the oldest direct test of the GAD field geometry. The 3.25-Ga geodynamo was dominantly a reversible yet directionally stable dipole, the hallmark of stable self-alignment to Earth's rotation axis. This stands in contrast to thin-shell geodynamo mechanisms [e.g., a basal silicate magma ocean (9)] with high aspect ratios that would generate strongly nondipolar and unstable surface fields that do not undergo antipodal reversals, similar to those of the ice-giant planets (36). This scenario involving a nondipolar dynamo would require the following unlikely sequence of events to explain the reversal in our samples: the local paleofield happened to persist over many PSV timescales in one direction and then coincidentally changed to the antipodal direction and persisted there.

In contrast, a stable dipole is in agreement with models of the Archean geodynamo that generate a field throughout the volume of the core (8), as well as with previous observations suggesting a stably dipolar Archean field (30, 37, 38), reaffirming the basic principles of paleomagnetism-based paleogeography up to 3.25 Ga. Additionally, the solar wind standoff distance is several times greater for dipolar fields than for multipolar fields of similar strength (39), so dipole-dominant fields can suppress [or enhance (40)] atmospheric modification via nonthermal escape and better shield the surface from cosmic radiation. This suggests a stably dipolar geodynamo may have contributed to a stable and habitable surface environment for the nascent biosphere since at least 3.25 Ga.

Materials and Methods

More-detailed materials and methods are presented in the supplement in *SI Appendix*, *Appendix S1*). We extracted 117 oriented 2.5-cm cores of Kunagunarrina Formation lavas from 11 total sites (cooling units; 7–12 cores each) representing three localities (KUA, KUB, and KUT) in the southern SVS (Fig. 1 and *SI Appendix*, Fig. S1). We drilled and field oriented all core samples using magnetic and solar compasses. We performed stepwise thermal demagnetization on all core samples, measuring their magnetic moments using a 2G Enterprises DC-SQuID Superconducting Rock Magnetometer at the Harvard Paleomagnetics Laboratory. We subjected all samples to alternating field (AF) demagnetization up to 10 mT in steps of 1 mT followed by thermal demagnetization up to 590 °C in steps of 10–40 °C (e.g., Fig. 2 *A*–*C*). We also performed a hybrid thermal demagnetization up to 430–540 °C followed by AF demagnetization to 110 mT (*SI Appendix*, Fig. S3) on selected samples and merged this dataset with our thermal demagnetization data (*SI Appendix*, *Appendix S1.3*).

We quantified the directions of all magnetization components using principal-component analysis (41). To compute directions in tilt-corrected (bedding) coordinates, we first rotated directions and bedding attitudes from KUA 40° clockwise and KUB 52° clockwise about the vertical axis to correct for drag folding of the SVS hinge plane (*SI Appendix*, Fig. S5 *C* and *D*). We then rotated all directions and bedding attitudes to correct for the plunging axis of the SVS (plunging 41° toward 69° E of N) and then corrected all directions to restore local paleohorizontal based on lava flow bedding attitudes (Fig. 2*E* and *SI Appendix*, Fig. S5 *B* and *C*). Over the last tilt-correction step, we performed the paleomagnetic fold test of Tauxe and Watson (13) (*SI Appendix*, Fig. S2*B*). On fully tilt-corrected directions, we performed the reversal test of McFadden and McElhinny (14). When comparing with other paleopoles, we performed additional rotations about a vertical axis on data from the SVS (pole HEBh and pole KUH-R from the present study) to correct for ~2.93 Ga 0–70° clockwise rotation of the SVS structural block (*SI Appendix*, Fig. S5 *A* and *B*; see *SI Appendix*, Appendix S2; ref. 22).

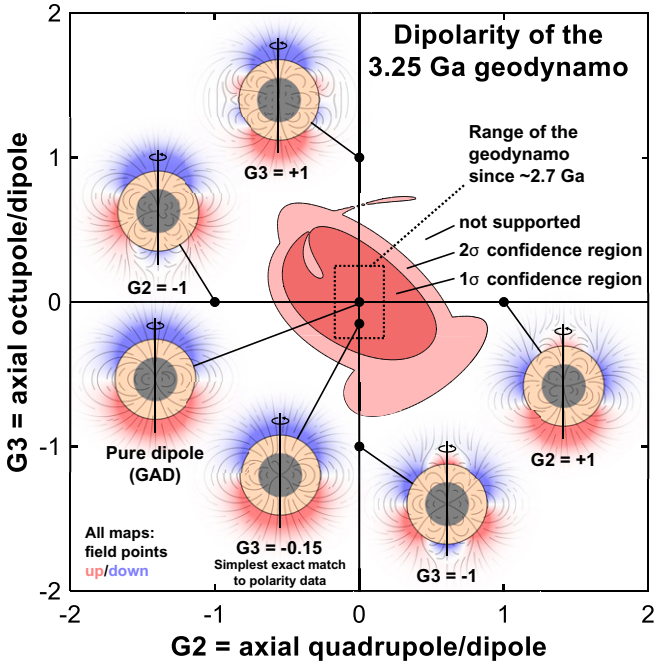

Fig. 6. Constraints on geomagnetic field dipolarity at 3.25 Ga. The directional stability and polarity inclinations of the KUH-R pole constrain the axial quadrupole/dipole (*G2*, x axis) and octupole/dipole (*G3*, y axis) moments ratios to the 1σ and 2σ confidence regions in red. *Insets* show representative field geometries. The data are consistent with a pure geocentric axial dipole field ("GAD" inset, at 0,0 on this plot). While reproducing the observed polarity inclinations exactly without including uncertainty would only require a 15% relative contribution from an axial octupole ("*G3* = −0.15" inset), we cannot rule out the simpler explanation of a GAD field, since it remains statistically compatible with our polarity data based on this test and a traditional common-mean reversal test (14). The 3.25-Ga field was therefore strongly dipolar and consistent with previous constraints on Precambrian field geometry [dashed rectangle (30–33)].

To identify the remanence-carrying magnetic grains, we observed oriented polished sections of several cores with the QDM (42) at the Harvard Paleomagnetics Laboratory, as in Brenner et al. (4) (*SI Appendix*, Figs. S7–S12). For one sample (KUB2), we also conducted an abbreviated demagnetization routine (NRM, 10 mT AF, and thermal cycles to 330 °C, 490 °C, 520 °C, and 560 °C) and imaged the sample throughout with the QDM. Following the methods of Volk et al. (43), changes in surface field patterns during demagnetization captured the unblocking of the phases hosting the imaged magnetizations (*SI Appendix*, Fig. S10).

We used a Horiba Scientific XploRA Plus Raman microscope in the Harvard Laboratory for Mineral Physics to identify mineral phases. Raman spectra from reduced carbonaceous matter (*SI Appendix*, Fig. S7 *K* and *L*) allowed for estimates of peak alteration temperature, following the methods of Kouketsu et al. (44). We also imaged selected samples with a JEOL JSM-7900F Schottky field emission scanning electron microscope.

We used the laser-ablation split-stream inductively coupled plasma mass spectrometry facility at the University of California, Santa Barbara to collect U-Pb petrochronology and trace-element abundance data from 120 titanites in situ on

selected polished sections from samples KUB1 and KUB2 (*SI Appendix*, Fig. S11; see below *SI Appendix, Appendix S4.5*). The spot size of all analyses was 30 μm. All uncertainties reported herein are 2σ, and all reported ages are lower intercept ages anchored to the common Pb composition of $^{207}Pb/^{206}Pb = 1.13$ expected for ∼3.2-Ga rocks (45). We filtered the analyses based on several criteria (*SI Appendix, Appendix S1.7*) to a compilation of 93 spots. To isolate analyses unaffected by minor postcrystallization Pb loss, we performed Gaussian deconvolution of their age distribution (46).

Data, Materials, and Software Availability. [Demagnetization Datafiles] data have been deposited in [MagIC Database] (DOI: 10.7288/V4/MAGIC/19546) (47).

ACKNOWLEDGMENTS. We thank Arthur Hickman and Martin Van Kranendonk for their insights on the rock units, preservation potential, and structural elements of the East Pilbara and Soanesville Syncline. We thank Rebecca Fischer for the use of the Raman microscope in the Harvard Laboratory for Mineral Physics. We thank Timothy Cavanaugh for imaging our samples with the SEM at the Harvard Center for Nanoscale Systems. We thank Franklin Wolfe and John Shaw for advice on the treatment of structural corrections. We thank Hairuo Fu for assistance with sampling. Finally, we acknowledge the Nyamal and Kariyarra peoples, Traditional Custodians of the land on which we conducted this study and of Kunanganaranga Pool on the Turner River, from which the Kunagunarrina Formation derives its name. This work was supported by grants from the NSF (EAR-1847042 and EAR-1723023).

1. A. Lenardic, The diversity of tectonic modes and thoughts about transitions between them. *Philos. Trans.- Royal Soc., Math. Phys. Eng. Sci.* **376**, 20170416 (2018).
2. K. J. Matthews *et al.*, Global plate boundary evolution and kinematics since the late Paleozoic. *Global Planet. Change* **146**, 226–250 (2016).
3. L. M. Wallace, R. McCaffrey, J. Beavan, S. Ellis, Rapid microplate rotations and backarc rifting at the transition between collision and subduction. *Geology* **33**, 857–860 (2005).
4. A. R. Brenner *et al.*, Paleomagnetic evidence for modern-like plate motion velocities at 3.2 Ga. *Sci. Adv.* **6**, eaaz8670 (2020).
5. M. McElhinny, W. Senanayake, Paleomagnetic evidence for the existence of the geomagnetic field 3.5 Ga ago. *J. Geophys. Res. Solid Earth* **85**, 3523–3528 (1980).
6. K. Bradley, B. P. Weiss, R. Buick, Records of geomagnetism, climate, and tectonics across a Paleoarchean erosion surface. *Earth Planet. Sci. Lett.* **419**, 1–13 (2015).
7. A. J. Biggin *et al.*, Palaeomagnetism of Archaean rocks of the Onverwacht Group, Barberton Greenstone Belt (southern Africa): Evidence for a stable and potentially reversing geomagnetic field at ca. 3.5 Ga. *Earth Planet. Sci. Lett.* **302**, 314–328 (2011).
8. T. Mittal *et al.*, Precipitation of multiple light elements to power Earth's early dynamo. *Earth Planet. Sci. Lett.* **532**, 116030 (2020).
9. L. Stixrude, R. Scipioni, M. P. Desjarlais, A silicate dynamo in the early Earth. *Nat. Commun.* **11**, 935 (2020).
10. L. Z. Evins, F. Jourdan, D. Phillips, The Cambrian Kalkarindji Large Igneous Province: Extent and characteristics based on new 40Ar/39Ar and geochemical data. *Lithos* **110**, 294–304 (2009).
11. Z. Li, W. Guo, C. Powell, "Timing and genesis of Hamersley BIF-hosted iron deposits: A new palaeomagnetic interpretation" (Rep. 199, Minerals and Energy Research Institute of Western Australia, 2000).
12. D. Evans, A. V. Smirnov, A. Gumsley, Paleomagnetism and U–Pb geochronology of the Black Range dykes, Pilbara Craton, Western Australia: A Neoarchean crossing of the polar circle. *Aust. J. Earth Sci.* **64**, 225–237 (2017).
13. L. Tauxe, G. Watson, The fold test: An eigen analysis approach. *Earth Planet. Sci. Lett.* **122**, 331–341 (1994).
14. P. McFadden, M. McElhinny, Classification of the reversal test in palaeomagnetism. *Geophys. J. Int.* **103**, 725–729 (1990).
15. A. H. Hickman, *East Pilbara Craton: A Record of One Billion Years in the Growth of Archean Continental Crust* (Geological Survey of Western Australia, 2021).
16. D. L. Huston *et al.*, The timing of mineralization in the Archean North Pilbara terrain, Western Australia. *Econ. Geol.* **97**, 733–755 (2002).
17. S. Vearncombe *et al.*, 3.26 Ga black smoker-type mineralization in the Strelley belt, Pilbara craton, Western Australia. *J. Geol. Soc. London* **152**, 587–590 (1995).
18. H. Gibson, R. Morton, G. Hudak, Submarine volcanic processes, deposits, and environments favorable for the location of volcanic-associated massive sulfide deposits. *Rev. Econ. Geol.* **8**, 13–51 (1999).
19. J. W. Jamieson *et al.*, Sulfide geochronology along the Endeavour Segment of the Juan de Fuca Ridge. *Geochem. Geophys. Geosyst.* **14**, 2084–2099 (2013).
20. C. Lalou, J. L. Reyss, E. Brichet, P. A. Rona, G. Thompson, Hydrothermal activity on a 105-year scale at a slow-spreading ridge, TAG hydrothermal field, Mid-Atlantic Ridge 26° N. *J. Geophys. Res. Solid Earth* **100** (B9), 17855–17862 (1995).
21. R. Buick *et al.*, Geochronology and stratigraphic relationships of the Sulphur Springs Group and Strelley Granite: A temporally distinct igneous province in the Archaean Pilbara Craton, Australia. *Precambrian Res.* **114**, 87–120 (2002).
22. M. J. Van Kranendonk, *Structural Geology of the Central Part of the Lalla Rookh Western Shaw Structural Corridor* (Geological Survey of Western Australia, Pilbara Craton, Western Australia, 2008).
23. M. L. Rudolph, S. J. Zhong, History and dynamics of net rotation of the mantle and lithosphere. *Geochem. Geophys. Geosyst.* **15**, 3645–3657 (2014).
24. J. L. Kirschvink, R. L. Ripperdan, D. A. Evans, Evidence for a large-scale reorganization of Early Cambrian continental masses by inertial interchange true polar wander. *Science* **277**, 541–545 (1997).
25. T. H. Torsvik *et al.*, Phanerozoic polar wander, palaeogeography and dynamics. *Earth Sci. Rev.* **114**, 325–368 (2012).
26. D. Pastor-Galán, E. L. Pueyo, M. Diederen, C. García-Lasanta, C. G. Langereis, Late Paleozoic Iberian orocline (s) and the missing shortening in the core of Pangea. Paleomagnetism from the Iberian Range. *Tectonics* **37**, 3877–3892 (2018).
27. R. W. Allmendinger, R. Smalley, Jr, M. Bevis, H. Caprio, B. Brooks, Bending the Bolivian orocline in real time. *Geology* **33**, 905–908 (2005).
28. M. J. Van Kranendonk, R. Hugh Smithies, A. H. Hickman, M. T. D. Wingate, S. Bodorkos, Evidence for Mesoarchean (∼3.2Ga) rifting of the Pilbara Craton: The missing link in an early Precambrian Wilson cycle. *Precambrian Res.* **177**, 145–161 (2010).
29. T. Kusky *et al.*, Archean dome-and-basin style structures form during growth and death of intraoceanic and continental margin arcs in accretionary orogens. *Earth Sci. Rev.* **220**, 103725 (2021).
30. A. J. Biggin *et al.*, Quantitative estimates of average geomagnetic axial dipole dominance in deep geological time. *Nat. Commun.* **11**, 6100 (2020).
31. T. Veikkolainen, L. Pesonen, K. Korhonen, An analysis of geomagnetic field reversals supports the validity of the Geocentric Axial Dipole (GAD) hypothesis in the Precambrian. *Precambrian Res.* **244**, 33–41 (2014).
32. D. V. Kent, M. A. Smethurst, Shallow bias of paleomagnetic inclinations in the Paleozoic and Precambrian. *Earth Planet. Sci. Lett.* **160**, 391–402 (1998).
33. D. A. Evans, Proterozoic low orbital obliquity and axial-dipolar geomagnetic field from evaporite palaeolatitudes. *Nature* **444**, 51–55 (2006).
34. M. Tominaga, W. W. Sager, M. A. Tivey, S. M. Lee, Deep-tow magnetic anomaly study of the Pacific Jurassic Quiet Zone and implications for the geomagnetic polarity reversal timescale and geomagnetic field behavior. *J. Geophys. Res. Solid Earth* **113**, (2008).
35. G. Strik, T. S. Blake, T. E. Zegers, S. H. White, C. G. Langereis, Palaeomagnetism of flood basalts in the Pilbara Craton, Western Australia: Late Archaean continental drift and the oldest known reversal of the geomagnetic field. *J. Geophys. Res. Solid Earth* **108**, (2003).
36. S. Stanley, J. Bloxham, Numerical dynamo models of Uranus' and Neptune's magnetic fields. *Icarus* **184**, 556–572 (2006).
37. T. Veikkolainen, L. J. Pesonen, Palaeosecular variation, field reversals and the stability of the geodynamo in the Precambrian. *Geophys. J. Int.* **199**, 1515–1526 (2014).
38. A. V. Smirnov, J. A. Tarduno, D. A. Evans, Evolving core conditions ca. 2 billion years ago detected by paleosecular variation. *Phys. Earth Planet. Inter.* **187**, 225–231 (2011).
39. O. O. Tsareva, E. M. Dubinin, H. V. Malova, V. Y. Popov, L. M. Zelenyi, Atmospheric escape from the Earth during geomagnetic reversal. *Ann. Geophys.* **63**, 223 (2020).
40. H. Gunell *et al.*, Why an intrinsic magnetic field does not protect a planet against atmospheric escape. *Astron. Astrophys.* **614**, L3 (2018).
41. J. Kirschvink, The least-squares line and plane and the analysis of palaeomagnetic data. *Geophys. J. R. Astron. Soc.* **62**, 699–718 (1980).
42. D. R. Glenn *et al.*, Micrometer-scale magnetic imaging of geological samples using a quantum diamond microscope. *Geochem. Geophys. Geosyst.* **18**, 3254–3267 (2017).
43. M. W. R. Volk, R. R. Fu, A. Mittelholz, J. M. D. Day, Paleointensity and rock magnetism of Martian Nakhlite meteorite miller range 03346: Evidence for intense small-scale crustal magnetization on Mars. *J. Geophys. Res.* **126**, e2021JE006856 (2021).
44. Y. Kouketsu *et al.*, A new approach to develop the R aman carbonaceous material geothermometer for low-grade metamorphism using peak width. *Isl. Arc* **23**, 33–50 (2014).
45. Jt. Stacey, J. Kramers, Approximation of terrestrial lead isotope evolution by a two-stage model. *Earth Planet. Sci. Lett.* **26**, 207–221 (1975).
46. M. Sambridge, W. Compston, Mixture modeling of multi-component data sets with application to ion-probe zircon ages. *Earth Planet. Sci. Lett.* **128**, 373–390 (1994).
47. A. R. Brenner, R. R. Fu, A. R. C. Kylander-Clark, G. J. Hudak, B. J. Foley, Kunagunarrina Formation demagnetization data. MagIC Database. https://www2.earthref.org/MagIC/19546. Deposited 14 June 2022.
48. M. T. D. Wingate, C. L. Kirkland, S. Bodorkos, A. H. Hickman, 160258: Felsic metavolcanic rock, Orchard Well (Geochronology Record 840, Geological Survey of Western Australia, 2010).
49. T. Zegers, D. Nelson, J. Wijbrans, S. White, SHRIMP U-Pb zircon dating of Archean core complex formation and pancratonic strike-slip deformation in the East Pilbara Granite-Greenstone Terrain. *Tectonics* **20**, 883–908 (2001).
50. M. Seton *et al.*, Global continental and ocean basin reconstructions since 200 Ma. *Earth Sci. Rev.* **113**, 212–270 (2012).

PNAS
www.pnas.org

Supplementary Information for
Plate motion and a dipolar geomagnetic field at 3.25 Ga

Alec R. Brenner[1]*, Roger R. Fu[1], Andrew R.C. Kylander-Clark[2], George J. Hudak[3], Bradford J. Foley[4].
[1]Department of Earth and Planetary Sciences, Harvard University, Cambridge, MA, USA.
[2]Department of Earth Science, University of California, Santa Barbara, CA, USA.
[3]Natural Resources Research Institute, University of Minnesota Duluth, Duluth, MN, USA.
[4]Department of Geosciences, Pennsylvania State University, State College, PA, USA.

***Correspondence to Alec Brenner**
Email: alecbrenner@g.harvard.edu

This PDF file includes:

Supplementary Information Text (Appendices S1-S5)
Figures S1 to S13 (throughout text)
Tables S1 to S2
Legend for Dataset S1
SI References

Other supplementary materials for this manuscript include the following:

Dataset S1

Supplementary Information Text

Table of Contents

Supplementary figures are placed in relevant sections throughout the text for ease of reading.

Appendix S1: Extended Materials and Methods

S1.1. Sampling. We extracted 117 oriented 2.5 cm diameter cores of Kunagunarrina Formation lavas from 11 total sites (= cooling units; seven to 12 cores each) representing three localities (KUA, KUB, KUT) in the southern Soanesville Syncline (SVS; Main Text Fig. 1, Fig. S1). The distinct local bedding attitudes at localities KUA (strike/dip = 250.0°/56.6°) and KUB (300.1°/51.5°), which are corrected for local magnetic declination from true North (-1.0° at KUA and -1.7° at KUB), permit a fold test within the SVS. Locality KUT, adjacent to KUA, is within the lapillistone marker bed in the stratigraphic middle of the formation. At KUT, we sampled from tephra clasts and lava bombs, permitting a conglomerate test. We drilled and field-oriented all core samples using magnetic and solar compasses while avoiding topographically-prominent outcrops susceptible to lightning strikes where possible. Within each locality, we used a single paleohorizontal (bedding) attitude across all sites, thus averaging local bedding attitude variability measured from rubbly flowtops, the strike of bedding-parallel ridges, and somewhat undulatory chert and sediment interbeds.

S1.2. Measurement of magnetization components. We performed stepwise thermal demagnetization on all core samples, measuring their magnetic moments using a 2G Enterprises DC-SQuID Superconducting Rock Magnetometer at the Harvard Paleomagnetics Laboratory. To remove magnetizations carried by multi-domain grains, we subjected all samples to alternating field (AF) demagnetization up to 10 mT in steps of 1 mT followed by thermal demagnetization up to 590°C in steps of 10 to 40°C (e.g., Main Text Fig. 2, A-C). We quantified the directions of magnetization components using principal-component analysis (1), and did not force the highest-temperature component(s) of magnetization to include the origin (2). Use of origin-forced fits to all samples did not significantly change our results. We identified six components of magnetization common to at least 10 samples (Table S1). One component ("AF") is unblocked by AF demagnetization up to 10 mT in all samples. Directions recovered from this component are random in both *in situ* and tilt-corrected coordinates. Upon thermal demagnetization, a low-temperature component (L) unblocks between 75 and ~300°C in 65 samples. Its direction in *in situ* coordinates (D, I = 359.0°, -45.8°; α_{95} = 3.7°) (Fig. S2A) is consistent with the present-day geomagnetic field direction (I = -38.2° assuming a current geocentric axial dipolar (GAD) geometry), so we interpret the L component as a recent viscous remanent magnetization (VRM).

Fifteen samples show a different low temperature component (L2) with a shallow northeast direction (D, I = 63.1°, -8.9°; α_{95} = 10.6°) (Fig. S2A). This component is weak, typically unblocking between 75 and ~200°C, is directionally coherent in *in situ* coordinates, and was most likely acquired around 0.54 Ga based on comparison with the Australian apparent polar wander (APW) path (3). This may correlate with early stages of heating with the ~0.51 Ga Kalkarindji large igneous province (3, 4). A medium-temperature component (M) appears in 45 samples, typically unblocking between ~200 and 500°C, and displays a scattered but shallow northwest-upward mean direction in *in situ* coordinates (D, I = 307.8°, -25.0°; α_{95} = 5.9°) (Fig. S2A). In ~35 samples, a significant fraction of total remanence unblocks between the 315 and 355°C heating steps, suggesting that the M component is at least partially carried by pyrrhotite ($T_{Néel}$ ~ 325°C). We correlate the M component with magnetizations of similar unblocking temperature and direction (D, I ~ 310°, -20°) that are widely observed as a regional overprint throughout the Pilbara Craton (5-7). These magnetizations are thought to reflect partial thermoremanent magnetization (pTRM) during low-grade regional metamorphism associated with Paleoproterozoic tectonism on the southern margin of the Pilbara Craton, either during the 2.215-2.145 Ga Ophthalmian Orogeny (8, 9) or 1.83-1.78 Ga Capricorn Orogeny. In 11 samples from localities KUA and KUT, another component (M2) unblocks between 435-520°C. The *in situ* direction of this component is NW-down (D, I = 318.0°, 38.4°; α_{95} = 13.7°) (Fig. S2A) and is distinct from both the M component and all directions unblocking at higher temperatures. Since M2 is overprinted by M, the timing of M2 magnetization is constrained to ≥1.7-2.2 Ga and <3.25 Ga. The only similar documented direction from the East Pilbara within this interval is from the earliest lavas of the Fortescue Group [pole "P0"; D, I = 305°, 72°; (10-12)], making a ~2.78 Ga pTRM origin for M2 likely. Still, this does not rule out a pTRM origin during other metamorphic events within the available timeframe, most notably those responsible for the folding of the SVS.

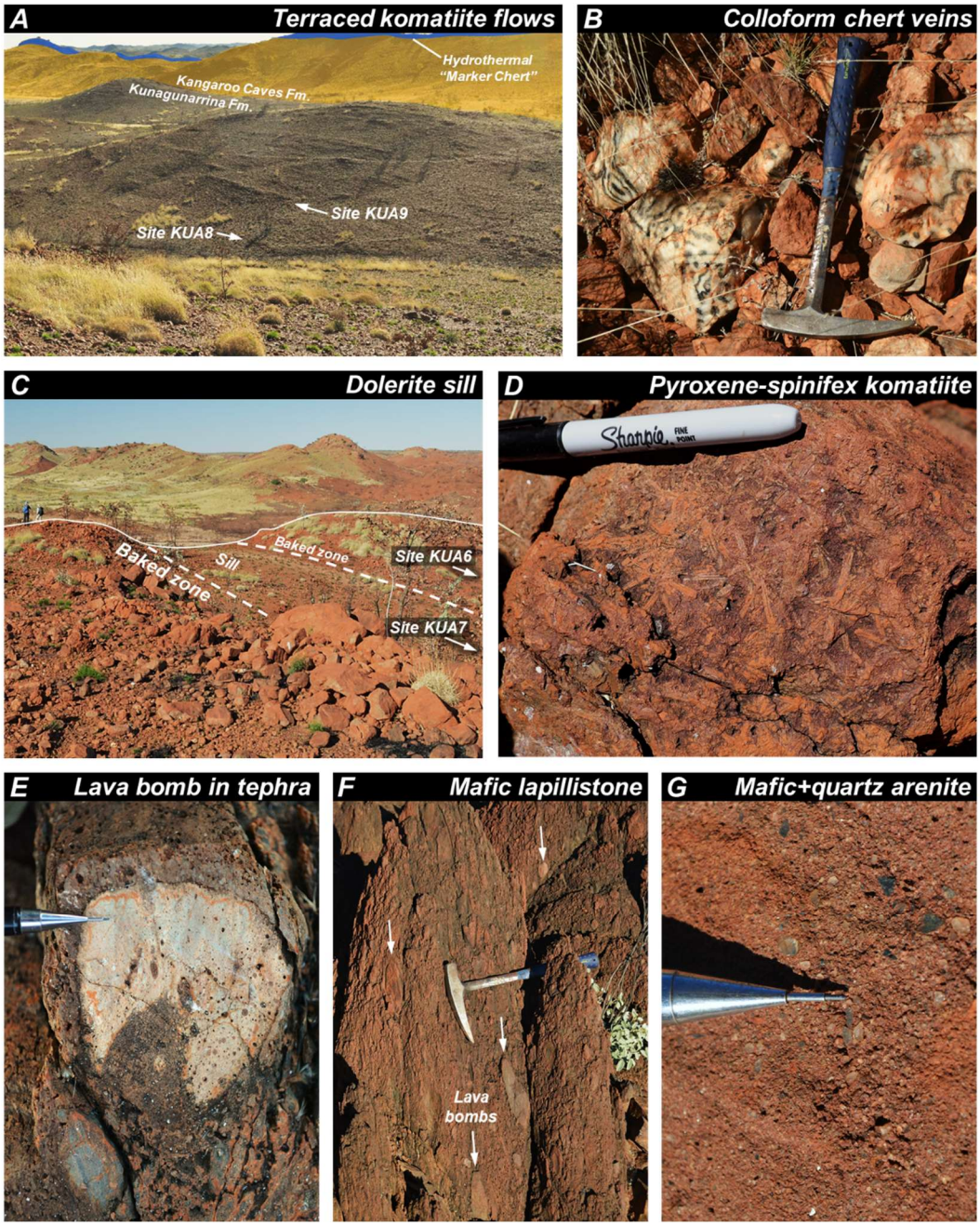

Figure S1. Field photographs of the sampled rocks and their associated lithofacies. A. Komatiite flows of the Kunagunarrina Formation form low terraces on a hillslope denuded by a recent wildfire. This view also includes the overlying Kangaroo Caves Formation (yellow shading) and its capping regional exhalite chert horizon (blue). Local bedding dips 57° to the right (photograph faces west). **B.** Vein of colloform hydrothermal black-and-white chert immediately underlying the exhalite "Marker Chert" horizon in Panel A. Hammer is 41 cm long. **C.** Hilltop exposure near sites KUA6 and KUA7 of the sampled dolerite sill. The dolerite is recessive relative to its baked zones, and thus occupies a depression with little to no exposure. **D.** Pyroxene-spinifex texture visible in komatiite flow KUA2. **E.** Lava bomb with intact uncompressed vesicles preserved amongst strongly-altered tephra in the lapillistone horizon at locality KUT. 0.5 mm pencil gives scale. **F.** The lapillistone horizon, including several lava bombs. **G.** Arenite with grains of mafic minerals and quartz sand just below the lapillistone horizon.

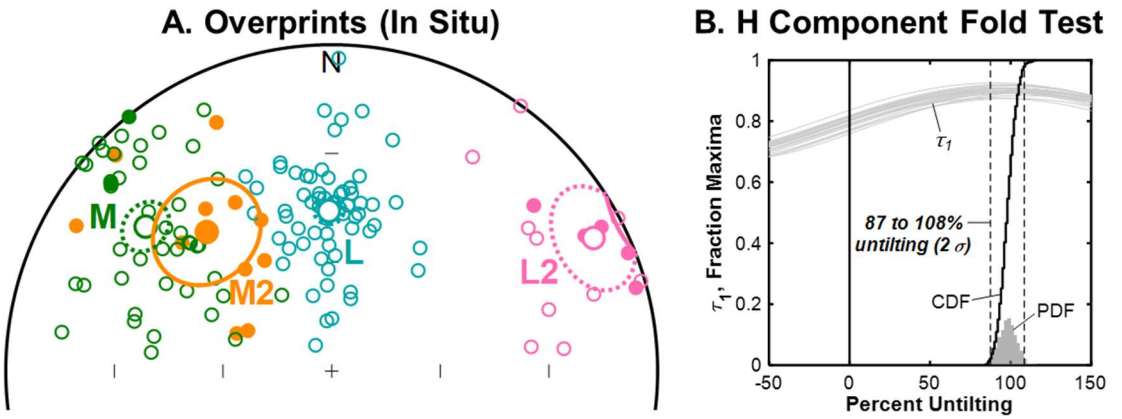

Figure S2. Additional paleomagnetic results. A. Stereonet of overprinting components in *in situ* coordinates, with the same colors as in Main Text Fig. 2A-C (see also Table S1). The AF component is not shown, since it is scattered randomly regardless of coordinate system. **B.** Results of a paleomagnetic fold test (13) on H components from all sites, shown as the likelihood (gray histogram) and cumulative (black curve) distributions of percent unfolding, with principal eigenvalues τ_1 shown as light gray curves. Since 100% unfolding is within the 2σ confidence interval of the test, a prefolding H magnetization is supported.

The highest-temperature component of magnetization ("H") unblocks between ~400 and 590°C in 44 samples from 10 out of 11 sites (Main Text Fig. 2; Table S1). This component is a magnetite-hosted thermochemical remanent magnetization (TCRM) based on its maximum unblocking temperature, origin-trending direction, and the mineralogical context of its carrier phases (see below Appendix S4, "*Magnetization timing from alteration mineralogy*"). The H component unblocks up to ~550-590°C (Main Text Fig. 2, A-C), whereas the Kunagunarrina Formation in the SVS is metamorphosed up to lower greenschist facies (330°C), thereby ruling out a full thermal overprint origin after 3.25 Ga. The demagnetization behavior of the H component varies substantially by site and by lithology. For instance, sites KUA3-4 and KUB1-2 are vesicular komatiitic basalt flows with sub-mm- to cm-scale pyroxene-spinifex texture. In these sites the H component is strongly site-coherent (k > 50), can represent up to ~90% of the moment unblocked during thermal demagnetization, and primarily unblocks in a narrow temperature range from 490 to 530°C (Main Text Fig. 2, B-C). In other sites, which included komatiitic to tholeiitic basalts and a contemporaneous dolerite sill (site KUA7; Fig. S1C; see below Appendix S3), the H component makes up a smaller fraction of the total sample moments (Main Text Fig. 2A).

Hydrothermal alteration was particularly pronounced in locality KUT, our conglomerate test, in which few samples displayed interpretable magnetization components above ~300°C. The lapillistone horizon has been strongly sheared and fully recrystallized to a fine carbonate matrix with chlorite and sub-mm euhedral anatase grains, and also hosts massive hydrothermal quartz (Main Text Fig. 1C). This strong carbonate alteration likely occurred during seafloor hydrothermalism (see below Appendix S4, "*Magnetization timing from alteration mineralogy*") and is pronounced in the lapillistone horizon due to its high fluid permeability relative to the surrounding mechanically-competent and unsheared lithologies. Strong recrystallization likely led to the consumption of all but the largest multi-domain grains by bulk hydrothermal leaching of Fe, as evidenced by the weak magnetizations of KUT samples. The resulting viscous behavior of H component carriers would explain the tendency of the few interpretable components in KUT towards northerly and up directions, along the present-day field direction. The instability of directions measured from KUT samples, coupled with little to no remanence in the H component unblocking range, make the conglomerate test indeterminate.

We also performed a hybrid thermal demagnetization up to 430-540˚C followed by AF demagnetization to 110 mT (Fig. S3) on samples with partial lightning IRM overprints and evidence for oven remanence acquisition and merged this dataset with our traditional thermal

demagnetization data (see Appendix S1.3, "*Hybrid thermal and AF demagnetization on selected samples*" below). This hybrid method is similar in intent and execution to that of Biggin et al. (14). From the resulting H component data, we excluded samples with maximum angular deviations (MAD) >20°. We also excluded obvious outlier directions, defined here as H component directions that differed from well-clustered H components from other samples within the same site by more than ~30°, often because H component fits in such samples were based on too few points to reliably average noise in the demagnetization path. The few outlier directions that we identified were nearly all also excluded by the MAD>20° filter, meaning that explicitly excluding them has little effect on the resulting site-mean directions. Additionally, we excluded directions from samples with saturation overprints from lightning IRMs (Fig. S3D) and high-temperature demagnetization paths with no identifiable component, such as those from locality KUT and all from site KUA2 (Fig. S3E).

The resulting compilation of H component data contained 38 directions from as many samples in 10 of 11 sites. We calculated site mean directions from sample components (Main Text Fig. 2D) and retained only nine sites with at least two passing core samples each and within-site Fisher precision parameter $k \geq 20$. These site-means form three clusters of directions in *in situ* coordinates (Main Text Fig. 2D and Table S1). Sites KUA1, 3 and 4 – the lowermost sites in the KUA transect – form a cluster about a shallow southeast-downward direction (D, I = 151.7°, 10.1°; α_{95} = 25.8°). Sites KUA5-6 and 8-9, from the upper half of the transect, cluster about a shallow northwest-upward direction (D, I = 306.0°, -13.6°; α_{95} = 24.1°). Both sites in locality KUB define a third south-downward direction (D, I = 172.8°, 31.8°; α_{95} = 19.1°).

To compute the correct paleomagnetic directions in tilt-corrected (bedding) coordinates, we first rotated directions and bedding attitudes from KUA 40° clockwise, and KUB 52° clockwise, about the vertical axis to correct for drag-folding of the SVS hinge plane (Fig. S5, C and D). We then rotated all directions and bedding attitudes to correct for the plunging axis of the SVS [plunging 41° towards 69° E of N, as determined by Brenner*, et al.* (5) based on mapped bedding attitudes in the eastern SVS (15)], and then corrected all directions to restore local paleohorizontal based on lava flow bedding attitudes (Figs. 2E and S5, B and C). Over the last tilt-correction step, we performed the paleomagnetic fold test of Tauxe and Watson (13) (Fig. S2B). On fully tilt-corrected directions, we performed the reversal test of McFadden and McElhinny (16). When comparing with other paleopoles, we performed additional rotations about a vertical axis on data from the SVS (pole HEBh and pole KUH-R from the present study) to correct for ~2.93 Ga 0-70° clockwise rotation of the SVS structural block [Fig. S5, A and B; see Appendix S2, "*Geologic setting*"; (15)].

S1.3. Hybrid thermal and AF demagnetization on selected samples. The H component may be overprinted by isothermal remanent magnetizations (IRMs) from recent exposure to lightning strikes. Saturating lightning overprints are straightforward to identify thanks to their scattered yet strong moments that are origin-trending over the full range of unblocking temperatures (Fig. S3D). We excluded these samples from all further analyses. However, in some samples, the H component – while distinguishable from the lower-temperature demagnetization path – carried a thermochemical remanent magnetization (TCRM) partially mixed with a lightning overprint (Fig. S3A). We identified these samples based on two criteria: (a) at least half of their initial moment unblocked along a linear to smoothly arcuate demagnetization path upon AF treatment up to 10 mT, and (b) their H components fell close to great circle paths between their fitted ~8-10 mT AF demagnetization direction and the mean H component direction defined by other samples from the same site (Fig. S3C). For these samples we performed an additional "hybrid" demagnetization sequence as described below.

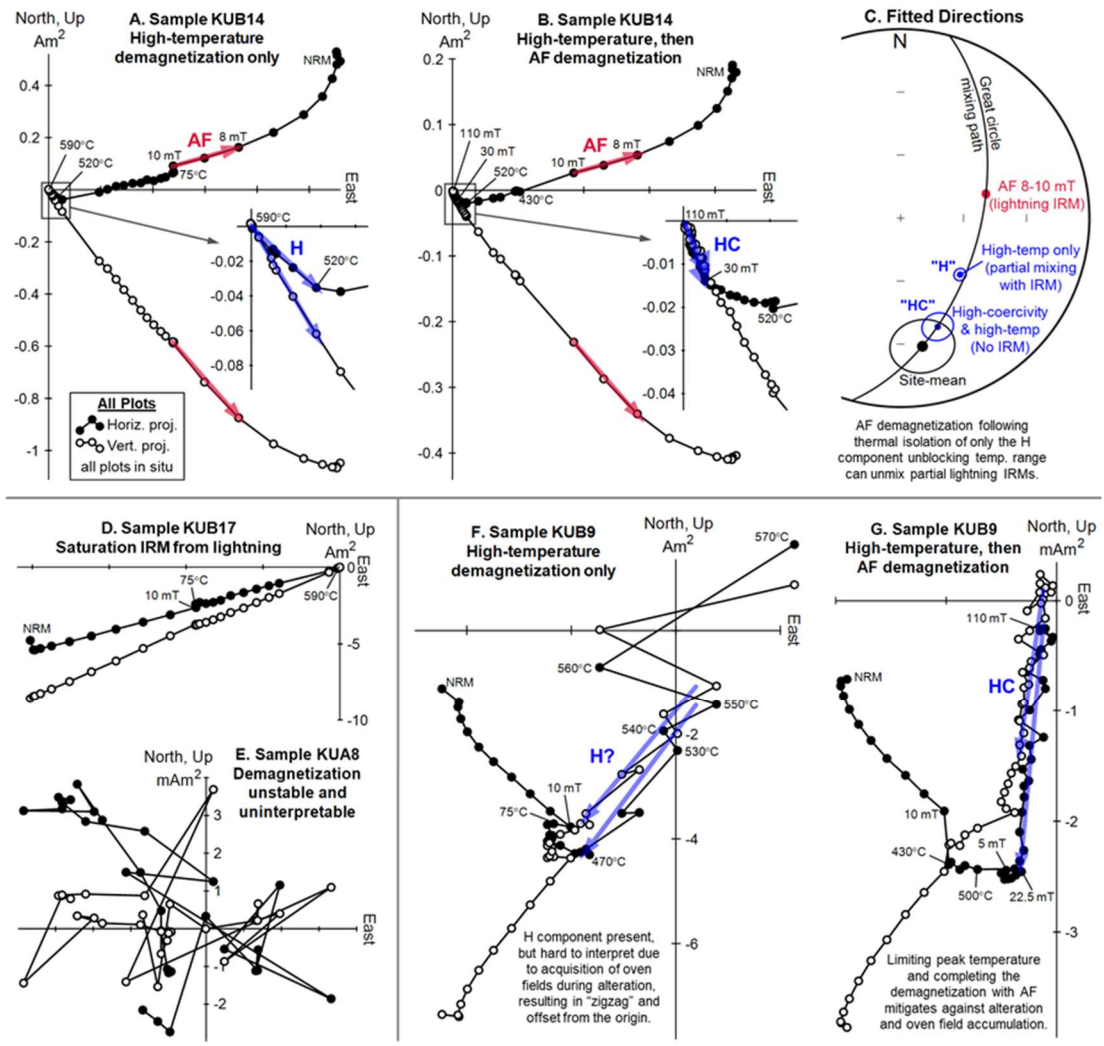

Figure S3. Examples of problematic vector demagnetizations and some solutions, shown as orthographic plots *in situ*. A. Thermal demagnetization of a sample with an H component (blue arrow and inset) distinguishable from the demagnetization path but mixed with a partial lightning isothermal remanence (IRM) unblocked by AF cleaning (red). **B.** Another subsample of the same core, but instead subjected to hybrid thermal-AF demagnetization (see Appendix S1, "*Extended Materials and Methods*"). The resulting high-temperature, high-coercivity component ("HC", blue arrow and inset) is unmixed from the lightning IRM (red). **C.** Stereonet of fitted directions from Panels A and B, showing mixing of the partial lightning IRM (red) with the true H component (black) direction along a connecting great circle path, and resulting H and HC components (blue). We rejected the H component direction and instead used the HC component. **D.** Thermal demagnetization of a sample fully-overprinted by lightning and unusable for paleomagnetic work. **E.** Thermal demagnetization of a sample without stable or interpretable magnetization components, and unusable for paleomagnetic work. **F.** Thermal demagnetization of a sample with a strong H component (blue) with gradual thermal alteration and residual field acquisition in the paleomagnetic oven. The sample accumulates an offset from the origin and exhibits a "zig-zag" demagnetization path due to alternating orientation within the oven (see Appendix S1, "*Extended Materials and Methods*"). Fitting an H component to this path is not straightforward. **G.** Another subsample of the same core, but instead subjected to hybrid thermal-AF demagnetization (see Appendix S1, "*Extended Materials and Methods*"). This approach heats the sample minimally, minimizing thermal alteration, and instead unblocks the high-temperature component with AF treatment, recovering a stable origin-trending HC direction (blue). We rejected the H component and instead used the HC component.

As discussed above (Appendix S1.2 above, "*Measurement of magnetization components*"), about 70 of our samples were prone to magnetic grain growth during sample heating, leading to unstable, non-origin-trending H component demagnetization paths and gradual remagnetization along residual (<20 nT) oven fields during demagnetization. This behavior was often accompanied by a "zig-zag" demagnetization path that resulted from alternating the sample orientation in the oven during adjacent thermal steps, done in part to mitigate for this remagnetization (Fig. S3F). For all such samples we averaged pairs of the highest-temperature demagnetization steps to suppress this zig-zag noise and to correct for the weak laboratory thermal remanence acquired in the oven, but this still resulted in demagnetization paths for about half of our samples that "missed" the origin by a measurable offset in moment not cancelled by pairwise step averaging (Fig. S3F). While this meant that affected samples had non-origin-trending H components, thus motivating our choice to use non-origin-forced fits, this effect was always subtle, with the moment offset never exceeding a few percent of the sample NRM moment. Anchoring all fits to the origin (2) did not alter our directional data or conclusions meaningfully, aside from slightly enhanced directional scatter attributed to random oven-related moment offsets.

Where possible, to address the issues of lightning IRM mixing, oven field acquisition during demagnetization, we adopted a similar method to that of Biggin et al. (14) and subjected oriented specimens from the same core to further demagnetization via a "hybrid" AF-thermal-AF demagnetization treatment. We included 54 samples that had distinguishable H components in thermal demagnetization, but that showed evidence for either (a) partial mixing with a lightning IRM as defined above or (b) alteration and subsequent acquisition of a residual oven pTRM. As with the standard thermal demagnetization procedure, this treatment began with AF cleaning up to 10 mT in 1 mT steps followed by thermal demagnetization starting at 430°C and ending at a temperature that we determined for each sample based on its previously-measured thermal demagnetization sequence. This endpoint temperature was chosen to be either (a) the temperature at which the sample's arcuate lightning IRM demagnetization path gave way to its linear origin-trending H component, or (b) the temperature at which alteration began steering the H component direction away from origin-trending behavior, typically starting with the attendant "zig-zag" behavior as defined above and with a rapid increase in the circular standard deviation of the measured direction. For samples with minimally-lightning-contaminated H components, the AF-following-thermal demagnetization may recover the uncontaminated H component by isolating magnetic carriers with coercivities higher than the peak field achieved in nearby past lightning strikes (Fig. S3C). For samples prone to magnetic grain growth during heating, the AF demagnetization routine may yield more interpretable H components by demagnetizing the H component without heating (Fig. S3G). The endpoint temperature ranged from 430-540°C, but was typically between 500 and 510°C. This limited thermal sequence is designed to eliminate magnetic carriers with unblocking temperatures too low to host the H component in all samples. After thermal demagnetization, we subjected all samples to AF treatment starting at 5 mT, progressing to 50 mT in steps of 2.5 mT, and then to 110 mT in steps of 5 mT.

In approximately 80% of treated samples, the hybrid thermal-AF demagnetization sequence (Fig. S3) successfully recovered site-coherent high-coercivity ("HC") components that reproduced or refined H component directions, indicating that directions measured herein are not sensitive to inclusion of partial lightning IRM overprints and oven pTRMs. The HC components unblocked between 5-110 mT, typically with most of the moment change between 20-80 mT.

For all samples from which we measured both an H and an HC component, we selected one of the two components to use in all further analyses. We used HC components only in samples where these were resolvable from their H component counterparts, indicating successful isolation of the HC component from partial IRMs or pTRMs, as well as in two samples with identifiable HC components but without clearly identifiable H components. In cases where both the H and HC components from a given sample were clearly recognizable and agreed in direction, we used the H component rather than the HC. In nine samples overprinted by lightning IRMs, we used the HC component if it was further than the H component from the 8-10 mT AF component direction, which is a proxy for the lightning overprint direction, and closer to the site-mean direction as defined by H components from other samples in the same site (i.e., the HC better unmixed the partial IRM from the true H direction; see Fig. S3, A-C). In three samples

prone to oven alteration, we used the HC component instead of the H component if the HC resulted in less offset in moment from the origin after full demagnetization relative to the moment unblocked by the H or HC component (i.e., the HC component better prevented the accumulation of a pTRM during oven heating; see Fig. S3, F and G).

Importantly, using only H component data without HC directions does not make a significant difference in our conclusions, resulting in 12 fewer sample directions and two fewer sites (KUA1 and KUA6). Further, site-means that included HC components differed from those using only H components by an average of 1.5° and always ≤5.5°, demonstrating that inclusion of HC components did not meaningfully bias the resulting directions. As a result, both H and HC component data exhibit the same degree of antipodality between the observed reversal polarities. Our "hybrid" AF-thermal-AF treatment therefore enhanced precision of site-level directions without altering conclusions.

S1.4. Paleopole data analysis. To measure PSV amplitude captured by our measured sites, we calculated the angular standard deviation S_B of its VGPs using the within-site dispersion correction after Doell (17):

$$S_B = \sqrt{S_{tot}^2 - \frac{S_w^2}{\bar{n}}} = \sqrt{\frac{1}{N-1}\sum_{i=1}^{N}\Delta_i^2 - \frac{1}{N}\frac{\left(\sum_{i=1}^{N}\frac{81°}{\sqrt{K_{wi}}}\right)^2}{\sum_{i=1}^{N} n_i}} \quad (1)$$

where N is the number of sites each with n_i samples (average is $\bar{n}$), S_{tot} is total dispersion, S_w is average within-site dispersion, Δ_i is the angular distance between the i^{th} VGP and the mean of all N VGPs, K_{wi} is the precision parameter of sample VGPs within the i^{th} site. We calculated K_{wi} from individual site direction precisions k_i and paleolatitudes λ_i after Cox (18):

$$K_{wi} = k_i\left[\frac{1}{8}(5 + 18\sin^2\lambda_i + 9\sin^4\lambda_i)\right]^{-1} \quad (2)$$

We adopted a common cutoff angle of $\Delta_i < 45°$ to exclude transitional directions (19, 20). Jackknife $(N-1)$ resampled S_{Bi} of the mean $\overline{S}_B$ estimate its uncertainty σ_{S_B} (21):

$$\sigma_{S_B} = \sqrt{\frac{N-1}{N}\sum_{i=1}^{N}\left(S_{Bi} - \overline{S}_B\right)^2} \quad (3)$$

For all reconstructions, we used Monte Carlo resampling (N=10^5) of the ages and positions of all paleopoles to estimate the uncertainty ranges of their latitudes, declinations, and the latitudinal/rotational motion rates between them. For KUH-R from this study, we assumed a normally-distributed age uncertainty with mean±2σ value 3250±15 Ma, and for poles EBm and HEBh, we assumed 3342.5±7.5 and 3184±8 Ma, respectively. We converted latitudinal motion rates from °/Myr to cm/yr with the factor 11.1 (cm/yr)/(°/Myr).

S1.5. Geomagnetic reversal analysis. To assess whether our observed reversal supports a resolvable departure from a dipolar geomagnetic field, we first compared the measured inclinations of its two polarities with those predicted by a reversing axial dipole and non-reversing axial quadrupole and octupole. In terms of paleolatitude λ, the axial quadrupole/dipole moment ratio $G2$, and the axial octupole/dipole moment ratio $G3$, the polarity inclinations are (22)

$$I_+ = \tan^{-1}\left(\frac{2\sin\lambda + 1.5G2(3\sin^2\lambda - 1) + 2G3(5\sin^3\lambda - 3\sin\lambda)}{\cos\lambda + G2(3\cos\lambda\sin\lambda) + 1.5G3(5\cos\lambda\sin^2\lambda - \cos\lambda)}\right) \quad (4)$$

$$I_- = \tan^{-1}\left(\frac{2\sin(-\lambda) + 1.5G2(3\sin^2\lambda - 1) + 2G3(5\sin^3\lambda - 3\sin\lambda)}{\cos(-\lambda) + G2(3\cos\lambda\sin\lambda) + 1.5G3(5\cos\lambda\sin^2\lambda - \cos\lambda)}\right) \quad (5)$$

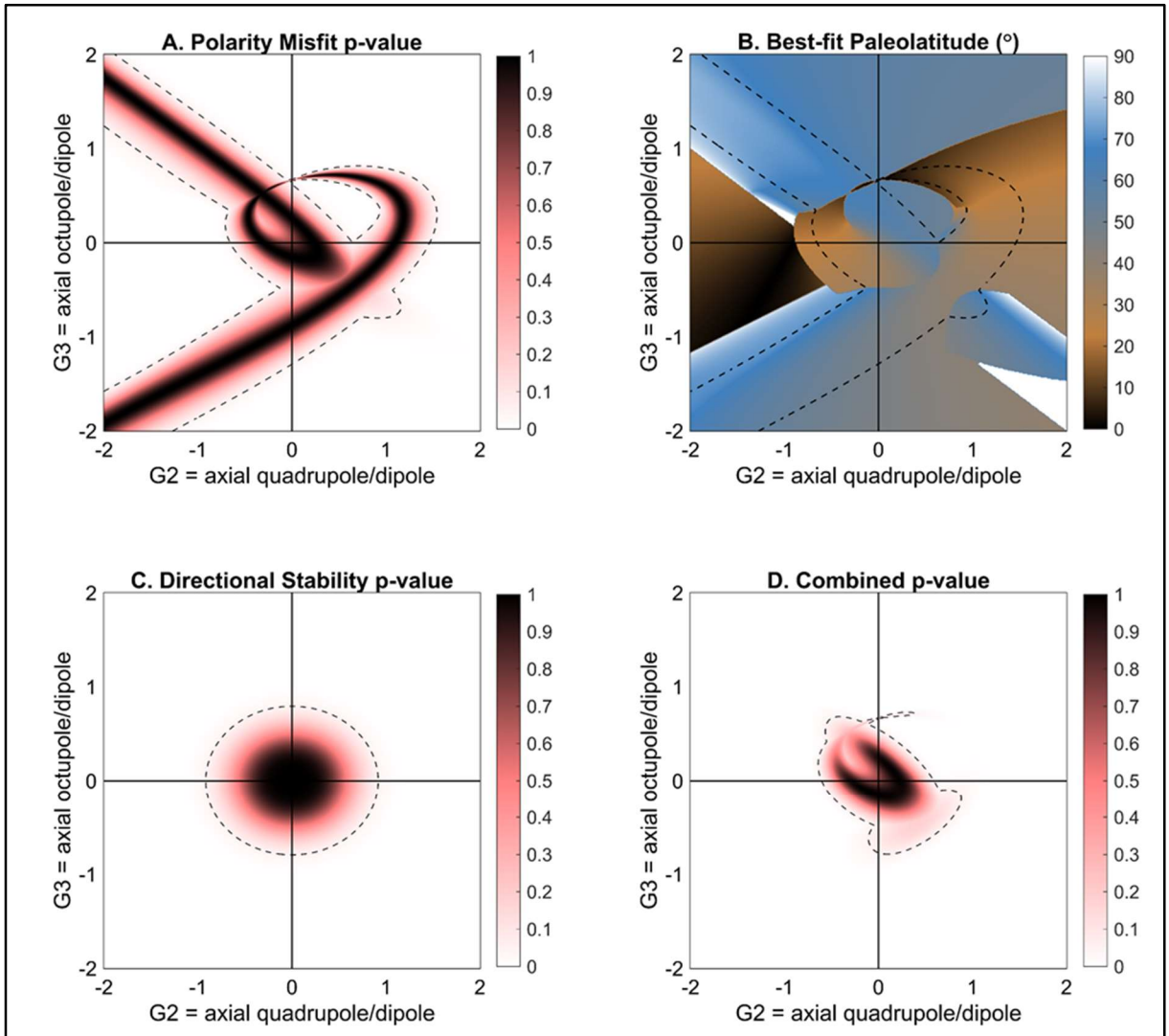

Figure S4. Breakdown of constraints on the dipolarity of the paleofield based on measured reversal geometry and directional stability. A. p-values of the combined minimized misfit of our two polarity inclinations to those of the paleofield with a reversing axial dipole, as a function of the additional relative contributions of the non-reversing axial quadrupole ($G2$) and octupole ($G3$). The lightest regions of this plot with p-values <0.05 (outside the dashed curve) are statistically incompatible with our measured polarities at 2σ confidence, while the center of the dark looped ribbon across the figure is a band of solutions that perfectly reproduce the observed polarities. The simplest non-GAD field geometry that perfectly reproduces our data is a reversing GAD field plus 15% non-reversing octupole ($G3 = -0.15$). **B.** Best-fitting paleolatitudes associated with the p-value mapping in Panel A. The sharp boundaries in some areas of this plot are results of crossovers in minimum misfit between multiple imperfect paleolatitude solutions. **C.** p-values associated with the measured directional stability (paleosecular variation) of the field, based on the relationship derived by Biggin et al. (23) who found that increasing dynamo dipolarity correlates with the minimum latitudinally-averaged field variability. This maps the probability that the field was at most as dipolar as each point in the plotted $G2 - G3$ space, again with the 2σ confidence region shown as a dashed ellipse. **D.** Combined probability map using both panels A and C, again with the 2σ confidence region shown as a dashed line. This map corresponds to Main Text Fig. 6.

The total misfit of our observed polarity inclinations $I_{OBS+} \pm \alpha_{95}$ to these values follows a χ^2 distribution with two degrees of freedom (one per polarity):

$$\sqrt{\left(\frac{I_{OBS} - I_+}{0.5\alpha_{95+}}\right)^2 + \left(\frac{I_{OBS-} - I_-}{0.5\alpha_{95-}}\right)^2} \sim \chi^2(df = 2) \quad (6)$$

For values of $G2$ and $G3$ from -2 to +2, well beyond the range of steady-state values thus far observed in the paleomagnetic record, we computed this misfit measure as a function of paleolatitude. We then picked the paleolatitude that minimized this misfit value (Fig. S4B) and calculated the probability p that $\chi^2(df = 2)$ exceeds that minimum misfit value (Fig. S4A). This probability represents the chance of observing at least the misfit between our observed polarities and the field inclination given a particular value of $G2$ and $G3$. Therefore, regions of $G2$-$G3$ space where p<0.05 are not supported by our observed polarities at the 2σ level.

In addition to this inclination constraint, the directional stability of the field (PSV) can constrain its total dipolarity. Based on a combination of empirical time-averaged field histories and numerical dynamo models, Biggin et al. (23) identified an empirical relationship between dipolarity D of the field and the Model G "a" parameter, which is the average VGP dispersion S_B (see above in Appendix S1.4, "*Paleopole data analysis*") at its minimum along the magnetic equator:

$$\log_{10} D = (-2.26 \pm 0.13) \log_{10} a + (3.44 \pm 0.16) \quad (7)$$

where the dipolarity D is the power ratio of the dipole to multipole terms, here simplified to

$$D = 2/[3(G2)^2 + 4(G3)^2] \quad (8)$$

The true value of the "a" parameter is unknown since it is defined at the equator (the minimum of S_B versus paleolatitude) while our pole was measured from moderately high paleolatitudes. However, our measured VGP dispersion $S_B = 24.6 \pm 12.2°$ serves as a conservative upper bound for the "a" parameter. Since the true value must be $a \leq S_B$, the value of D calculated from it is a lower bound. Taking advantage of this constraint, we constructed a map of the probability that the field was at most as dipolar as each point in $G2$-$G3$ space, yielding an elliptical confidence region surrounding the origin (Fig. S4C). To incorporate uncertainties in the values of S_B and the coefficients in Eq. 7, we applied a simple Monte Carlo resampling scheme ($N=10^5$) to these parameters when constructing the map.

We combined the dipolarity constraints from both the measured polarity inclinations and the directional stability of the field by multiplying their respective probability maps together, producing a joint probability map constraining the nondipole terms of the geodynamo (Main Text Fig. 6; Fig. S4D). As above, values of p<0.05 are statistically incompatible with the data.

S1.6. Microscopy. To identify the remanence-carrying magnetic grains we observed oriented sections of several cores with the quantum diamond microscope [QDM (24)] at the Harvard Paleomagnetics Laboratory, as in Brenner et al. (5) (see Figs. S7-S12). The QDM uses optically-detected magnetic resonance (ODMR) spectroscopy of nitrogen-vacancy (NV) centers in a diamond to produce maps of the surface vector magnetization on the samples with several mm field of view and several μm resolution. From each sample, we prepared a 0.03-1.5 mm thick 25 mm diameter disk and polished its upper face using 1 μm Al_2O_3 grit, taking care to avoid overprinting the sample's NRM. Placing the polished face of our samples in contact with the sensing diamond, we measured the magnetic field intensity along the [111] direction of the diamond crystal lattice using projective magnetic microscopy [PMM (24)]. We isolated the magnetic field signal of the ferromagnetic grains by measuring the sample successively under two mutually anti-parallel 0.9 mT bias fields canceled to <400 nT effective bias field and computed the out-of-plane (B_z) magnetic field using a spectral algorithm (25).

For one sample with a representative magnetic texture in vesicles (KUB2) we also conducted an abbreviated demagnetization routine (NRM, 10 mT AF, and thermal cycles to 330°C, 490°C, 520°C, and 560°C) and imaged a vesicle throughout with the QDM. Changes in the surface field pattern during demagnetization captured the unblocking of the phases hosting the imaged magnetizations (Fig. S10). To measure the changes in the field pattern and tie them

to remanence unblocking, we followed the methods of Volk et al. (26). In brief, this involved identifying regions of strong positive NRM surface field, and calculating the proportion of pixels within these regions that remain positive in these patches over the course of the demagnetization sequence. The resulting area fraction of remaining positive field is a proxy for the degree of remanence unblocking: a fraction of 1 reflects no change in the magnetization pattern and thus no unblocking, while a fraction of 0.5 reflects no statistical dependence of the field map on the NRM map (i.e., a randomized field pattern) and thus a fully unblocked remanence. Temperature intervals over which this fraction decreases substantially therefore indicate unblocking of magnetized phases.

Once we located magnetic sources in micromagnetic maps, we used a Horiba Scientific XploRA Plus Raman microscope (532 nm excitation wavelength) in the Harvard Laboratory for Mineral Physics to identify the mineral phases surrounding them, thus providing petrographic context for the source(s) of remanence. In sample KUB1, we also measured Raman spectra from reduced carbonaceous matter in calcite inclusions (Fig. S7, K and L). We calculated estimates of peak alteration temperature from these inclusion spectra following the five-peak curve fitting methodology of Kouketsu et al. (27). Where necessary, we also imaged magnetic phases with a JEOL JSM-7900F Schottky field emission scanning electron microscope, always imaging using backscattered electrons (BSE) with accelerating voltage 15-20 kV.

We also compared the observed replacement minerals and textures with those of a modern analog. This analog is the Gainesville East Sheet, a ~0.200 Ga layered diabase sill located in the Culpeper Basin, Virginia, USA (28-30). Author A. Brenner collected samples from a late orthopyroxene cumulate horizon within this sill on a field trip with members of the Northern Virginia Mineral Club in March 2010. These samples were all from a ~10 meter seam of infilled cavities in Bench #80 of the Vulcan Materials Company Manassas Quarry in Manassas, Virginia [approx. location 38.771°N, 77.526°W (31)].

Petrographic observations and results are treated in detail below in Appendix S4, "*Magnetization timing from alteration mineralogy*."

S1.7. Geochronology. We used the laser-ablation split-stream (LASS) inductively coupled plasma mass spectrometry (ICP-MS) facility at the University of California Santa Barbara to collect petrochronology data from titanites *in-situ* on selected polished sections [(32); Fig. S11; see below Appendix S4.5; "*Titanite petrochronology constraints*"]. This included U-Pb analyses made with a Nu Instruments Plasma HR multicollector ICP-MS, and trace-element analyses made with an Agilent 7700s quadrupole ICP-MS, both fed by ablation from an Analyte Excite 193 nm laser equipped with a HeLex two-volume cell. All analytical spots were 30 μm in diameter, ablated at 4 Hz for 15 seconds each with fluence ~1 J/cm^2, following a 2 shot pre-ablation and 20 second baseline. The primary U-Pb reference material (RM) used was MKED1 [1517 Ma; (33)]. In addition, materials Y1710C5 [390 Ma; (34)], BLR [1047 Ma; (35)], Fish Canyon [28.4 Ma; (36)], and TCB [1016 Ma; (37)] were analyzed for quality control, and yielded ages of 390 ± 2 Ma (n=7), 1040 ± 4 Ma (n=12), 28.2 ± 0.5 Ma (n=7), and 1017 ± 6 Ma (n=4), respectively. For the trace-element RM, we used NIST612, assuming 19.2 wt% Ca. We propagated an additional 1% uncertainty in the $^{207}Pb/^{206}Pb$ and $^{238}U/^{206}Pb$ ratios of all unknowns, since this uncertainty is all that is required for all U-Pb reference materials to yield values of age MSWD ≤ 1. Following this 1% uncertainty propagation, secondary RMs were within 1% of their accepted values, suggesting the absolute age uncertainties of our individual unknowns are also within 1%, or ca. 30 Ma. We reduced all data using Iolite v3.5 (38), and calculated Concordia ages in IsoPlot v4.1 (39). For all age calculations, we used decay constants of $\lambda_{235} = 9.8485\times10^{-10}$ yr^{-1} and $\lambda_{238} = 1.55125\times10^{-10}$ yr^{-1} (40). All uncertainties and error ellipses reported herein are 2σ, and all reported ages are lower intercept ages anchored to the common Pb composition of $^{207}Pb/^{206}Pb = 1.13$ expected for ~3.2 Ga rocks (41).

We performed 120 analyses on titanites from three polished sections from two samples (KUB1, KUB2) from site KUB1 (Fig. S11; see below Appendix S4.5, "*Titanite petrochronology constraints*"). Of these, we excluded from further calculations one analysis with <15% Ti, 12 analyses with >5% reverse-discordance, and 14 analyses in the top 10% of age errors (excluded 2σ age errors >546 Ma). Analyses on five grains containing up to 30% actinolite inclusions visible on their pre-ablation surfaces were not distinct from the array of U-Pb compositions of inclusion-

free analyses, so we did not exclude these analyses. The resulting compilation of 93 analyses showed evidence for minor post-crystallization Pb-loss, so we performed a two-component Gaussian deconvolution of their age distribution using the algorithm of Sambridge and Compston (42) implemented in Isoplot v4.1 (39). This calculation resolved age peaks at 3028 ± 19 Ma (36 ± 15% of analyses) and 3223 ± 23 Ma (64 ± 15% of analyses), with relative misfit 0.851 (Fig. S11E). Deconvolution assuming more than two age components did not result in appreciable improvement in the goodness of fit. We interpret the older, ~3.22 Ga age as the age of crystallization of the titanite population (consistent with the lowest overlap of analyses with the Concordia at up to 3.20 Ga), and the younger, ~3.03 Ga age as the maximum age of Pb-loss in some of the population (see below Appendix S4.5, "*Titanite petrochronology constraints*").

Appendix S2: Geologic setting

S2.1. Previous paleomagnetic work. High-confidence paleomagnetic poles have robust paleohorizontal corrections and make use of field tests to reliably constrain magnetization ages, and are therefore suitable for APW reconstructions. Poles older than 2.7 Ga that satisfy these requirements have thus far been measured in only two crustal blocks, the East Pilbara Craton of Western Australia and the Kaapvaal Craton of South Africa. Of the Archean poles from the East Pilbara, the youngest are those of the 2.772-2.710 Ga Fortescue Large Igneous Province, a sequence of flood basalts that formed the initial cover sequence across much of the Pilbara Craton as it moved across high latitudes (10-12). Notably, these rocks define a laterally-continuous magnetic stratigraphy, with mainly "normal" polarity magnetizations punctuated by two "reversed" intervals that pass a reversal test and define the oldest robustly-identified polarity reversal at ~2.77 Ga [poles "P1" and "P2"; (10, 43, 44)]. Another pole "HEBh" was recently measured from the 3.192-3.176 Ga Honeyeater Basalt (5), placing the Pilbara at mid-latitudes (Main Text Fig. 4). The oldest poles are those of the 3.350-3.335 Ga Euro Basalt ["EBm," (6); Main Text Fig. 4] and 3.471-3.464 Ga Duffer Formation ["DFM," (45)], both of which place the East Pilbara at low latitudes.

Several studies have argued for the operation of plate tectonics in the Archean based on the implied latitudinal motion between several of these poles (5, 10). In particular, the 36° latitudinal disparity between the Euro Basalt and Honeyeater Basalt has been interpreted as the earliest known evidence for long-range plate motion (5). The ~160 Myr age gap between these two units requires that the average rate of latitudinal motion during this interval was ≥0.23°/Myr, comparable to those of modern plate motions. However, the timing of this motion within the intervening 160 Myr – and thus whether the East Pilbara traversed the latitudinal distance slowly over the entire interval or in a brief episode of relatively rapid motion – has until now been unclear. In addition to latitudinal motion, vertical axis rotation of the East Pilbara is likely during the 3.34-3.18 Ga window, though structural block rotations around 2.93 Ga complicate this comparison (see below, "*Structural uncertainties and corrections*").

The plate motion history of the East Pilbara Craton during the 3350-3180 Ma interval would benefit greatly from paleomagnetic study of a nearby unit of intermediate age and structural history. This motivates the present study of the 3.275-3.249 Ga Kunagunarrina Formation, a sequence of up to 2.4 km of komatiitic to basaltic lavas exposed throughout the western East Pilbara (46-49) (Main Text Fig. 1). This unit is the central part of the ~3.29-3.23 Ga Sulphur Springs Group, overlying the siliciclastic sediments and felsic volcaniclastics of the ~3.29-3.255 Ga Leilira Formation, and underlying the felsic volcanics of the ~3.255-3.235 Ga Kangaroo Caves Formation (47, 48). The latter is coeval with the 3.257-3.235 Ga voluminous granitoid intrusions of the Cleland Supersuite throughout the East Pilbara and hosts notable 3.265-3.235 Ma volcanic-hosted massive sulfide (VHMS) deposits developed during hydrothermal circulation on the Paleoarchean seafloor [Main Text Fig. 1; (47, 48, 50-54)]. Crucially, the Kunagunarrina Formation is well-exposed in the SVS (Main Text Fig. 1, Fig. S1), enabling a more direct comparison of its paleo-rotation state with respect to the 3.18 Ga Honeyeater Basalt several kilometers upsection.

Several previous studies from ~3.2 Ga rocks in the Kaapvaal Craton of South Africa have claimed detections of geomagnetic reversals around 3.2 Ga, and are worth examining for comparison with the reversal measured herein. The first of these studies measured two intrusive phases that form the interior and margin of the Kaap Valley Tonalite (55), a 3229 Ma pluton bordering the Barberton Greenstone Belt (56). The authors observed that the interior and margin hosted steep, antipodal steep magnetizations, and proposed that these resulted from a polarity reversal that occurred during inward cooling of the pluton as late as ~3214 Ma. Another, shallower pair of opposing polarities were found shortly thereafter and interpreted similarly (57) from the adjacent and coeval 3235-3215 Ma Nelshoogte Pluton (56).

However, this work also identified an early Proterozoic overprinting magnetization (termed B+ and B-) within the Nelshoogte Pluton (57). This shows that merely identifying a dual-polarity magnetization is insufficient to demonstrate a primary origin, invalidating the use of the reversal test to make this claim. Since plutonic paleomagnetic data lack critical internal quality checks such as the ability to compare within-cooling-unit and among-cooling-unit scatter and the

lack of structural controls between sampling localities, the ineffectiveness of the reversal test is expected. For example, progressive, heterogeneous cooling or chemical alteration over any subsequent time span with a reversing dynamo can result in an apparently passing reversal test.

Further, the earlier Kaap Valley and Nelshoogte data were probably contaminated by viscous overprints since the magnetic mineralogy of the tonalitic host rocks was dominantly multi-domain magnetite as inclusions within magmatic hornblende (58). Subsequent work employed oriented single-crystal paleomagnetic methods to determine paleofield directions and intensities from ensembles of single-domain magnetite inclusions within magmatic quartz and microcline grains of the Kaap Valley Tonalite (58). Again, two directional polarities were isolated, albeit discordant with those originally identified from whole-rock methods (55).

A number of complications preclude the positive identification of a reversal from these results. While qualitatively antipodal, the single-crystal polarity-mean directions are distinguishably asymmetric by 32.5°, failing a paleomagnetic reversal test (44). Additionally, studies of the Kaap Valley Tonalite report their directions from sites along the margins of the pluton (55, 58), where a post-magmatic solid-state foliation fabric is strongly developed parallel to the pluton's contact with country rocks (56). A similar fabric, alongside a variably-developed lineation, is present throughout the Nelshoogte Pluton (56). These post-emplacement fabrics make a straightforward primary interpretation of the measured directions difficult and permit two scenarios for the relative timing of magnetization. If the temperatures attained during foliation exceeded the <580°C unblocking temperature of the magnetite carriers, then the measured remanences date to cooling following the deformation at the earliest. Alternatively, if peak metamorphic temperatures were below the unblocking temperature, then the bulk shear that formed the foliation would have rotated primary magnetizations by unknown amounts that depend on the local foliation attitude and degree of deformation. This rotation would be highly non-uniform over the m-to-km length scales between samples and localities. Since the magnetizations are directionally-coherent and do not show evidence for this style of rotation, they would therefore be overprints recorded after the foliation event. In either case above, the magnetizations must record the paleofield following or contemporaneous to fabric development events, and thus are overprinting magnetizations of unknown age. In addition, as discussed above, the inability to compare magnetizations among cooling units and the lack of structural controls between sampling localities implies that reversals during later remagnetization events can be recorded as apparently reversed directions. In the Barberton Greenstone Belt, these may include intrusive and regional metamorphic events at 3.1, 2.95, 2.8-2.6 and 2.09-2.03 Ga (59, 60). For these reasons, we regard evidence from the Kaapvaal Craton for a >3 Ga reversal as intriguing but inconclusive. These works aside, the oldest robustly-identified reversal is that of poles P1 and P2 of the Fortescue Province (10).

S2.2. Structural uncertainties and corrections. While recovering a crustal block's paleolatitude from magnetic directions in stratified rocks requires only a tilt-correction to restore measured bedding attitudes to paleohorizontal, recovering its paleo-rotation state requires both tilt-correction and corrections for later structural events that deformed and rotated the measured rocks. Structures that require such corrections include plunging folds and panels that rotated relative to their surroundings. Care must be taken to identify these structures and quantify their implied vertical axis rotations. Poles EBm and DFM do not require additional corrections for such structures, since bulk deformation at their measurement locations are limited to simple doming (e.g., EBm was measured one the edge of the rotationally-stable Carlindi Batholith), without identifiable rotation or shearing (61).

Poles KUH-R and HEBh, however, require several corrections. Both are measured in the Soanesville Syncline (SVS; Main Text Fig. 1, Fig. S5), a northeast-plunging open fold that occupies a structural panel within a broad zone of sinistral shear and wrench faulting that meanders north-south across the western East Pilbara. The SVS and its parent shear zone both formed between 2.94 and 2.93 Ga via regional northwest-southeast compression during the 2.955-2.919 Ga North Pilbara Orogeny, which resulted in much of the structural character of the Pilbara Craton (15, 48). The timing of these events is constrained by dating of synkinematic granitoids (15, 62). The following sequence details, in order, the structural events that led to the present-day SVS, illustrated in Fig. S5 and based on previous structural mapping (15, 63):

- The SVS and its surroundings were displaced to the northwest and rotated clockwise along a bend in the fault system bounding the shear zone to the west (Fig. S5, A-B). The exact amount of rotation experienced by the SVS during this event depends on its unknown initial position relative to the bend in the fault, but the 70° angle subtended by the bounding fault sets an upper bound on the clockwise rotation of the SVS area. The lower bound is 0°, or no rotation, which corresponds to limited displacement along the fault. This rotation affected the measurement locations of poles KUH-R and HEBh equally.
- Narrowing of the shear zone to the north blocked further northward displacement of the rocks north of the SVS, while pinching of the shear zone to the south continued to displace the rocks to the south of the SVS northwards. The resulting northwest-southeast compression resulted in a series of syncline-dominant, parallel, open folds trending 069° E of N, the largest of which is the SVS itself (Fig. S5, B-C). Ramping of the SVS up the sloped eastern margin of the dome to the west plunged the SVS 41° to the NE, resulting in a fold axis with trend/plunge 069°/41°. The measurement locations of poles KUH-R and HEBh both experienced this deformation equally.
- The final stages of northwest-southeast compression displaced the SVS slightly to the northwest along the bounding fault to its west, causing drag folding of its western margin (Fig. S5, C-D). This rotated rocks in the western portion of the SVS block counterclockwise, resulting in bending of the southwestern segment of the SVS axial surface by about 60° at its extreme southern end. Our samples at localities KUA and KUT experienced 40° of counterclockwise rotation during this event, and KUB experienced a 52° rotation, as evidenced by the mappable surface trace of the SVS axis determined from tracing of marker horizons and faults (Fig. S5, C and D). Meanwhile, samples from pole HEBh experienced no rotation during this stage.

The corresponding sequence of corrections to recover fully-restored paleomagnetic directions from the *in situ* directions of KUH-R and HEBh are as follows (Fig. S5):

- **A 40° clockwise rotation to KUA+KUT directions only, and a 52° clockwise rotation to KUB directions only.** To correct for late-stage drag folding and restore the southwestern portion of the SVS axis to the same 069°/41° trend/plunge as the northeastern SVS, all magnetization directions and bedding attitudes from KUH-R (this study) must be rotated clockwise around a vertical axis between 40° and 52°. For later tilt-corrections, we also rotated the bedding attitudes at each locality by the corresponding 40-52°. This correction is not applied to pole HEBh.
- **A 41° horizontal-axis rotation to unplunge the SVS, followed by bedding tilt correction.** To correct for the folding of the SVS, all magnetization directions and bedding attitudes from poles KUH-R and HEBh must then be "unplunged" by rotating 41° about a horizontal axis with trend 159°. Directions must then be tilt-corrected by restoring local bedding attitudes to the horizontal plane. This results in fully-tilt-corrected directions, as shown in Main Text Fig. 2E and Table S1. The fold test on the H component (Fig. S2B) was performed using the tilt-correction portion of this stage of rotation.
- **A 0-70° counterclockwise rotation.** Finally, to correct for early block rotation of the SVS region, all unfolded magnetization directions from poles KUH-R and HEBh must then be rotated counterclockwise around a vertical axis between 0° and 70°, depending on how much displacement of the SVS occurred during initial 2.93 Ga structure formation. For our preferred APW path and reconstruction (Main Text Fig. 4; see rationale below in Appendix S2.3, "*Geomagnetic polarity ambiguities*"), we choose a value of 20° for the magnitude of this correction, which nullifies implied rotational motion of the East Pilbara between poles EBm and KUH-R. For alternative proposed APW paths and their corresponding reconstructions (Fig. S6) we instead adopted the full range of corrections between 0° and 70° to explore how the reconstruction(s) change upon varying this uncertain rotational correction within its full allowable range. It is important to note that while ambiguity in this correction changes the paleo-rotation states of poles KUH-R and HEBh *with respect to all other East Pilbara paleopoles*, the paleo-rotation states of poles KUH-R and HEBh *with respect to one another* are unaffected, since the correction applies to both poles equally. Comparison of these two poles with those measured outside the SVS depends on the magnitude of this correction.

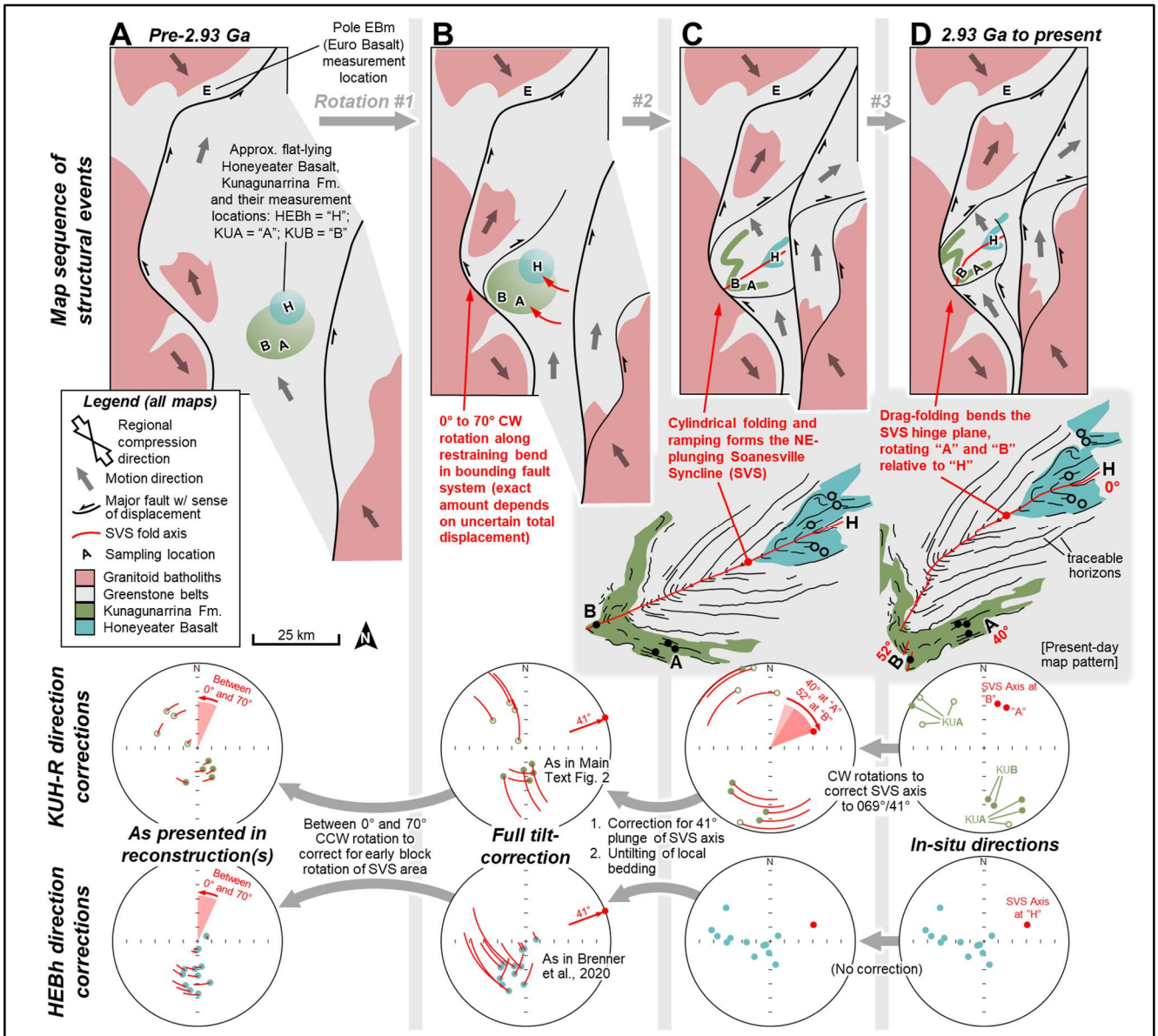

Figure S5. Corrections for structure formation. The sequence of structure-forming events at ~2.93 Ga in the Soanesville Syncline (SVS) region and surroundings (map views in top row) and the corresponding sequence of corrections for paleomagnetic directions from pole KUH-R (top row of stereonets, measured from points "A" and "B" on maps, this study) and pole HEBh [bottom row, point "H" on maps, Brenner et al. (5)]. For reference the measurement point of pole EBm from the 3.34 Ga Euro Basalt (6) is also shown (point "E"), and the only necessary correction to its directions is a simple tilt correction. The sequence of events is based on mapping of this region by Van Kranendonk et al. (63) and Van Kranendonk (15). Structures formed in this timeframe are tied to displacements along a system of curvilinear faults (black curves) that defined a regional sinistral shear zone developed between converging granitoid batholiths (pink). The SVS area was one of the structural panels in this shear zone. Rotations in the SVS occurred in the following sequence based on mapping work (15, 63). First, the area rotated between 0° and 70° clockwise as it moved along a curved fault system bounding the western margin of the shear zone (Rotation #1, **A-B**); the exact amount of rotation within this range depends on the unknown initial position of the SVS and its resulting total displacement along the fault system. The SVS was then folded into a series of NE-plunging open folds as wrench faulting compressed

it NW-SE during narrowing of the regional shear zone (Rotation #2, **B-C**). Finally, late-stage drag folding rotated the western margin of the SVS block counterclockwise, as evidenced by bending of the SVS hinge plane (Rotation #3, **C-D**, and approximately-reconstructed and present-day inset maps of the SVS). Our samples from KUA (point "A" on maps) experienced 40° of this rotation, and KUB ("B") experienced 52°, while HEBh experienced no rotation during this stage.

S2.3. Geomagnetic polarity ambiguities. The unknown relative reversal states of each paleopole with respect to one another introduce an additional ambiguity, since the "pole" in each paleomagnetic dataset is the north *geomagnetic* pole, but may correspond to either the north or south *geographic* pole thanks to the demonstrated ability of the field to spontaneously reverse its dipole component. Therefore, the true paleolatitude and paleo-rotation state of a crustal block are either (a) those calculated directly from the measured paleopole, say "POLE", assuming it is the north geographic pole, or (b) those calculated from the paleopole's inverse, "POLE-R", which results in a paleolatitude of opposite sign and a paleo-rotation state flipped 180°.
In the Archean, the absence of a calibrated continuous geomagnetic polarity timescale means that we cannot determine absolute reversal states, leading to many combinations of normal vs. reversed paleopoles and thus many *possible* motion reconstructions (Fig. S6). However, the parsimonious assumption that rapid motions were less likely between sequential paleopoles substantially reduces the space of *conservatively plausible* reconstructions. In this work, "plausible" reconstructions are those that require no more than ~1°/Myr motion. For instance, poles KUH-R and HEBh are only 26° apart, and happen to imply the same paleolatitude of about 43°, so we can reasonably suggest that they likely record the same reversal state and thus very little motion in the intervening ~65 Myr. Phrased alternatively, it would be highly unlikely that these two poles sample opposite reversal states but coincidentally record large, ~2.2°/Myr motions that happen to produce opposing poles.

The final ambiguity is thus whether pole EBm records the same or opposite geomagnetic reversal state as poles KUH-R and HEBh, a comparison complicated by the structural rotation of the SVS examined above. However, we can again filter the possible scenarios by considering those that result in the least motion. If EBm measures the same geomagnetic polarity as KUH-R/HEBh, the maximum possible SVS structural correction of 70° results in the least rotational motion between the two pole pairs. However, this scenario requires ~95 Myr of 1.4°/Myr rotation (Fig. S6B, model #5). Alternatively, if EBm was reversed with respect to KUH-R/HEBh, then an SVS structural correction of 20° results in the least motion (no rotation and 0.55°/Myr latitudinal drift). This scenario corresponds to our preferred reconstruction (Main Text Fig. 4).

We conclude that the 3.25-3.18 Ga KUH-R and HEBh poles very likely share the same geomagnetic polarity, while the 3.34 Ga EBm pole likely sampled the opposite reversal polarity. Whether a reversal took place between the two pairs of poles is unknown, and the degree of relative rotation between the two pole pairs is constrained but has a large range of uncertainty. Even so, accounting for these ambiguities results only in reconstructions that feature major latitudinal and/or rotational motions between these two pole pairs (≥0.55°/Myr). Further, the 3.25-3.18 Ga pole pair documents major rotational motion (0.55°/Myr) that does not depend on unknown structural corrections, and probably also on relative reversal states. Therefore, while vertical axis rotations and reversal state uncertainties complicate motion rate calculations, the conclusion that substantial motions of the East Pilbara occurred at ≥3.25 Ga is unaffected.

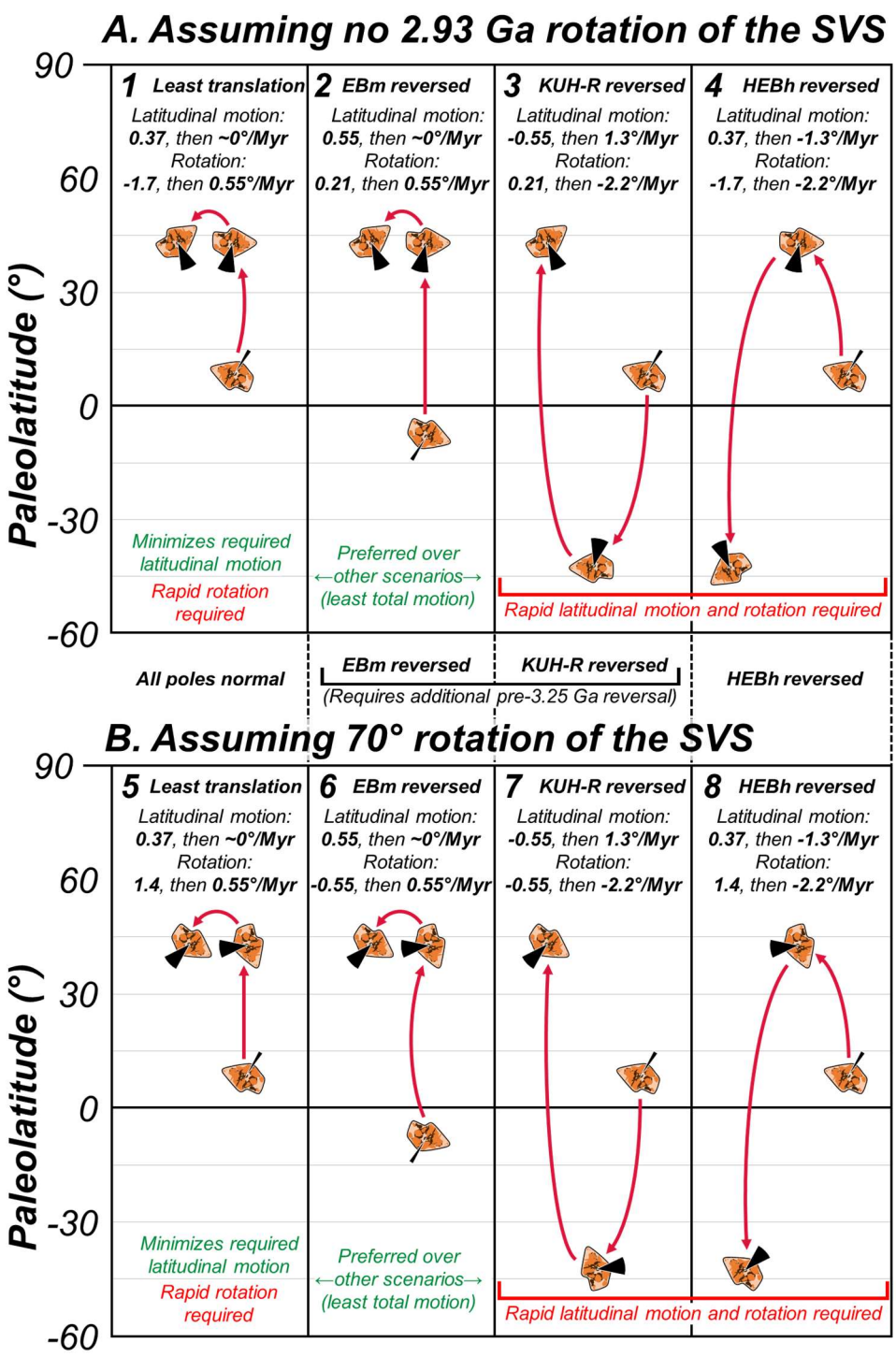

Figure S6. A more complete visual exploration of possible reconstructions given reversal state ambiguities. Panels are drawn as in Main Text Fig. 4B. Each panel corresponds to an endmember structural correction for the SVS poles KUH-R and HEBh, and columns tied across the two panels correspond to scenarios in which the poles sample various reversal states relative to the other poles. Reconstructions in panel **A** prescribe the minimum possible structural rotation (0°) of the SVS block at ~2.93 Ga, while those in **B** prescribe the maximum possible structural rotation (70° clockwise). Models 2 and 6 are similar to our preferred reconstruction (Main Text Fig. 4B), while all other models display substantially greater total motion.

Appendix S3: Magnetization timing from paleomagnetic field tests

S3.1. Fold test. Our sampling permitted fold, conglomerate and reversal tests that constrain the timing of magnetization via cross-cutting relationships. After structural and tilt corrections to (a) straighten the bent SVS hinge plane, (b) un-plunge the axis of the SVS [trend/plunge = 069°/41° (15)] and (c) restore local bedding at localities KUA and KUB (see above Appendix S2.2 and Fig. S5 for details), the site-mean H component direction clusters from the lowermost sites in KUA and both sites in KUB merge (Main Text Fig. 2E). Moreover, all nine resolvable site-mean H components pass a fold test (13) implying a best-fit untilting value of 87% 108% (2σ) (Fig. S2B). Since the fold test requires a single unfolding correction, we performed this fold test over the final tilt-correction step, *after* correcting directions and bedding attitudes for SVS hinge plane plunging and bending. The H magnetization thus pre-dates folding of the SVS at ~2.93 Ga.

S3.2. Reversal test. Structural correction of H components from the upper half of the sampled stratigraphy (sites KUA5-9) results in a cluster of northwest-upward directions in tilt-corrected coordinates (D, I = 329.8°, -53.3°; α_{95} = 24.1°; Main Text Fig. 2E; Table S1). Three samples from site KUA7 (a dolerite sill) host a similar direction, although these directions are too scattered to yield a precise mean, likely due to multidomain behavior of magnetic recording phases within the more coarsely-crystalline sill (Fig. S7, D and E). A notable feature of the KUA5-9 direction is its approximate antipodality to the mean direction of all other sites, which is 160.1° away (D, I = 183.2°, 63.4°; α_{95} = 13.6°; Main Text Fig. 2E; Table S1). We consider several possible origins for these approximately antipodal H component clusters:

1) **A regional Paleoproterozoic overprint.** The mean direction of sites KUA5-9 is somewhat similar – albeit shallower in *in situ* coordinates – to that of the regional overprint carried by the M component, and is quite similar to directions from ~1800-1700 Ma rocks in the Western Australian cratons (3, 64), potentially indicating an overprint origin. However, many samples carry distinguishable M and H components. This is particularly evident for samples carrying the M2 component, especially at sites KUA5 and 9. In these samples the M component partial thermoremanent magnetization (pTRM) overprints M2, which in turn overprints H. This demonstrates that the H component is distinct from the M component, and that acquisition of the H component substantially pre-dates that of the M component. In addition, given the similarity of the M2 overprint direction to that of the ~2.78 Ga Fortescue P0 pole (43), the overprinting relationships above demonstrate that the H component age is ≥2.78 Ga.
2) **Local remagnetization by the sill at KUA7.** Since site KUA7 is a dolerite sill of unknown age, and captures a similar paleofield direction to that of sites KUA5-9, we must consider whether the direction recovered from the neighboring sites reflects thermal remagnetization by the sill up to ≥580°C. The sill is ~15 m thick (Main Text Fig. 1B, Fig. S1C), and since site KUA6 is only 1-2 sill-widths away from the intrusion, it was probably at least partially remagnetized during intrusion of the sill. This is supported by the petrography of site KUA6, in which all magmatic clinopyroxene grains are fully recrystallized into fine chlorite (Fig. S7F). This mineralogy reflects a uniquely advanced degree of alteration among the sampled lavas, and is restricted to site KUA6, and thus most likely originated during baking by the sill at KUA7. In contrast, sites KUA8-9 are 3-5 sill-widths away, and KUA5 is 10 sill-widths away. None of these sites display the enhanced alteration evident in the baked zone at site KUA6, and retain alteration mineralogies indicative of lower greenschist facies conditions. The sill therefore could not have remagnetized sites KUA5, 8 and 9 during its emplacement.

   The sill at site KUA7 could have several possible ages. Documented dikes in the area belong to the ~1.07 Ga Round Hummock and ~0.755 Ga Mundine Wells Dike Swarms (11, 15, 65), both of which would imply paleofield directions that do not agree with that of sites KUA5-9 (Round Hummock D, I ~ 335°, 35°; Mundine Wells D, I = 014°, -36°). While three small dolerite dikes of ~1.8 Ga age have been mapped some 300 km away in the far western Pilbara Craton (66) – a time at which the paleofield direction would approximately match that of sites KUA5-9 – they have not been documented from the Meso-Paleoarchean core of the East Pilbara terrane, making this age unlikely. Dolerite sills from the ~3.18 Ga Dalton Suite are common throughout the field area, but would host a magnetization of similar direction to

that of the comagmatic Honeyeater Basalt (5), which is not the case here (Honeyeater Basalt D, I = 204°, 59°). Thus the remaining possible age for KUA7 is shortly after eruption of the surrounding lavas, meaning sites KUA6 and 7 share the hydrothermal alteration and magnetization history of the neighboring sites KUA5, 8 and 9.

3) **Magnetic self-reversal.** Rocks may spontaneously reverse their magnetizations in rare situations where their magnetic carrier phases either (a) are titanomaghemites that contain substantial substituent titanium (x ~ 0.4-0.6) and have experienced low-temperature oxidation (67, 68), or (b) are present at a very high volume density such that grains regularly experience magnetic backfield from neighboring grains. The former is typically observed in intermediate to felsic volcanic rocks, which can host Fe-Ti oxides with the correct Ti substitution and oxidation state. However, since the H component unblocks up to ~580°C, it cannot be carried by titanomaghemites with x > ~0.3 (69). Together with textural observations, this shows that the magnetic carrier phases are instead nearly pure magnetite that recrystallized from primary Fe-Ti oxides, and are not oxidized enough to have experienced this style of self-reversal. Further, the NRM intensities of our samples (up to ~0.1 A/m) are all well below the threshold at which most magnetized grains experience substantial backfield from neighboring grains. Self-reversal is therefore very unlikely.
4) **A Paleoarchean reversal captured by episodic hydrothermalism.** Since sites KUA5-9 are stratigraphically above all other sites, their approximately antipodal direction could reflect a magnetic reversal that occurred soon after magnetization of sites KUA1-4 and KUB1-2, but before that of sites KUA5-9. This interpretation requires the two "polarities" to be statistically indistinguishable from antipodal, forming the basis of a reversal test (16). The measured polarities are indeed consistent with antipodality, as they are asymmetric by 19.9°, within the requisite critical angle of 23.0°. The limited number of sites per polarity (5 and 4 sites each) and their scatter limit the discriminatory power of this test, which is classified as "indeterminate" since the critical angle exceeds 20° (16). That said, independent lines of evidence suggest a reversal origin of the antipodal directions. First, extensive petrographic evidence contextualizes the H magnetization as a hydrothermal TCRM acquired during episodic fluid flow that punctuated the eruption of the Kunagunarrina Formation (see below Appendix S4, "*Magnetization timing from alteration mineralogy*"). Field evidence based on hydrotthermal quartz horizons points in particular to two such major hydrothermal episodes, one occurring after the eruption of the lowermost sites and another occurring after eruption of the remaining sites with opposing polarity (Main Text Fig. 1; Fig. S1, A and B). In addition, titanite U-Pb alteration petrochronology places a direct lower bound on the age of the H component at ≥3.223±0.023 Ga, within tens of Myr of eruption (see below Appendix S4.5 and Fig. S11). Thus, detailed petrographic and lithostratigraphic context clarifies how a reversing H component may have arisen during episodic TCRM acquisition, which together with the narrow constraint on its timing, makes a reversal the only probable explanation for the observed polarity groups.

The elimination of much later regional or local remagnetizations and self-reversing behavior, coupled with the stratigraphic coherence and antipodality of the measured polarities, thus indicate that the H component records a geomagnetic reversal dating to hydrothermal alteration of the Kunagunarrina Formation between 3.265 and 3.235 Ga (see below Appendix S4, "*Magnetization timing from alteration mineralogy*"). In addition to defining the H component as an early remanence, a reversal of this age represents the oldest documented geomagnetic reversal, pre-dating the next-oldest robust example by ~480 Myr (10).

S3.3. Implications for paleofield stability. Since the H component is a hydrothermal TCRM acquired during early alteration (see below Appendix S4, "*Magnetization timing from alteration mineralogy*"), remanence acquisition was likely prolonged over tens to hundreds of thousands of years, enough to partially or fully average PSV (70, 71). Still, the precise relationship between the timescales of PSV and alteration are uncertain, precluding a definitive analysis of PSV based on the H component directions alone. Additionally, chemical remanences often record the paleofield less efficiently, thus introducing scatter that may give the appearance of greater PSV. That said, we observe that in nine of the ten sites that host an H component, the within-site scatter is less than the between-site scatter, and often significantly so. In the context of how samples are

collected, this shows that within the area sampled from each site (typically tens of meters or less), the timing of alteration and TCRM acquisition is much faster than within the sampled field area as a whole (hundreds of meters to km). This supports the assertion that individual "sites", while hosting TCRMs that are linked genetically to shared hydrothermal alteration system(s), are magnetized during separate time intervals and thus sample PSV in a fashion similar to the TRMs hosted by unaltered lavas, in which individual sites capture brief snapshots of the paleofield variability that can be averaged between sites. It is therefore worthwhile to use between-site variability to calculate the angular dispersion of site-mean virtual geomagnetic poles (VGPs) and gauge variability of the late Paleoarchean geodynamo. We calculate a PSV dispersion $S_B = 24.6 \pm 12.2°$ ($N = 9$ VGPs). These results are greater than ~10-20° dispersion results of similar antiquity (5, 20, 45) and from the last 5 Myr (72). Since these data are both derived from small samples, they may be biased towards lower values of S_B (73).

Also of note is the lack of so-called "transitional" directions among the site-means presented herein, as well as in pole HEBh (5). Such directions document excursions or periods between reversal states, and typically represent ~1-2% of sites in modern samples, corresponding to 1-2 reversals/Myr, each lasting ~0.01 Myr (74). The probability of observing zero transitional directions among the 20 VGPs sampled by poles KUH-R and HEBh, assuming the field was in transition 2% of the time, is $(1\text{-}0.02)^{20}$ ~67%, compatible with our observations. Alternately, if we set this probability to 0.05, we can calculate the maximum allowable fraction of the time the field was transitional within 2σ confidence, which for 20 VGPs is $1\text{-}(0.05)^{1/20}$ ~14%. This is comparable to the transitional field frequency in the Jurassic Quiet Zone, an interval in which a relatively unstable dynamo produced 10+ reversals/Myr and elevated PSV (75, 76). Thus, the lack of transitional field directions in our data reflects a paleofield at least as stable as the least stable field in recent geologic history, which itself was dominantly dipolar.

Appendix S4: Magnetization timing from alteration mineralogy

S4.1. Overview. Examination and dating of the petrological textures associated with the H component remanence reveal more about the mechanism and timing of its acquisition. We examined samples with well-developed H components from multiple sites. In this Appendix, we first characterize the mineralogy of our samples with Raman spectroscopy and optical and electron microscopy, and reconstruct the conditions of hydrothermal alteration that produced it, especially phases precipitated into void spaces (S4.2-4.3). We then present QDM mapping that ties our measured magnetizations to these mineralogical changes, thereby inferring the timing of magnetization relative to observed textures [S4.4; see above Appendix S1, "*Extended Materials and Methods*"; (77)]. Finally, we constrain the timing of magnetizing alteration to >3.223±0.023 Ga based on *in-situ* U-Pb dating of post-magnetization titanite (S4.5-4.7). This date, combined with the alteration sequence, field relations, and independent geological evidence, tie the H component magnetization to episodic seafloor hydrothermal alteration between 3.265-3.235 Ga.

S4.2. Ferromagnetic assemblages and their origin. The metamorphic mineralogy of all samples, identified via optical petrography and Raman spectroscopy, was produced via moderate hydrothermal alteration at up to ~330°C by fluids derived from seawater [Figs. S7 and S12; (78)]. All samples have retained primary igneous textures. Primary ferromagnesian silicate phases typical of komatiites, including skeletal olivines (Figs. S7B and S12E) and orthopyroxene cores of zoned spinifex-textured clinopyroxenes (Figs. S7I and S12F), have been replaced by chlorite (likely itself a replacement of serpentine) + magnetite with occasional further replacement by calcite. Carbonate replacement (Fig. S7, F-H and J-K) was dominant in sites KUA1-5, KUB1-2, and pervasive in locality KUT, whereas chlorite replacement (Figs. S7B and S12E) dominated in sites KUA6-9. Ubiquitously, clinopyroxenes of augite composition (Fig. S7, H and I; Fig. S12F), commonly skeletal or with skeletal embayments, are the only remaining primary mafic phases. Hydration-silicification replacement halos (sub-mm-scale) of actinolite after primary clinopyroxenes are common around vesicles, veins and along margins of otherwise-unaltered clinopyroxenes (Fig. S7, H and I; Fig. S12F). Actinolite is also common as inclusions in albite and in vesicles. Primary plagioclase microlites have been fully converted to albite (sodic alteration) ± epidote (saussuritization; Fig. S7E) ± chlorite (likely after sericite), and mafic glass was replaced by a groundmass of chlorite ± albite ± actinolite ± titanite (e.g., Fig. S7I).

Accessory minerals document similar conditions of alteration. Primary titanomagnetites are identifiable as trellised or dendritic pseudomorphs composed of ilmenite and titanite, occasionally also oxidized to anatase or "leucoxene" (Fig. S7, C and E; Fig. S12, B and C). These phases are commonly intergrown with magnetite that recrystallized via lamellar exsolution or encrustation of the original grains. Primary (magnesio-)chromites, many of which nucleated on vesicle walls (79), have been replaced by chromium-rich magnetite (Figs. S7A, S9D and S12D). The largest chromites (mm-scale) display "atoll" textures (Figs. S7A and S12D) of hydrothermal Si/Al/Fe/Zn enrichment and extreme Mg/Cr depletion (80). Accessory secondary phases include a diverse assemblage of Fe/Cu/Zn sulfides (Figs. S7J and S12A) that occur mainly in veins and vesicle infills (we directly identified pyrite, chalcopyrite, covellite, sphalerite, and galena, as well as magnetic detection of pyrrhotite in some samples).

Recrystallized titanomagnetite in the groundmass is worth further examination given its major contribution to the magnetization of unaltered basalts. In many cases, these titanomagnetites are preserved in intricate detail, particularly at site KUA4. Here dendritic networks of magnetite grains recrystallized from primary titanomagnetites are abundant within the recrystallized basaltic glass groundmass [Figs. S8 and S12C; cf. (81)]. The diverse morphologies of these grains are relics of those of the original skeletal crystallites, and include branched-rectilinear, plumose, ladderlike, and cruciform arrangements of 0.02-0.5 μm cuboctahedral "beads" and several-μm "bars" [Fig. S8, E-J; Fig. S12C; cf. (82)]. These textures are often intimately associated with titanite pseudomorphs after ilmenite with similar morphologies, albeit less finely-preserved. While the dendrites preserve primary textures, they were recrystallized during oxy-exsolution of original titanomagnetite (most likely ~$Fe_{2.3}Ti_{0.7}O_4$) to yield the assemblage magnetite and ilmenite, and then during hydrothermal alteration to yield magnetite, titanite, chlorite, and zeolites [Fig. S8; Fig. S12, B and C; (83)].

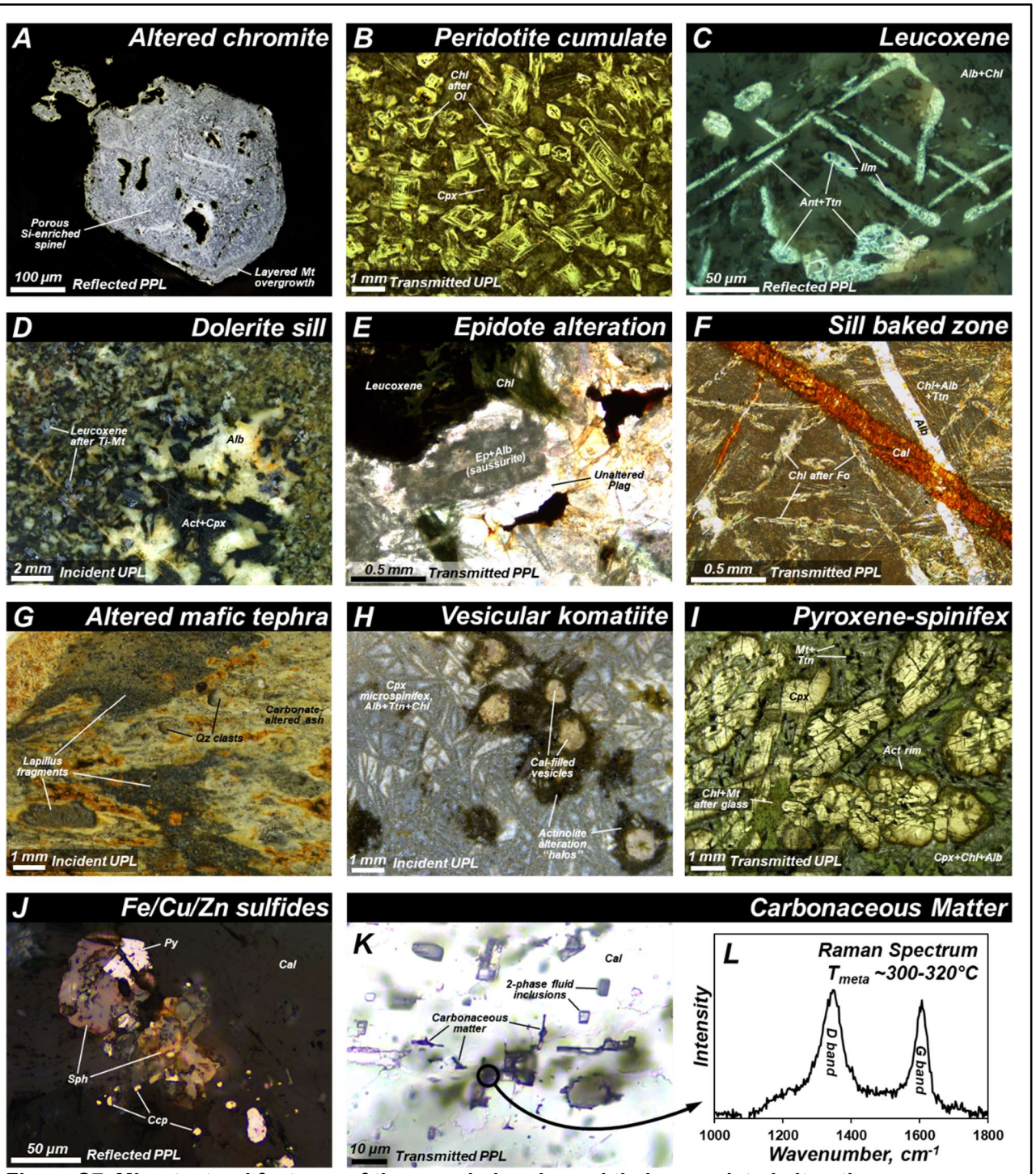

Figure S7. Microtextural features of the sampled rocks and their associated alteration mineralogies. A. "Atoll"-textured chromite grain in sample KUA62 (site KUA9) that has been hydrothermally altered to a porous Si, Al, Fe-enriched spinel. **B.** Peridotite cumulate from the base of the flow at site KUA9 (sample KUA62), showing strongly skeletal olivines altered to serpentine followed by chlorite and set in a groundmass of chlorite, actinolite and unaltered clinopyroxene. **C.** Leucoxene – an intergrowth of titanite, ilmenite and their weathering products (mainly the white titanium oxide anatase) – forms as an alteration product of original titanomagnetite grains in site KUA5 (sample KUA31). **D.** The dolerite sill at site KUA7 (sample KUA48) is coarser and more equigranular than the surrounding lavas. **E.** A coarse sample (KUA50) of the sill at site KUA7 contains plagioclase altered to epidote and albite

("saussuritization") during hydrothermalism. **F.** Site KUA6 (sample KUA41) is within the baked zone of the sill at site KUA7, and is strongly recrystallized, with no surviving pyroxene. It also displays multiple generations of cross-cutting veins consistent with the typical infill sequence of the rock package. **G.** Sample KUT20 shows the strong carbonate alteration of the tephra-lapillistone horizon at the center of our sampled stratigraphy. Altered scoria clasts and relatively unaltered quartz grains are entrained in the sheared, recrystallized ash matrix. **H.** Vesicles infilled by carbonate and haloed by actinolite are visible in sample KUA24 from the flowtop of site KUA4. The groundmass displays a microspinifex texture, with small clinopyroxene platelets that rapidly cooled from the komatiitic melt during eruption. **I.** Coarse pyroxene-spinifex texture in sample KUB6 from near the flowtop of site KUB1. Large clinopyroxene laths are abundant, many with skeletal embayments (e.g., center of the image), and most with orthopyroxene cores altered to serpentine + magnetite and then to chlorite + magnetite. Former mafic glass is now altered to chlorite and magnetite, and all pyroxenes exhibit alteration rims and fracture fills of actinolite. **J.** Complex assemblage of Fe/Cu/Zn sulfides within calcite infilling a vesicle in sample KUB2 (site KUB1). These sulfides and their host calcite are the final infill stage in the preserved prograde infill sequence. **K.** Inclusions of two-phase fluids and carbonaceous matter within calcite infilling a vesicle in sample KUB1 (site KUB1). **L.** Raman spectrum of the carbonaceous matter in Panel K, displaying two excitation bands corresponding loosely to disordered and graphitic carbon. The morphology of these spectral features indicates this inclusion experienced a peak maturation temperature of up to ~320°C, and other inclusions record peak temperatures up to ~330°C. Abbreviations used – XPL: cross-polarized light, PPL: plane-polarized light, UPL: unpolarized light, Mt: magnetite, Chl: chlorite, Ol: olivine, Cpx: clinopyroxene, Alb: albite, Ant: anatase, Ttn: titanite, Ilm: ilmenite, Ti-Mt: titanomagnetite, Act: actinolite, Ep: epidote, Plag: plagioclase, Cal: calcite, Qz: quartz, Py: pyrite, Sph: sphalerite, Ccp: chalcopyrite.

S4.3. Ferromagnetic assemblages in void spaces. A separate population of ferromagnetic minerals occur within vesicle infills, which also provide evidence for the timing and nature of the alteration. Calcite-filled vesicles occur in our samples throughout sites KUA2-4 and KUB1-2 and exhibit zoned infill mineralogy, offering a window into the timing and paragenetic sequence of alteration. Four sequential infilling phase assemblages can be distinguished petrographically (Fig. S9, A-C; Fig. S12A). The first, which we term "Stage 1," rims all veins and vesicles (Fig. S9, A and B; Fig. S12A), filling all but the largest (multi-mm) vesicles. While the present mineralogy of this material is pure calcite, this is an overprint from a later stage of infill ("Stage 4" below). By analogy with modern seafloor basalts, Stage 1 likely originally consisted of silica, chlorite, celadonite, saponite, or low-temperature Na-rich zeolites. All commonly precipitate as porosity-filling phases during "seafloor weathering" or burial in contact with water below ~150°C (78, 84).

The next phase assemblage, "Stage 2," consists of subrounded regions within the calcite infill that are adhered to the walls of large vesicles incompletely filled by Stage 1. These contain angular domains clouded by 0.03-0.7 μm magnetite grains (Fig. S9, A and B; Fig. S12A). These magnetites are elongated rods with aspect ratios between ~10:1 and 1:1 and are locally oriented along several preferred directions (Fig. S9, E and F). This texture is characteristic of magnetite exsolution from Fe-bearing silicates, particularly Ca-rich plagioclase, which is unstable with respect to Fe oxides at low temperatures (85). Stage 2 magnetites are thus grown within the remnants of ferroan plagioclase grains. Anorthite forms in these contexts in modern rocks closely associated with acicular, radiating "rosettes" of Ca-rich zeolites, which nucleate on void space walls upon alteration to ~250°C (84, 86). This morphology is consistent with the habit of Stage 2 material, which also occurs as "rosettes" adhered to vesicle walls. This phase assemblage thus documents the mobilization and redistribution of Ca^{2+} and Fe^{2+} from basaltic glass to new (Ca,Fe)-rich phases during the initial stages of hydrothermal alteration (84, 86, 87), along with partial oxidation of the Fe^{2+} to Fe^{3+} to form magnetite.

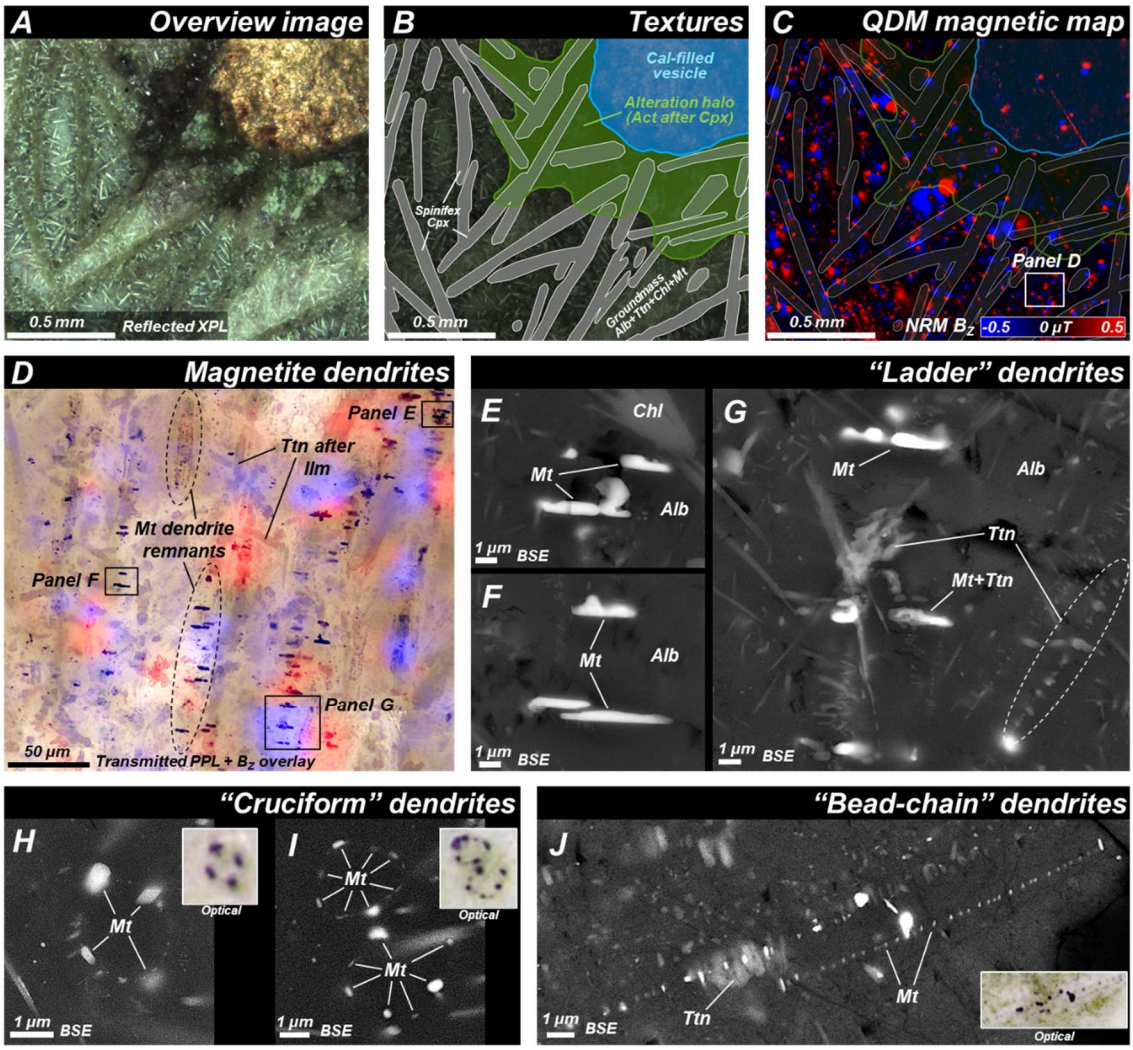

Figure S8. Magnetic mineralogy of altered primary titanomagnetite dendrites. (See Appendix S4.2). Panels A-C show the same field of view on sample KUA24. **A** is an optical image; **B** delineates the pyroxene-spinifex textured groundmass and its silicification/hydration to actinolite surrounding a calcite-filled vesicle; **C** is a QDM map of vertical magnetic field (NRM B_Z) over the sample surface. Most magnetic sources are associated with the matrix between spinifex clinopyroxene platelets. These sources are removed in the altered zone around the vesicle. **D.** Detail of magnetized sources in the groundmass, showing a variety of rectilinear "ladder-like" arrangements of magnetite and titanite. These formed first during rapid cooling of the komatiite flow as branched titanomagnetite dendrites, then recrystallized to yield magnetite and ilmenite, and then again to magnetite and titanite. **E-G.** BSE and optical detail images of dendrites in Panel D. **H-I** show another dendrite morphology, several-μm "cruciform" arrangements of four to eight magnetite grains in crosses or octahedra, also in sample KUA24. **J.** Another common dendrite morphology is as paired, closely-spaced, linear "bead-chains" of sub-μm magnetite grains, shown here in another area of sample KUA24 as both an electron and optical image. The "cruciform" and "bead-chain" dendrite morphologies likely formed by encrusting growth of magnetite crystals upon pre-existing octahedral or rectilinear titanomagnetite dendrites, the recrystallized remnants of which are locally preserved as the "ladder" dendrites. Abbreviations used – XPL: cross-polarized light, PPL: plane-polarized light, BSE: backscattered electron image, Mt: magnetite, Cal: calcite, Cpx: clinopyroxene, Alb: albite, Chl: chlorite, Ttn: titanite, Ilm: ilmenite, Act: actinolite.

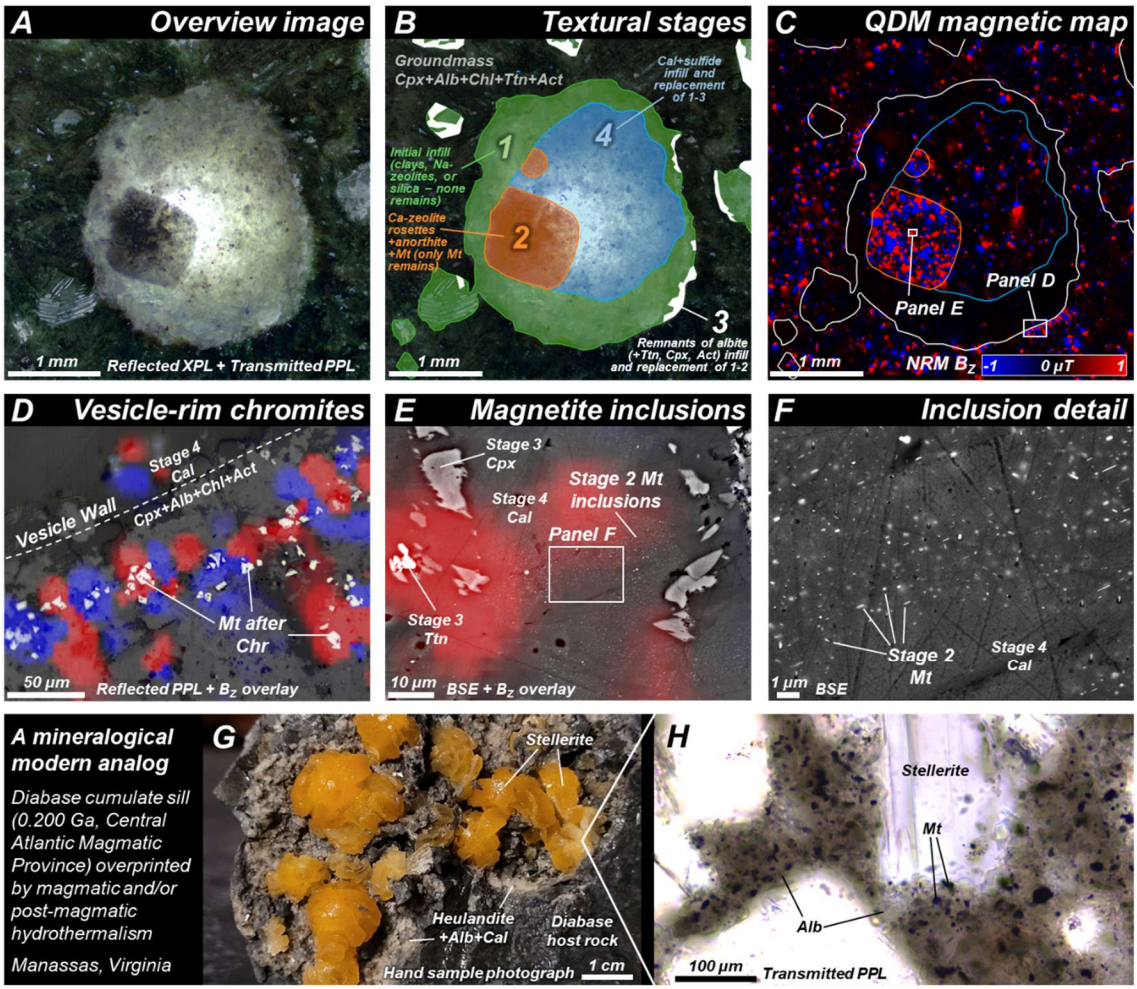

Figure S9. Magnetic mineralogy associated with vesicle infill and alteration. (See Appendix S4.3). Panels A-C all show the same field of view of a large vesicle on sample KUB2. **A** is an optical image, **B** delineates the multi-stage infill mineralogy of the vesicle, much as in (86, 87), and **C** is a QDM map of the unmodified vertical magnetic field (NRM B_Z) over the sample surface. Note the strongly-magnetized material corresponding to Stage 2 of infill, as well as more dispersed magnetized particles associated with the groundmass (magnetite) and with Stage 4 (sulfides). **D.** Detail of the rim of the vesicle in Panels A-C, showing magnetized chromite grains that nucleated on the vesicle wall during eruption, now pseudomorphed by magnetite. **E.** Detail of Stage 2 infill material showing concentrations of sub-μm magnetite inclusions that carry the magnetization, with closer detail in **F** that shows the rodlike morphology of the inclusions and their tendency to orient along a few preferred directions. This is indicative of magnetite formed by exsolution from Fe-bearing plagioclase, which precipitated along with Ca-zeolites. **G-H** show a modern analog for this infill sequence, especially Stage 2, from a diabase sill in Virginia, USA. Hand samples of cavities from this modern analog sill (**G**) contain rosettes of the Ca-rich zeolite stellerite, similar in habit to Stage 2 material. Plagioclase with titanomagnetite inclusions fills the spaces between the stellerite crystals in these rosettes (**H**), representing an analog for the mineralogy of Stage 2. Abbreviations used – XPL: cross-polarized light, PPL: plane-polarized light, BSE: backscattered electron image, Mt: magnetite, Cal: calcite, Chr: chromite, Cpx: clinopyroxene, Alb: albite, Chl: chlorite, Ttn: titanite, Act: actinolite, Plag: plagioclase.

Since Stage 2 material is almost entirely overprinted by later stages, our inference of the original phase assemblage is from similar infills that occur in modern hydrothermally-altered rocks of comparable composition. We document an identical infill assemblage from cavities in the Gainesville East Sheet, a ~0.200 Ga layered diabase sill intruding the Culpeper Basin of Virginia, USA (28-30). Alteration of this sill and those nearby by magmatic and/or post-magmatic hydrothermal fluids resulted in a variety of hydrous alteration mineralogies (29, 88). These include prehnite, hydroxyapophyllite, and a variety of Ca-rich zeolites that incompletely fill large vugs and vesicles, specimens of which are often prized by mineral collectors (31). A particularly well-known example are bright orange cm-scale rosettes of the Ca-rich zeolite stellerite (Fig. S9G). These occur on the walls of large cavities alongside coatings of sub-mm heulandite, plagioclase, and calcite (Fig. S9G). Inside the rosettes, albite with abundant titanomagnetite inclusions fills the interstices between stellerite crystals (Fig. S9H). These rosettes therefore represent a modern analog for the morphology and mineralogy of Stage 2 material, in which magnetite inclusions also occur in former plagioclase that fills spaces between crystals that nucleated as rounded aggregates on void space walls.

Following Stage 2, “Stage 3” consists of pure albite that infills the remainder of all vesicles and most veins, which fully replaced all material from Stages 1 and 2 except magnetite inclusions of Stage 2. This albite continues uninterrupted into the groundmass surrounding vesicles, filling most of the interstitial space between pyroxene phenocrysts, and thus is also a replacement of basaltic glass. Albite forms during albitization (also termed “spilitization”) of ocean floor basalts during high-water/rock-ratio hydrothermal circulation of Na^+ bearing seawater (89, 90). This Na^+ replaces the Ca^{2+} and other trace constituents in plagioclase, thus also redistributing these elements into the fluids and into new accessory minerals. Three such accessory Ca-bearing phases are closely associated as inclusions within the albite in our samples: actinolite, pure diopside, and titanite. This actinolite is abundant (89) and also forms “haloes” of alteration surrounding vesicles, where it replaces pyroxene phenocrysts. Accessory diopsides likely formed at ~320°C (91). Finally, titanites formed via liberation of Ti from primary plagioclase and/or glass (90). Returning to the younger diabase sill discussed above as a modern analog, alteration similar to Stage 3 albitization was likely responsible for converting intermediate plagioclase or anorthite infill between zeolites to pure albite. We also observe actinolite and rare titanite occurring within this albite. Others have also documented actinolite inclusions within vesicle infills from the same suite of diabase sills (29).

The final “Stage 4” infill phase assemblage is composed of calcite and occasional siderite with accessory Cu/Fe/Zn/Pb-sulfides (Figs. S7J and S12A). This calcite almost completely dissolved and replaced Stage 3 albite within vesicles and veins, and also to a lesser extent within the surrounding groundmass (Fig. S9, A-C; Fig. S12A). Multiphase fluid inclusions are common within Stage 4 carbonate, and some host reduced carbonaceous matter (Fig. S7K). This likely originated from reduced carbon produced in serpentinization reactions, or from microbial colonization of the lavas once cooled on the seafloor, followed by kerogenation of the resulting carbon during alteration, as has been observed in contemporaneous deposits nearby (92). Raman spectra of this material display characteristic disordered and graphitic (“D” and “G”) emission bands (Fig. S7L), the morphology of which may be leveraged as an alteration geothermometer (27, 93). A suite of carbonaceous inclusions in sample KUB1 yielded peak alteration temperatures of 306±19°C, indicative of <330°C lowest greenschist facies thermal conditions (see above Appendix S1, “*Extended Materials and Methods*”). Once again comparing to the diabase sill discussed above as a modern analog, calcite and sulfides are a common infill phase assemblage, occurring as an overprinting coating in large cavities (Fig. S9G) and completely filling smaller vesicles (29).

The observed replacement relationships (e.g. calcite after albite after zeolites and initial weathering products) within multistage porosity-filling minerals define a prograde paragenetic alteration sequence (Fig. S12A) that documents seawater hydrothermal alteration at progressively increasing fluid temperatures (<150°C, ~250°C, ~320°C, and ≤330°C for Stages 1, 2, 3, and 4, respectively). This intensification of hydrothermal alteration was paralleled by increasing fluid/rock ratios and more open-system character of the hydrothermal circulation. Initial alteration during relatively weak hydrothermal circulation (Stages 1 and 2) redistributed mobile elements ($K^+/Na^+/Ca^{2+}/Fe^{2+}$) into new minerals (clays, zeolites, plagioclase) without attendant

major changes in bulk composition. Exchange of Fe during this early alteration also resulted in its oxidation by the fluids and subsequent reprecipitation as magnetite, thus contributing to the H component. Later, hotter circulation of greater volumes of brine-laden seawater resulted in bulk element exchange between the seawater and rock (e.g., Na^{+}/Ca^{2+} exchange during Stage 3, and $Ca^{2+}/Mg^{2+}/Fe^{2,3+}/S^{2-}/CO_3^{2-}$ exchange during Stage 4). Other alteration processes documented herein (Fig. S12) document bulk leaching of Fe during this hydrothermal intensification, thus *removing* magnetite that hosts the H component. The carbonate precipitation of Stage 4 is especially characteristic of active subseafloor hydrothermal systems up to depths of ~1.5 km (78, 94), since the source of this hydrothermal carbonate is seawater that remains restricted to relatively shallow sub-seafloor environments with high water-rock interaction ratios (95-97).

S4.4. Magnetic imaging and identification of remanence carriers. Optical microscopy presented above reveals that Fe-bearing phases in Kunagunarrina Fm. lavas occur in diverse textural associations with secondary phases, including recrystallized groundmass dendrites, chromites, glass, mafic phases such as pyroxene, and void spaces with multistage infills. QDM mapping of samples throughout our sites show that magnetization is most commonly associated with recrystallized magnetite in the groundmass, including magnetite after primary titanomagnetites, chromites, glass, and ultramafic minerals (Figs. S8-S12) (98). QDM maps of samples from site KUA4, with the best-preserved H component magnetizations among our samples, show that the dominant magnetized phases are abundant dendritic networks of magnetite grains recrystallized from primary titanomagnetites [Fig. S8; (81)]. Populations of diversely oriented magnetite dendrites, while individually magnetically anisotropic, are excellent paleofield recorders since they exhibit SD-PSD behavior, even at PSD-MD grain sizes (82). These grains are 0.02-5 μm, and thus are expected to exhibit a mix of SD, single-vortex [SV, a PSD state between ~0.07 and ~1 μm; see Nagy et al., (99)], and MD states. Both SD and SV states are capable of preserving remanences for many Gyr, consistent with the preservation of the H component and three overprinting events over several Gyr in our samples (100).

QDM maps also show that in vesicle infill minerals, Stage 1 material is associated with little to no magnetization (Fig. S9C), while the Stage 2 aggregates of 0.03-0.7 μm magnetite grains that cloud and darken later calcite (Fig. S9, A and B) host very strong local magnetizations, greatly exceeding that of the matrix hosting the vesicles (Fig. S9C). The paragenetic sequence resulting in these magnetites indicate that their strong magnetizations were acquired as a ~250°C TCRM during hydrothermal alteration of the host lavas. Much as with magnetite dendrites, this type of exsolved magnetite is strongly magnetically anisotropic within any given plagioclase crystal, but within a population of plagioclase crystals is capable of stably retaining a directionally-accurate TCRM associated with exsolution (101). Further, the size range of the inclusions observed herein includes SD and SV states that are magnetically stable over Gyr, and possibly some MD grains as well (99, 100). Stage 4 material hosts a weak magnetization associated with its sulfides (Fig. S9, A-C).

Because only a subset of the imaged ferromagnetic grain populations may be carrying H components, we conducted an abbreviated thermal demagnetization sequence including QDM imaging at each heat step on a sample (KUB2) that carries a well-defined H component (KUB2, see Main Text Fig. 2C). This analysis, which follows Volk et al. (26) and is designed to quantify the unblock temperature spectra of observed grain populations, can test the specific association between the H component and ferromagnetic minerals produced during early hydrothermal alteration (Fig. S10). Changes in the surface microscale magnetic field pattern of a vesicle hosting Stage 2 magnetite show that about half of the vesicle's remanence unblocks up to 330°C, most likely due to sulfides (T_C ~325°C) and/or coarse magnetite grains that are common in vesicle infills. The remaining half of remanence is most likely hosted by 0.03-0.7 μm rod-shaped magnetite inclusions, and unblocks in the narrow range 520-560°C. This corresponds to the unblocking range of the H component of the bulk sample (Main Text Fig. 2C), directly tying a portion of the H component to magnetic mineralogy dating to Stage 2.

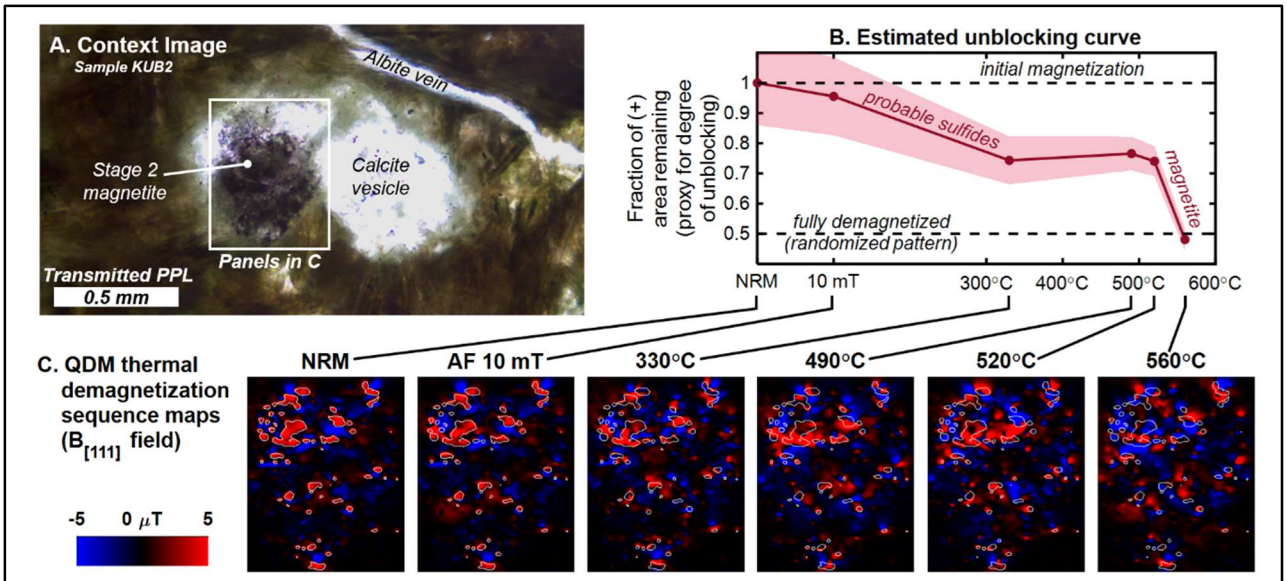

Figure S10. QDM-derived unblocking temperature estimation for Stage 2 vesicle-hosted fine magnetite in sample KUB2. A. Context optical image of a vesicle hosting Stage 2 magnetite that clouds later calcite infill. The outlined region refers to QDM magnetic field maps in panel **C**. These maps show the evolution of the surface field pattern (measured along the [111] crystallographic axis of the sensing diamond) during an abbreviated thermal demagnetization sequence from NRM to 560°C. Note that patches where the NRM surface field was positive are outlined in white on all maps, highlighting how the field pattern changes as the remanence unblocks. Calculating the proportion of pixels that remain positive in these patches over the demagnetization sequence results in the red curve in **B**, with the error envelope derived from bootstrapping the alignment errors between the NRM map and each field map. The fraction of remaining positive area is a proxy for the degree of remanence unblocking: a fraction of 1 reflects no change in the magnetization pattern and thus no unblocking, while a fraction of 0.5 reflects no statistical dependence of the field map on the NRM map (i.e., a randomized field pattern) and thus fully-unblocked remanence. From this relationship, about half of this vesicle's remanence unblocks up to 330°C, most likely due to sulfides and/or coarse magnetite grains that are common in vesicle infills. The remaining half of remanence is hosted by the μm- to sub-μm rod-shaped magnetite inclusions, and unblocks in the narrow temperature range of 520-560°C that corresponds to H component unblocking of the bulk sample (Main Text Fig. 2C). This links the H component to minerals formed via early hydrothermal alteration of the Kunagunarrina Formation.

S4.5. Titanite petrochronology constraints. Of the alteration-related phases present in our samples, titanite is especially useful since it incorporates U during crystallization and is relatively resilient to remobilization of U and Pb during low-grade metamorphism, making it suitable for U-Pb petrochronology. This offers an opportunity to directly date the alteration responsible for the ferromagnetic minerals in our samples, and thus the H component magnetization.

Titanites grown in void spaces during Stage 3 albitization represent the most appealing targets for this dating. These titanites are common in vesicle-rich samples from site KUB1 and are suitable for *in-situ* LA-ICP-MS U-Pb dating, since they can be large (100+ μm), are inclusion-free in many examples, and retain primary crystallization textures such as euhedral habits and zonation (Fig. S11, A-D). This is unlike the titanite population that formed as a replacement of ilmenite after titanomagnetite, which is ubiquitously intergrown at sub-10 μm scale with Ti oxide phases (forming the white, opaque phase assemblage "leucoxene") that may contaminate analyses (Fig. S7C).

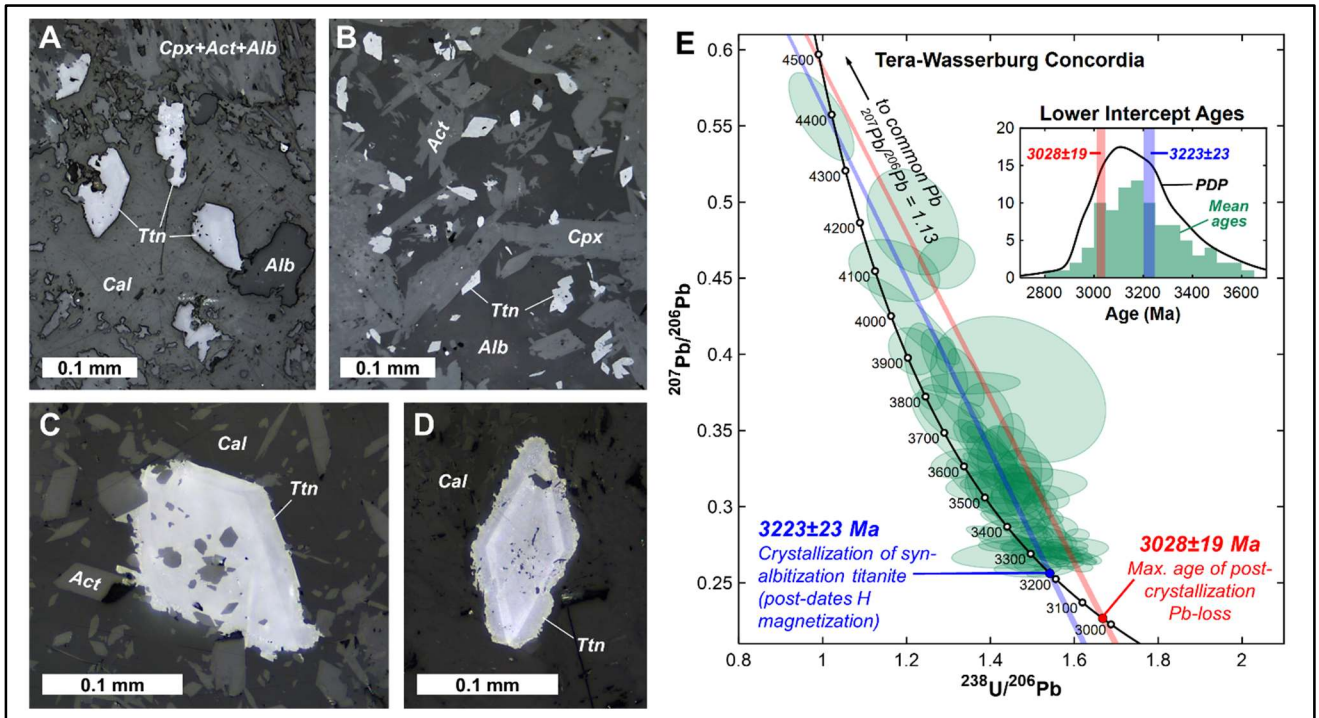

Figure S11. U-Pb dating of post-H-component titanites in Stage 3 infill. A-D show reflected plane-polarized light images of Stage 3 titanites with representative textures, including euhedral habit (all images), zonation (**C, D**), and association with cogenetic albite (**A, B**) and actinolite (**B, C**). Later calcite overprints the albite (**A, C, D**). **E.** Tera-Wasserburg Concordia diagram with our U-Pb analyses of these titanites (green; see Table S2). We deconvolved the distribution of lower-intercept ages derived from these analyses (inset; green histogram and black probability density plot or PDP) to separate pristine analyses (blue) from those disturbed by Pb-loss (red). This yielded two age groups, one reflecting Pb-loss at <3.028±0.019 Ga and another reflecting crystallization of the titanites at 3.223±0.023 Ga. The H component thus pre-dates ~3.22 Ga. Abbreviations used – Ttn: titanite, Alb: albite, Cal: calcite, Cpx: clinopyroxene, Act: actinolite.

More importantly, the timing of Stage 3 titanite crystallization confidently post-dates the growth of magnetite that hosts the H component. These titanites are closely associated with Stage 3 albite infill and replacements, and, when not directly enclosed by albite, they often contain relict embayments of albite or inclusions of Stage 3 actinolite (Fig. S11 A-C). This association is in line with the chemistry of albitization reactions, which liberate Ca and Ti from pre-existing anorthite and glass, thus making these elements available for titanite precipitation (89, 90). Finally, our trace element analyses of these titanites support a plagioclase-rich source for the titanites, since nearly all have positive Eu/Eu* anomalies (Table S2). Given the clear textural association with Stage 3 albitization, these titanites post-date Stage 2 magnetites that are directly linked to the H component by microscopic imaging of demagnetization (Fig. S10; see above Appendix S4.4, "*Magnetic imaging and identification of remanence carriers*"). In fact, several Stage 3 titanite grains overgrow the Stage 2 magnetite aggregate analyzed herein (Fig. S10). Further, these titanites and the albitization reactions that formed them post-date the reactions that grew all observed magnetite that contributes to the H component (Fig. S12). This is because the magnetites all grew during the early stages of hydrothermalism, as fluids started to mobilize Fe^{2+} from primary phases, oxidize it partially to Fe^{3+}, and re-precipitate it as magnetite (Fig. S12). Later intensification of hydrothermal circulation led to more open-system behavior, and a transition to wholesale exchange of mobile elements between rocks and fluids, including the addition of Na and Si from seawater that resulted in albitization, and remobilization of Fe into the fluids resulting in the dissolution of magnetite and late sulfide precipitation (Fig. S12).

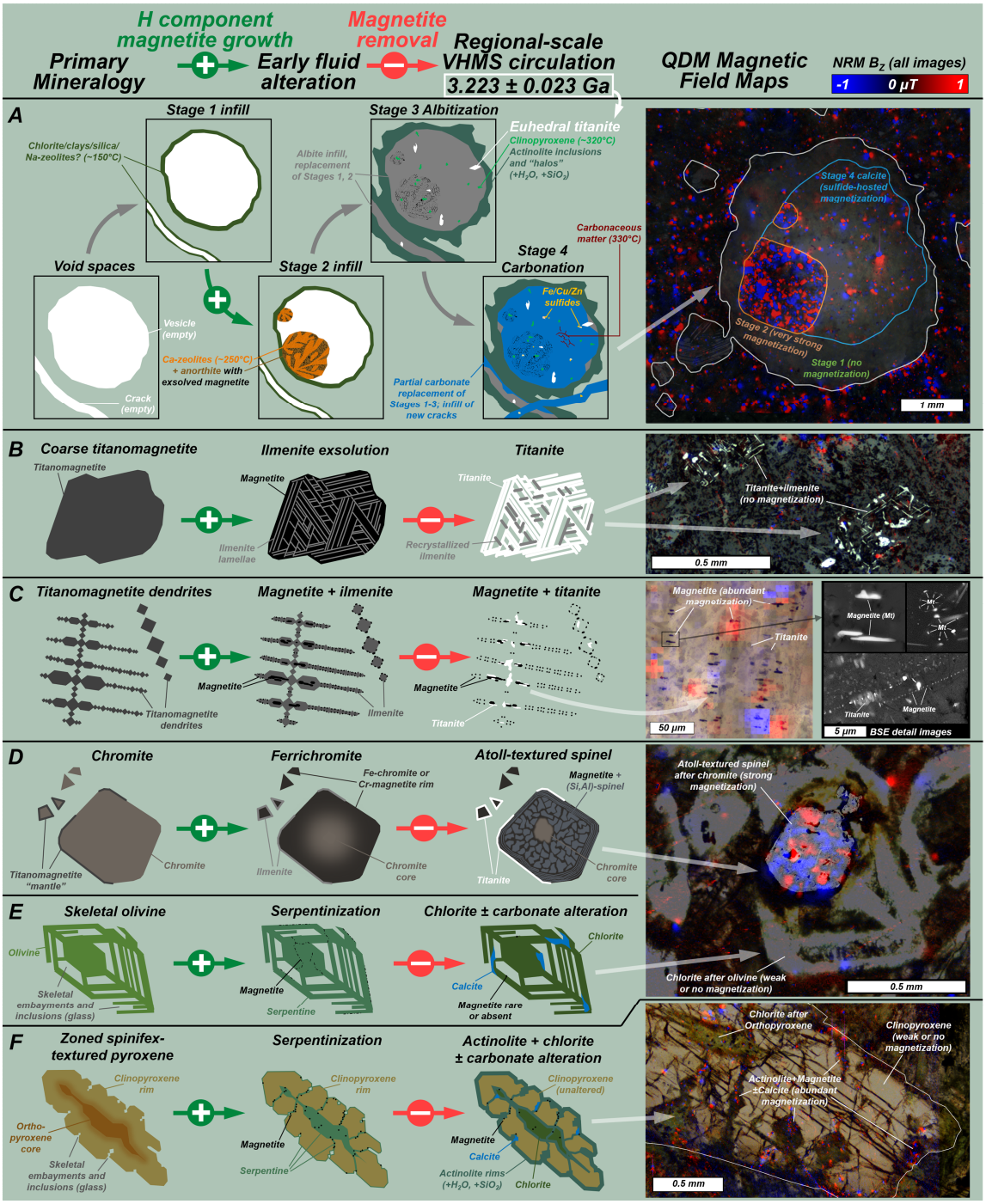

Figure S12. Summary of observed mineralogy and the resulting textures of ferromagnetic and other Fe-bearing minerals in our paleomagnetic samples. All resulting mineral assemblages were formed during seafloor hydrothermal alteration and are described in more detail throughout Appendix S4. The panels show the preserved prograde paragenetic sequence of alteration from left to right, progressing from the primary magmatic mineralogy through early fluid alteration products to those after regional lower-greenschist facies hydrothermal circulation. The resulting signatures in micromagnetic maps are shown in the right-most column. Reactions that formed magnetite hosting the resulting H component TCRM are marked with green arrows with "+" and occurred early in the alteration sequence during initial Fe^{2+} mobilization and oxidation. Later alteration within the intensifying hydrothermal system, dated herein to

3.223±0.023 Ga, resulted in leaching of Fe and H component magnetite removal, shown as red arrows with "–". In order, the strongest and most volumetrically-important alteration magnetizations, are hosted by minerals shown in panels F, C, and A, as well as by magnetite formed from alteration of volcanic glass. **A.** Void spaces (fractures, vesicles) have complex alteration mineralogies, since whichever phases are saturated in the fluid over time precipitate in the voids. The observed textures indicate four variably-overprinted stages of infill as hydrothermal temperatures increased. In order, these were (Stage 1) mafic clays, Na-rich zeolites or silica at <150°C; (Stage 2) Ca-rich zeolites plus anorthite and associated strongly-magnetized exsolved magnetite at up to ~250°C; (Stage 3) albite plus titanite (dated to 3.223±0.023 Ga, see Appendix S4.5), actinolite and clinopyroxene at ~320°C; and (Stage 4) calcite plus sulfides and carbonaceous matter thermally matured up to 330°C. **B.** Coarse titanomagnetites first exsolve into lamellae of Ti-rich magnetite and ilmenite lamellae. The ilmenite then alters to titanite and most or all magnetite is typically dissolved during progressive Fe leaching and silicification. **C.** Finer primary titanomagnetite dendrites recrystallize into ilmenite and encrusting/lamellar grains of pure magnetite, which recrystallizes again into titanite and magnetite during further fluid modification. **D.** Primary (magnesio-)chromites, some with primary mantles of titanomagnetite, first gain a metamorphic rim of diffusive Mg/Cr depletion and Fe/Cu/Zn enrichment to form magnetite or ferrichromite, followed by development of Si-spinel and magnetite "atoll" textures in large grains during more advanced fluid alteration. **E.** Primary skeletal olivines first serpentinize into serpentine and magnetite, followed by replacement of serpentine by chlorite (pictured) or calcite and removal of most magnetite by fluid leaching. **F.** The orthopyroxene cores and fractured clinopyroxene rims of zoned acicular pyroxenes first serpentinize, yielding magnetite in significant enough quantities that it most likely dominates the bulk magnetization of most samples. Serpentine is then altered to chlorite (and some remaining clinopyroxene to actinolite) via hydration and silicification reactions, with later overprinting by carbonate precipitation. Abbreviations used – BSE: backscattered electron image, Mt: magnetite.

Having established that Stage 3 titanites are suitable dating targets and post-date the H component, we performed *in-situ* laser ablation U-Pb analyses of 120 Stage 3 titanite grains in two samples (KUB1 and 2) from site KUB1. Of these analyses, we excluded 27 with strong reverse-discordance, low Ti, or high errors (Table S2; see above Appendix S1.7, "*Geochronology*"). The remaining 93 analyses fall along a discordia line, overlapping the Tera-Wasserburg Concordia at its lower intercept between 3.3 and 3.2 Ga (Fig. S11E).

Some analyses have slightly elevated $^{238}U/^{206}Pb$ and therefore depart slightly from this discordia, resulting in dispersion of their lower-intercept ages towards younger values (Fig. S11E). We interpret this as a signature of minor post-crystallization Pb-loss in some of the population. This is in line with trace element abundance patterns, which are similar across the entire titanite population (Table S2). This suggests that all analyzed titanites crystallized during the same event, and later events have partially remobilized Pb in some grains while leaving trace elements unaffected. Many later events are candidate sources of this Pb-loss, most notably the 2.2-2.0 Ga Ophthalmian Orogeny that resulted in Pilbara-wide resetting of Pb-Pb dates (8).

This Pb-loss biases lower-intercept ages in the discordia array towards younger values, resulting in an underestimate of the crystallization age of the titanite population. To mitigate this effect, we applied a two-component Gaussian deconvolution (42) to the distribution of lower-intercept ages, thus isolating pristine analyses from those disturbed by later Pb-loss. This yielded age groups centered on 3.028±0.019 Ga and 3.223±0.023 Ga (2σ), representing 36% and 64% of the analyses, respectively (both ±15%; Fig. S11E). We interpret the former ~3.03 Ga age group as the maximum age of the apparent Pb-loss in some samples. This leaves the ~3.22 Ga age group, which we interpret as the crystallization age of the analyzed Stage 3 titanite population. This is consistent with the absence of analyses overlapping the Concordia at ages <3.2 Ga (Fig. S11E). The magnetite that hosts the H component in the Kunagunarrina Fm. is therefore older than this 3.223±0.023 Ga titanite population.

S4.6. Timing of alteration and magnetization. Textural observations throughout this Appendix ubiquitously demonstrate that magnetite in Kunagunarrina Fm. lavas formed during relatively shallow (within a few km depth) and relatively low temperature (≤330°C) hydrothermalism. Further, this magnetite preserves an H component magnetization that originated as a thermochemical remanence (TCRM) acquired between eruption of the lavas at 3.275-3.249 Ga and the precipitation of later hydrothermal phases which we directly date to 3.223±0.023 Ga. Below, we use these constraints to identify the event responsible for the H component TCRM.

Of the numerous hydrothermal and metamorphic events documented from the East Pilbara, this date range is incompatible with those that occurred after ~3.2 Ga. Most are also readily eliminated based on several lines of evidence. First, our passing fold test demonstrates that the H magnetization pre-dates the ~2.93 Ga North Pilbara Orogeny (Main Text Fig. 3; see above Appendix S3, "*Magnetization timing from paleomagnetic field tests*"). Further, abundant carbonate as the final hydrothermal precipitate in our samples is indicative of shallow zones of hydrothermal systems that experience strong interaction with seawater (95-97). This argues against TCRM acquisition during events post-dating burial of our samples to more than a few km, most notably during the 3.07 Ga Prinsep Orogeny and associated Elizabeth Hill Supersuite (Kunagunarrina Fm. burial depth >5 km). Additionally, 3.07 Ga intrusions, structures, and metamorphism are mostly limited to the East Pilbara's northwestern and southeastern margins, inconsistent with a pervasive overprint in the SVS (48).

An earlier possible overprinting event is the emplacement of the 3.18 Ga Dalton Suite, which includes voluminous sills in the SVS [Main Text Fig. 1; (102)]. However, this event would have resulted in a hydrothermal overprint carrying a similar direction to that of the comagmatic Honeyeater Basalt (5), which is not the case here. Additionally, the mineralogy of the Kunagunarrina Formation does not include the ~250-300°C prehnite-pumpellyite alteration assemblage locally preserved within the Honeyeater Basalt (5, 102), indicating that the Kunagunarrina Formation likely experienced an additional metamorphic event with higher peak temperatures before the early seafloor alteration of the Honeyeater Basalt.

The only documented event in the region that could have resulted in a TCRM with the timing, alteration style, and mineralogy of the H component is the intrusion of voluminous granitic plutons of the Cleland Supersuite, the nearest of which are between 3.257 and 3.235 Ga (48). The geological and mineralogical context of the rocks surrounding our sampling area document that these intrusions drove hydrothermal activity and metamorphism in the region. This interval is marked by widespread resetting of Ar-Ar and Rb-Sr closure ages throughout the East Pilbara (46, 103-105), as well as structural doming of composite batholiths (106). One Cleland Supersuite multiphase intrusion was responsible for intense hydrothermal mineralization at 3.244-3.235 Ga centered ~30 km to the north of the study area (47, 50-53). The exhalite horizon associated with this hydrothermal event is the regional seafloor exhalite "Marker Chert" that hosts base metal sulfides in a variety of volcanic-hosted massive sulfide (VHMS) deposits formed during seafloor hydrothermal activity (47, 50-53). The Marker Chert outcrops in the SVS within 1 km upsection of our sampling sites, where it is underlain by veins of colloform quartz that further indicate its hydrothermal origin [Main Text Fig. 1, Fig. S1A-B; (107)]. Galena from this horizon and similar underlying mineralization, including in the SVS, yields direct Pb-Pb ages between $3.257^{+0.008}_{-0.006}$ and 3.235 Ga, with some samples overprinted by partial (~3.22 Ga) or full (~3.07 Ga) Pb-Pb resetting (54, 108). This hydrothermal circulation event therefore shares the style and timing of alteration observed in our samples.

Additionally, the presence of diverse Fe/Cu/Zn sulfides in our own samples (Fig. S7J) associated with late hydrothermal textures suggests that this regionally-developed hydrothermal circulation was responsible for the late stages of their alteration (94, 109). Our study area also shows a common characteristic of VHMS-style alteration in the form of locally-patchy, approximately bedding-parallel ("semiconformable") alteration within competent rock packages (e.g., thick stacks of lavas, as in our sampled flows) but nearly uniform strong alteration in more permeable units (e.g., loose sediments, as in the central lapillistone horizon at locality KUT), further suggesting that hydrothermal circulation produced the assemblages we identify in our samples (94, 109, 110). This style of alteration occurs in episodes linked to heating by the individual intrusions that drive the circulation of seawater in the system (54, 110). This circulation is convective in geometry and therefore remagnetizes rocks over a broad range of depths all at

once, as distinct from burial alteration, which operates more like a “conveyor belt,” continuous in time and with a strong dependence on depth and local geotherm. Fluid circulation episodes have durations comparable to the cooling timescale of the intrusions that drive them, driving mineral alteration for up to thousands to hundreds of thousands of years (70, 71). This is long enough that data from a suite of geographically-separated sites that were altered (and thus magnetized) at different times by the same protracted VHMS circulation event can be averaged together to sample paleosecular variation (PSV) and record the time-averaged field during alteration.

The fluid circulation responsible for forming the H component TCRM was therefore expressed as episodic percolation of hydrothermally-warmed seawater through the recently-buried volcanic pile. This circulation altered the rock package, with early stages of alteration producing the TCRM (Fig. S12). As evidenced by the reversal in our section, at least two discrete hydrothermal flow events occurred during eruption of the sampled package, either regional or local in scale, driven by intrusions and/or progressive early burial of the package.

Intriguingly, two stratigraphic horizons within our sampled section are associated with VHMS-style hydrothermal circulation, each of which could be responsible for one of the observed magnetization polarities. This interpretation is appealing in that it readily explains both the hydrothermal origin of the magnetic mineralogy and the presence of a reversal within the section (see above Appendix S3, “*Magnetization timing from paleomagnetic field tests*”). One such horizon is the mafic submarine volcaniclastic unit in the center of the sampled package (Main Text Fig. 1C; Fig. S1, E-G). This horizon contains abundant pods and veins of massive hydrothermal quartz, indicating pronounced fluid circulation shortly following its eruption (Main Text Fig. 1C). Also, submarine pyroclastic lithofacies are commonly associated with local VHMS mineralization (94-97, 109-112). This horizon occurs above the sites that host the “reversed” polarity H component, and below all other sites, and thus could be responsible for magnetization of the lower Kunagunarrina Fm. The other mappable syn-alteration horizon in the area is the regional Marker Chert discussed above, which was deposited at 3.238±0.003 Ga during regionally-developed circulation surrounding the Strelley Granite to the north (47). This horizon, which is the last mappable evidence for semiconformable hydrothermal circulation in the area, is likely responsible for the magnetization of sites hosting the “normal” polarity H component in our study, and thus the upper part of the Kunagunarrina Formation.

Also intriguing is the preservation of the reversed polarity H component through later hydrothermal alteration that resulted in the normal polarity, with apparently no samples that record a mix of both polarities or that record the normal polarity as an overprint of the reversed polarity. One explanation is that the normal polarity direction is somewhat similar to the regional “M” component overprint in *in situ* coordinates, so some normal polarity overprints may be misclassified as part of the M component and remain unrecognized. Alternatively, several mechanisms could explain why the lower, reversed polarity sites may be resilient to further remagnetization during alteration that produced the normal polarity. First, as we document at length above, hydrothermal alteration resulted in infilling of porosity and compositional changes that decreased the permeability of affected rocks (especially silicification). Consequently, the alteration process progressively restricted the flow of hydrothermal fluids, thus “armoring” rocks against further alteration events. Second, we show that the H component was acquired during the initial stages of fluid alteration of our samples, while later, more intense hydrothermal circulation actually resulted in the partial destruction of this magnetization through leaching of Fe-bearing phases such as magnetite (Fig. S12). Any normal overprints on reversely-magnetized samples were therefore likely removed via dissolution of its carrier phases.

In summary, the mineralogical context and alteration textures in our samples document that the H component magnetization arose during thermochemical alteration of our samples by circulating hydrothermal fluids just below the paleoseafloor. Dating of alteration phases also narrowly constrains the timing of this magnetization, which together with other geochronology and field evidence, identifies the event responsible for the magnetization as sub-seafloor hydrothermal circulation associated with nearby intrusions of the 3.257-3.235 Ga Cleland Supersuite (48). The minimum feasible age of the H component magnetization is 3.235 Ga, which is the minimum allowable age bound on the 3.238±0.003 Ga Marker Chert horizon, the last hydrothermal horizon in the study area [SHRIMP U-Pb date on zircon (47)]. Likewise, the maximum age we consider for the H component is 3.265 Ga, the maximum allowable age bound

on the oldest mineralization documented from Cleland Supersuite magmatism at $3.257^{+0.008}_{-0.006}$ Ga [Pb-Pb model age of galena in a VHMS deposit (54, 108)].

S4.7. General implications for Archean paleomagnetism. Magnetization via shallow hydrothermal alteration readily explains many Archean magnetizations of seafloor-deposited units [e.g., (5, 6)], especially since most Archean remanences thus far reported are consistent with pure magnetite as the host mineralogy. Dating of modern seafloor hydrothermal deposits shows that mineral growth from local pulses of circulation, when driven by large intrusions, can be sustained for up to thousands to hundreds of thousands of years (70, 71, 113), long enough to fully sample PSV. Also, remanences measured from most Archean lavas are substantially weaker than those from their unaltered modern equivalents, since hydrothermal modifications to magnetic mineralogy mainly result in removal of magnetic phases by leaching of Fe, weakening magnetizations or destroying them entirely. This effect is strongly dependent on the fluid permeability of the altered rocks, likely explaining why our conglomerate test at KUT was indeterminate due to a lack of coherent H components, since it sampled from a permeable volcaniclastic horizon that experienced advanced hydrothermal alteration and removal of magnetization.

This style of magnetization also potentially explains anomalously low reversal frequencies documented in younger Archean rocks (43), since reversals may have been preserved as primary thermoremanences at first, but later were fully overprinted by sporadic alteration events that simultaneously remagnetized a large range of stratigraphic heights, resulting in thick packages of uniformly-magnetized rocks. Further, the lack of primary mineralogy, despite the passing reversal test, calls into question some Archean paleointensity studies that do not carefully show that they measure signals from phases carrying primary thermoremanent magnetizations. Future Archean paleointensity work must carefully rule out secondary remanences acquired during hydrothermal alteration shortly after emplacement.

Overall, the mineralogical changes described above highlight the importance of detailed microscopic examination of magnetic carriers and their textural associations. Despite the many potential pitfalls of working with this type of magnetization, our results demonstrate that in pervasively altered rocks, paleomagnetic analyses can still be successful where the magnetic mineralogy can be robustly linked to precisely-dated alteration episode(s). The complex alteration histories of cratonic blocks can permit robust paleomagnetic work in deep geologic time, at least for rocks in which primary remanences are not preserved.

Appendix S5: Stagnant-lid net rotation speed limits

Before attributing measured Archean surface motions to tectonic processes, we must first consider whether motion of a stagnant-lid can account for them. All motions of a stagnant-lid must manifest as global rotations of the entire lithosphere, which result from two physical processes. The first is True Polar Wander (TPW), in which the lithosphere-mantle system rigidly rotates to align Earth's maximum moment of inertia axis to Earth's rotational axis. While TPW is capable of plate-tectonics-like speeds, it can only occur along an axis that intersects Earth's rotational equator and is likely limited to rotations of ~90° for a single stage event [see Main Text; (114)]. The second is net rotation, in which lateral variability in sub-lithospheric viscosity structure results in global asymmetry of coupling to mantle flow (115-117). Below, we derive a scaling for the characteristic speed of fast net rotation (in simplified terms, a "speed limit") in a stagnant-lid setting, based mainly on Ricard et al. (115) and Rudolph et al. (116). Table S3 lists all parameters used in this derivation. See also Fig. S13.

S5.1. Net rotation derivation. Consider a stagnant lid sitting atop the convecting upper mantle. Coupling them is a shear zone, corresponding to the upper asthenosphere (Fig. S13B), with thickness h that varies globally such that it has constant vertically-averaged viscosity η. Both the lid and mantle are mobile, with vector difference in velocity $\Delta\boldsymbol{v}$. This relative velocity is equivalent to the strain rate $\dot{\boldsymbol{\varepsilon}}$ accumulating over the thickness h of the coupling zone that accommodates all relative motion (Fig. S13B). Since $\dot{\boldsymbol{\varepsilon}}$ is also shear stress $\boldsymbol{\sigma}$ divided by viscosity η,

$$\dot{\boldsymbol{\varepsilon}} = \frac{\Delta\boldsymbol{v}}{h} = \frac{\boldsymbol{\sigma}}{\eta} \tag{9}$$

Since all forces are horizontal, this basal traction applied across the zone of deformation can be reframed as a basal torque $\boldsymbol{\tau}$ about Earth's center a distance $\boldsymbol{r}$ away:

$$\boldsymbol{\tau} = \boldsymbol{r} \times \boldsymbol{\sigma} = \frac{\eta}{h}\boldsymbol{r} \times \Delta\boldsymbol{v} \tag{10}$$

We are interested in the no-acceleration case in which the horizontal stresses acting on the lithosphere balance to give a steady-state velocity. These forces can include substantial contributions from plate boundaries (e.g., ridge push, slab pull), but these are absent in a one-plate stagnant-lid, so the only force to consider is basal traction. The integrated basal torque on the lithosphere must be zero so that the lithosphere does not accelerate indefinitely:

$$\int_A \boldsymbol{\tau}\, dA = \eta \int_A \frac{\boldsymbol{r} \times \Delta\boldsymbol{v}}{h}\, dA = \eta \int_A \frac{\boldsymbol{r} \times (\boldsymbol{v_L} - \boldsymbol{v_M})}{h}\, dA = 0 \tag{11}$$

In words, all incremental areas dA of the lithosphere experience a basal traction force due to viscous deformation within a layer of thickness h and average viscosity η, induced by (and proportional to) lithospheric motion ($\boldsymbol{v_L}$) relative to local underlying mantle motion ($\boldsymbol{v_M}$).

Solving for the $\Delta\boldsymbol{v} = \boldsymbol{v_L} - \boldsymbol{v_M}$ field explicitly is impossible for the Archean without the 3D structure and motions of the upper mantle and lithosphere. A simplifying assumption is that the Archean lithosphere was bimodal much like today's, with an area A_C of thick, "continent-like" cratons (subscripts "C") set in a larger area A_O of thinner "oceanic" lithosphere (subscripts "O") (Fig. S13, A and B). The coupling zones below each type of lithosphere have distinct thicknesses h, separating their equal but opposite contributions to global basal traction:

$$\frac{1}{h_C}\int_{A_C} \boldsymbol{r} \times (\boldsymbol{v_L} - \boldsymbol{v_M})_{\boldsymbol{C}}\, dA_C = -\frac{1}{h_O}\int_{A_O} \boldsymbol{r} \times (\boldsymbol{v_L} - \boldsymbol{v_M})_{\boldsymbol{O}}\, dA_O \tag{12}$$

The importance of this lithospheric dichotomy for net rotation is that it introduces a nonuniform upper boundary condition for mantle convection, whereas convection within a uniform medium with uniform boundary conditions cannot produce net rotation (118). Separating terms,

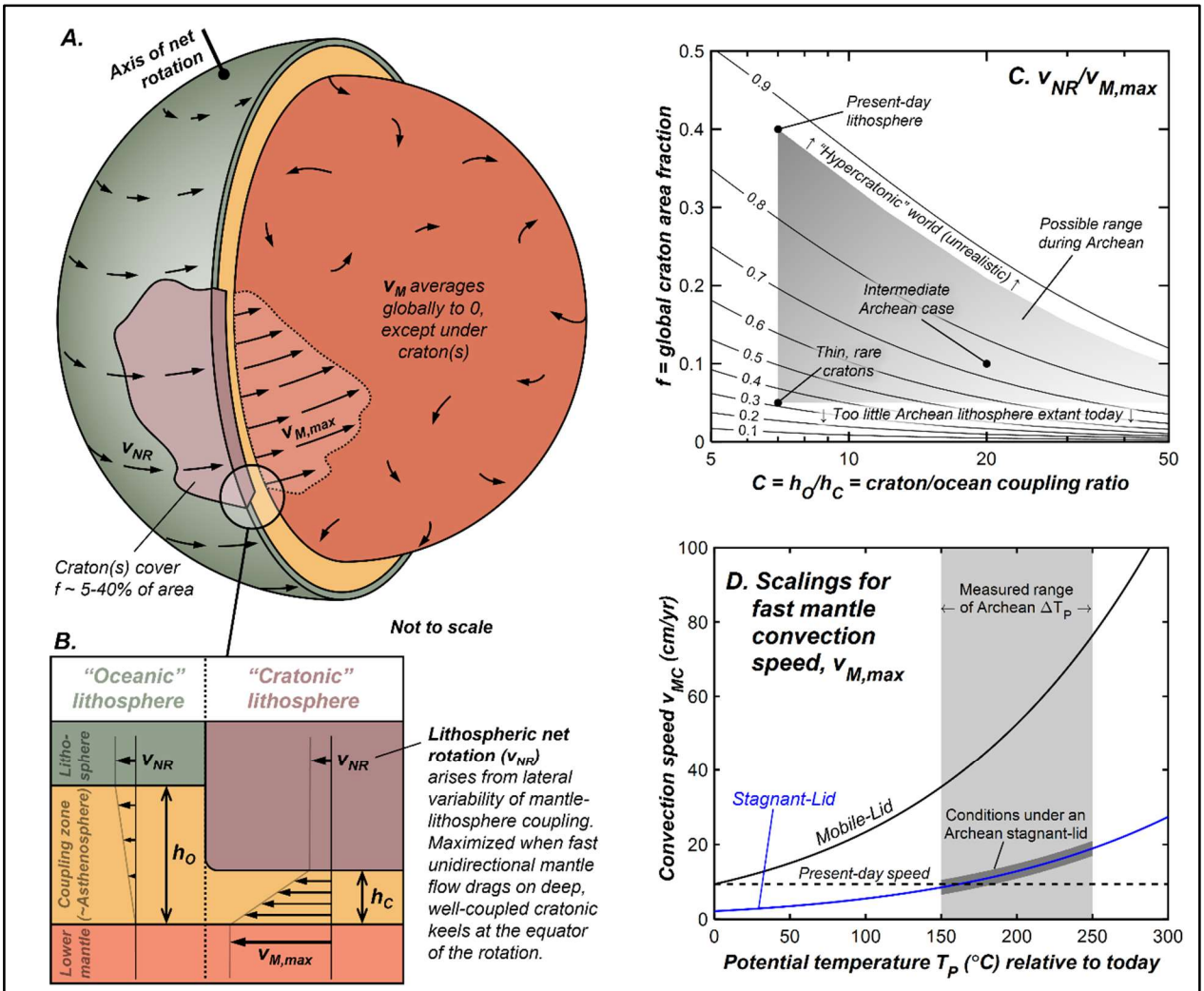

Figure S13. Framework for deriving the speed limit of lithospheric net rotation on a stagnant-lid. Schematics of the global velocity structure (**A**) and kinematic setup (**B**) in this framework illustrate that fast perturbations to mantle flow (speed $v_{M,max}$) can excite a rigid-body net rotation (speed v_{NR}) of a one-plate bimodal lithosphere (cratons in brown, oceans in green) coupled heterogeneously through the uppermost mantle (yellow) to motions of the mantle (orange). In the case of maximum net rotation, the lithosphere that couples best to mantle flow (cratons) is concentrated on the equator of the rotation, and overlies fast unidirectional mantle flow. **C.** The scaling factor between v_{NR} and $v_{M,max}$ in this scenario depends on the fraction f of global area covered by cratons and the ratio C of coupling efficiency between the cratons and oceans. This factor approaches unity for high f and C, i.e. for the greatest dichotomy in lithosphere-mantle coupling. The region of possible Archean values is shaded gray. **D.** Scaling of $v_{M,max}$ under mobile-lids (black curve) and stagnant-lids (blue curve) with mantle potential temperature (expressed as its value above 1350°C today). The gray shaded region corresponds to the range of T_P predicted for the Archean based on petrologic data (119), and the dashed line indicates the convection speed under the modern mobile-lid. If Earth had a stagnant-lid in the Archean, mantle convection speed under the lid would have been comparable to or slightly faster than its modern speed, thanks to a balance between lower viscosity at higher mantle temperatures and a thicker boundary layer due to a stagnant-lid. For mobile-lids, it is worth noting that plate motion speeds are proportional to this speed scaling, but also depend on other factors, especially the strength and mechanical characteristics of the lithosphere.

$$\frac{1}{h_C}\left[\int_{A_C} \boldsymbol{r} \times \boldsymbol{v_L}\, dA_C - \int_{A_C} \boldsymbol{r} \times \boldsymbol{v_M}\, dA_C\right] = -\frac{1}{h_O}\left[\int_{A_O} \boldsymbol{r} \times \boldsymbol{v_L}\, dA_O - \int_{A_O} \boldsymbol{r} \times \boldsymbol{v_M}\, dA_O\right] \quad (13)$$

We now consider the velocity fields of each term. Since a stagnant-lid is rigidly connected, the velocity field $\boldsymbol{v_L}$ is that of a rotating spherical shell (Fig. S13A) as a function of polar angle θ from the rotation axis and maximum surface speed at the rotational equator v_{NR}:

$$|\boldsymbol{v_L}| = v_{NR} \sin(\theta) \quad (14)$$

As we are interested in the maximum possible rate of net rotation, we consider the case where all cratonic lithosphere is concentrated along the equator of the net rotation axis, the simplest and most geologically-reasonable context of which would be as a supercraton (Fig. S13A). This maximizes the contribution of the craton(s) to basal traction. In the approximation of relatively small and equatorially-placed craton(s), $|\boldsymbol{v_L}|$ within A_C is $\sim v_{NR}$.

Fast net rotation also requires that mantle flow below all cratonic lithosphere is as fast as possible and unidirectional, inducing strong basal drag on the cratonic keel(s) uniformly in the same direction as v_{NR} (Fig. S13A). Again in the approximation of relatively small and equatorially-placed craton(s), $|\boldsymbol{v_M}|$ within A_C is therefore $\sim v_{M,max}$, the fastest possible horizontal mantle convection speed. The small-craton approximation also makes the oceanic area A_O approximately the area of Earth's surface A. Within this area $A_O \approx A$, the mantle convection pattern may be quite complex, but the vector average of convective speed is very close to zero (i.e., globally-averaged $|\boldsymbol{v_M}|$ within A is ~0, so $\int \boldsymbol{r} \times \boldsymbol{v_M} dA \sim 0$). This is because in the case of small cratons, the upper boundary condition for mantle convection is close to homogeneous, allowing for very little global degree-1 toroidal convective motion [i.e., mantle net rotation; (118)]. Also, the average upper mantle flow under oceanic lithosphere, if non-zero, is expected to oppose the flow under the cratons, balancing the strong flow and counteracting the basal traction beneath the craton(s). Setting $|\boldsymbol{v_M}|$ within A to ~0 therefore sets an upper bound on v_{NR}.

Substituting these velocity fields into Eq. 13 and evaluating,

$$\frac{1}{h_C}\left[r v_{NR} A_C - r v_{M,max} A_C\right] = -\frac{1}{h_O}\left[r v_{NR}\left(\int_{A_O} \sin(\theta)\, dA - A_C\right)\right] \quad (15)$$

Since the spherical differential surface area element is $dA = r^2 \sin(\theta)\, d\theta d\phi$, where ϕ is longitude, the integral on the right-hand side reduces to

$$\int_{A_O} \sin(\theta)\, dA = r^2 \int_0^{2\pi} \int_0^{\pi} \sin^2(\theta)\, d\theta\, d\phi = \pi^2 r^2 \quad (16)$$

and Eq. 15 becomes

$$\frac{1}{h_C}\left[r v_{NR} A_C - r v_{M,max} A_C\right] = -\frac{1}{h_O}\left[r v_{NR}(\pi^2 r^2 - A_C)\right] \quad (17)$$

Simplifying and rearranging,

$$\frac{h_O}{h_C}\left[v_{NR} - v_{M,max}\right] = \frac{A_C - \pi^2 r^2}{A_C}\left[v_{NR}\right] \quad (18)$$

We now introduce two new variables that make this expression more convenient. The first is a "coupling factor" C, which is the coupling zone thickness ratio h_O/h_C. This factor is best understood as the imbalance between how efficiently cratons versus oceanic lithosphere couple mechanically to underlying mantle flow. The second is the fraction f of global area occupied by cratonic or "continent-like" lithosphere. Normalizing A_C and $\pi^2 r^2$ by Earth's surface area $4\pi r^2$ thus allows for the substitution $f = A_C/4\pi r^2$. In terms of C and f,

$$v_{NR} \leq \left[\frac{C}{C + \frac{\pi}{4f} - 1}\right] v_{M,max} \quad (19)$$

Qualitatively, the stagnant-lid lithospheric net rotation speed limit scales as the maximum attainable horizontal speed of mantle convection $v_{M,max}$ under the lithosphere best coupled to mantle flow (Fig. S13C). The scaling corrects for the counteracting drag force due to basal traction under the remaining lithosphere. Fast net rotation is promoted by large $v_{M,max}$ (fast driving speed), large f (extensive mantle-coupled keels), and large C (deep keels) (Fig. S13C).

What values of the continental fraction f and craton-ocean coupling ratio C are reasonable for the Paleoarchean? Secular growth of the continental crust around cratonic nuclei strongly suggests that f was no more than its present-day value of 0.4, and a wide variety of postulated Paleoarchean values exist, some as low as ~0.05 based on the present-day distribution of crustal ages. Ricard et al. (115) estimate that the value of C is ~7 for today's lithosphere, but the value may well have larger in the Archean, since the depth of cratonic keels is greater than the depth of average modern continental lithosphere, leading to a higher coupling ratio (117). For our analysis, we consider C ~ 20 a more reasonable value for the Archean.

One caveat is that a scenario with cratonic area similar to modern continental area (f ~ 0.4) is unlikely to occur with high C, since this would imply that cratons occupied almost all of the area currently occupied by the continents. Such a "hyper-cratonic" scenario (Fig. S13C) would imply a much larger volume of continental lithosphere in the Archean than today, since the modern continents are a mix of thick-keeled cratons and substantially thinner and younger mobile belts. The majority (comprising ~1/3 of Earth's surface area) of this ancient cratonic lithosphere would then have to be recycled back into the mantle. While this is possible in principle via decratonization, such as in the North China Craton (120), cratons are thought to be preferentially preserved through geologic time, precisely because their thick keels stabilize them against tectonic modification and destruction. This "hyper-cratonic" Archean scenario is therefore highly unlikely, motivating the use of the modern lithosphere (f = 0.4, C ~ 7) as a more realistic choice for an upper bound on mantle-craton coupling in an Archean Earth with a large continental area. This would still imply that since the Archean, a large volume of continental lithosphere has been reworked into the mantle, since this Archean lithosphere is not extant today.

In the limit of thin, rare cratons (f ~ 0.05, C ~ 7), an intermediate Archean case (f ~ 0.1, C ~ 20), and the modern case (f = 1, C ~ 7), the surface net rotation speed limit scales as:

$$v_{NR} \leq 0.32 v_{M,max} \ (thin, rare\ cratons) \quad (20)$$
$$v_{NR} \leq 0.74 v_{M,max} \ (intermediate\ Archean\ case) \quad (21)$$
$$v_{NR} \leq 0.88 v_{M,max} \ (modern\ lithosphere\ structure) \quad (22)$$

Since $v_{M,max}$ is comparable to fast plate motion speeds (~9-10 cm/yr), this scaling predicts v_{NR} on the modern Earth cannot exceed ~88% of the speed of fast plate motions, or ~0.8°/Myr. Notably, this discounts TPW, plate boundary forces, and net rotation of the mantle induced by lid motions, all of which can contribute to a greater modern observable speed limit. Still, during the last 200 Myr, the maximum net rotation observed was ~0.75°/Myr, and persisted for only a few Myr (116, 121), in line with this scaling. For a broad range of reasonable Archean values for f and C, the maximum possible surface net rotation is comparable to or less than that of the present-day Earth with respect to the speed of fast mantle convection $v_{M,max}$.

S5.2. Mantle flow scaling laws. Next we examine what values of $v_{M,max}$ are reasonable for the Archean. In stagnant-lid regimes, the mantle convection speed v_{SL} scales as (122-124)

$$v_{SL} = c\left(\frac{\kappa}{d}\right)\left(\frac{a_{RH} Ra_i}{\Theta}\right)^{2/3} \quad (23)$$

where c is a scaling constant, the ratio of thermal diffusivity κ (1×10^{-6} m^2/s) to depth of the mantle d (2890 km) dimensionalizes the velocity relative to models, a_{RH} is a constant (~2), Ra_i is the mantle Rayleigh number, and Θ is the Frank-Kamenetskii parameter, defined as (125)

$$\Theta = \frac{Q\Delta T}{R(T_S + \Delta T)^2} = \frac{Q(T_P - T_S)}{RT_P^2} \quad (24)$$

where Q is creep activation energy [~300 kJ/mol for dry olivine; see below for a discussion of rheology; (126)], R is the gas constant (≡ 8.314 J/mol/K), T_S is the lid surface temperature (300 K), T_P is the potential temperature of the upper mantle (~1350°C = 1623 K today), and $\Delta T = T_P - T_S$ is the temperature difference across the mantle-lid system. Ra_i is defined as

$$Ra_i = \frac{\rho \alpha g \Delta T d^3}{\kappa \eta_i} = \frac{\rho \alpha g d^3 (T_P - T_S)}{\kappa \eta_i} \quad (25)$$

where ρ is density (4500 kg/m^3), α is thermal expansivity (3×10^{-5} K^{-1}, (127)), g is gravitational acceleration (10 m/s^2), and η_i is effective viscosity of the upper mantle. We adopt an Arrhenius law for η_i versus T_P:

$$\eta_i = \eta_0 \exp\left[-\frac{Q}{R}\left(\frac{1}{T_{P0}} - \frac{1}{T_P}\right)\right] \quad (26)$$

where η_0 is a reference mantle viscosity (10^{21} Pa·s) at,the modern mantle potential temperature T_{P0}. Substituting Eq. 24-26 into Eq. 23 and simplifying,

$$v_{SL} = cd\left(\frac{a_{RH} R \rho \alpha g (\kappa)^{1/2} T_P^2}{Q \eta_0}\right)^{2/3} \exp\left[\frac{2Q}{3R}\left(\frac{1}{T_{P0}} - \frac{1}{T_P}\right)\right] \quad (27)$$

In comparison, the scaling for the speed of convection in a mobile-lid regime v_{ML} is

$$v_{ML} = c\left(\frac{\kappa}{d}\right)(Ra_i)^{2/3} = cd\left(\frac{\rho \alpha g (T_P - T_S)(\kappa)^{1/2}}{\eta_0}\right)^{2/3} \exp\left[\frac{2Q}{3R}\left(\frac{1}{T_{P0}} - \frac{1}{T_P}\right)\right] \quad (28)$$

The fundamental distinction relative to the stagnant-lid scaling is the omission of the factor $(a_{RH}/\Theta)^{2/3}$. This factor accounts for greatly decreased participation of the cold lid in convection, resulting in a dramatic reduction in the proportion of the temperature contrast ΔT that is available to drive convection (122, 124, 125). The scaling constant c in both stagnant- and mobile-lid scalings is chosen (~0.07) to reproduce fast modern plate motion speeds (~9-10 cm/yr). The consequence is that over the allowable range of potential temperatures (up to 250 K above present-day; see below), v_{ML} exceeds v_{SL} at a given mantle temperature by a factor of

$$\frac{v_{ML}}{v_{SL}} = \left(\frac{\theta}{a_{RH}}\right)^{2/3} = \left(\frac{Q(T_P - T_S)}{2RT_P^2}\right)^{2/3} \sim 4.0 - 4.4 \quad (29)$$

The forms of Eq. 27 and 28 also make clear that in both regimes, an increase in mantle potential temperature of 200 K above the modern value also increases convective speed by a factor of

$$\frac{v_{T_{P0}+200\,K}}{v_{T_{P0}}} = \exp\left[\frac{2Q}{3R}\left(\frac{1}{T_{P0}} - \frac{1}{T_{P0} + 200\,K}\right)\right] \sim 5 - 6 \quad (30)$$

Together, Eq. 29 and 30 imply that to match or exceed modern convection velocities, an Archean stagnant-lid with otherwise similar properties would have required a mantle potential temperature ~150°C hotter than at present. Incidentally, this is in line with most petrological estimates of Archean T_P, which typically imply ΔT_P between ~150-250°C (119, 128). This range would have yielded stagnant-lid convection at ~0.9-2.0 times present-day speeds (Fig. S13D).

It is important to note that the behavior of the scalings highlighted in Eq. 29 and 30 depend on the exact value of Q, which varies for differing creep mechanisms and mantle hydration states (126). The value used herein is 300 kJ/mol, which characterizes diffusion creep in dry olivine. However, Q may take on lower values (e.g., 240 kJ/mol for diffusion creep in wet olivine) or higher values (e.g., 430-540 kJ/mol for dislocation creep in wet or dry olivine). Lower values (wet olivine) are unlikely since the mantle is poorly-hydrated today and was likely even less hydrated in the deep past (129). Higher values correspond to dislocation-dominated rather than diffusion-dominated creep behavior. While dislocation creep is most likely favored in the upper mantle today, the mantle's *effective* activation energy is probably at most comparable to that of diffusion creep due to non-Newtonian behavior. This is because the viscosity scaling in non-Newtonian systems is characterized by a reduced activation energy Q/n, where n is a

constant between ~1.7 and 3 (124, 125, 130). Therefore, even though dislocation creep is likely the dominant process, our assumption of a Newtonian rheology necessitates using a diffusion-like activation energy as an approximation (124, 125, 130).

S5.3. Speed limits and discussion. Substituting for parameter values in Eq. 28 yields a modern maximum mantle convection speed of $v_{M,max}$ ~9.4 cm/yr, which corresponds to rotation at up to ~0.85°/Myr. Likewise, for T_P 150-250°C hotter than today, fast mantle convection beneath an Archean stagnant-lid would have operated at v_{SL} ~ 8.5-19 cm/yr, corresponding to rotation at up to 0.76-1.7°/Myr (Fig. S13D). Incorporating these estimates of $v_{M,max}$ into Eq. 20-22, we arrive at estimates of the speed limit of non-TPW lithospheric net rotation in several scenarios (Main Text Fig. 5):

Archean stagnant-lids with T_P 150-250°C hotter than present:

$$v_{NR} \leq 2.8 - 6.1\,cm/yr = 0.25 - 0.55\,°/Myr\ (thin, rare\ cratons) \quad (31)$$
$$v_{NR} \leq 6.4 - 14\,cm/yr = 0.57 - 1.3\,°/Myr\ (intermediate\ Archean\ case) \quad (32)$$
$$v_{NR} \leq 7.5 - 17\,cm/yr = 0.68 - 1.5\,°/Myr\ (modern\ lithosphere\ structure) \quad (33)$$

Archean stagnant-lid speed limits are therefore less than or at most comparable to today's (≥0.8°/Myr), and the fastest model limits net rotation to 1.5°/Myr.

Reaching this speed limit at 3.2 Ga would have required an extraordinary and improbable set of conditions. As discussed after Eq. 19 above, this assumes that the Archean lithosphere had a modern structure and composition, and that most of the continental lithosphere would have since been reworked back into the mantle. The highest speed limits above also require that T_P would have been ~250°C hotter than at present to support the necessary convection speed, the maximum petrological estimate. Further, the arrangement of all cratons into a supercraton or supercontinent at the net rotational equator is possible but contrived. Since all plausible reconstructions evaluated in the present work result in simple motions only if the rotation pole was at or near the East Pilbara, the East Pilbara itself is a likely counterexample to this condition. The additional requirement of unidirectional flow under the entire cratonic lithosphere is very unlikely, especially since this specific convection pattern and lithospheric arrangement has not occurred in recent geologic time (116), let alone persisted for the ≥65 Myr intervals of rotations measured herein. Consequently, modern net rotations, when time-averaged over 65 Myr intervals, do not exceed ~40% of the modern (lower-bound) instantaneous speed limit. This suggests that ≥65 Myr time-averaged Archean speeds were likely no more than $0.4 \times 1.5\,°/Myr = 0.6\,°/Myr$ (Main Text Fig. 5). While it is unknown whether this "modern" approximation is appropriate for the Archean, one could argue that the scale of the Archean mantle convection pattern was likely smaller than today given its greater T_P and thus greater Ra_i, making it even more difficult to form a large and persistent patch of unidirectional upper mantle flow. In any case, supporting the required maximum-speed configuration for the longevity of rotations measured herein would have been unrealistic.

The motions measured in this work (~0.55°/Myr) are comparable to derived absolute speed limits on net rotation of Archean stagnant-lids, and their persistence for many tens of Myr, coupled with the exceptional conditions required to drive fast net rotations, suggests net rotation is likely not a suitable driver (Main Text Fig. 5). Net rotation of the lithosphere is therefore not our preferred mechanism to explain the observed rotations, suggesting instead either plate tectonics or true polar wander as drivers. Given that a TPW driver would also struggle to explain all of the observed motions due to geometry and duration (see Main Text), motion of the East Pilbara Craton between 3.34 and 3.18 Ga thus constitutes strong evidence for mobile-lid processes as the primary driver.

Table S1. Summary of directions and poles reported in this study. H components are reported by site, locality, and reversal polarity. Preferred values for each component-mean are in bold. Below the table, we also include versions of the H component pole KUH-R that are corrected for various amounts of possible pre-folding rotation of the SVS at ~2.93 Ga, which we discuss throughout the text and in Appendix S2.2, "*Structural uncertainties and corrections.*" Notes: *Not used due to lack of a sufficiently site-coherent H component; **All sites converted to R polarity.

	Site, Locality or Component	Sampling Location Lat, Long	n/N	Polarity	In Situ						Tilt-Corrected						Age
					Directions				Poles or VGPs		Directions				Poles or VGPs		
					Dec, Inc	α_{95}	R	k	Lat, Long	α_{95}	Dec, Inc	α_{95}	R	k	Lat, Long	α_{95}	
Overprints	*L mean*	*~21.5°S, 119.1°E*	*65/117*	-	***359.0°, -45.8°***	***3.7°***	***62.330***	***24.0***	***82.5°N, 054.2°W***	***3.8°***	*174.2°, -73.5°*	*4.5°*	*60.997*	*16.0*	*07.6°S, 064.4°W*	*7.3°*	***Recent***
	L2 mean	*~21.5°S, 119.1°E*	*15/117*	-	***063.1°, -08.9°***	***10.6°***	***14.000***	***14.0***	***26.6°N, 156.5°W***	***8.3°***	*130.0°, -26.8°*	*14.2°*	*13.288*	*8.2*	*29.5°S, 116.5°W*	*12.6°*	***0.54 Ga (?)***
	M mean	*~21.5°S, 119.1°E*	*45/117*	-	***307.8°, -25.0°***	***5.9°***	***41.849***	***14.0***	***39.7°N, 027.9°E***	***4.7°***	*315.0°, -59.4°*	*6.6°*	*41.156*	*11.4*	*46.5°N, 010.1°W*	*8.7°*	***2.22-1.78 Ga***
	M2 mean	*~21.5°S, 119.1°E*	*11/117*	-	***318.0°, 38.4°***	***13.7°***	***10.169***	***12.0***	***28.6°N, 074.4°E***	***11.7°***	*017.6°, -15.4°*	*13.7°*	*10.169*	*12.0*	*69.0°N, 173.6°E*	*10.1°*	***2.78 Ga?***
H Components	KUA1	21.525732°S, 119.111880°E	2/7	R	162.0°, -5.0°	11.1°	1.998	508.2	60.2°S, 099.3°W	-	218.6°, 51.6°	11.1°	1.998	508.2	54.2°S, 054.8°E	-	-
	KUA2*	21.525377°S, 119.111505°E	0/7	-	-	-	-	-	-	-	-	-	-	-	-	-	-
	KUA3	21.524122°S, 119.110972°E	3/7	R	143.9°, 22.2°	3.5°	2.998	1242.5	54.1°S, 140.7°W	-	159.3°, 71.9°	3.5°	2.998	1242.5	51.5°S, 137.2°E	-	-
	KUA4	21.523948°S, 119.110814°E	7/7	R	148.5°, 12.5°	4.4°	6.968	188.6	56.0°S, 129.1°W	-	185.9°, 66.7°	4.4°	6.968	188.6	61.9°S, 110.9°E	-	-
	Lower KUA mean	*~21.525°S, 119.111°E*	*3/4*	*R*	*151.7°, 10.1°*	*25.8°*	*2.917*	*24.0*	*57.9°S, 124.4°W*	*18.1°*	*195.2°, 65.4°*	*25.8°*	*2.917*	*24.0*	*61.0°S, 102.1°E*	*37.6°*	-
	KUA5	21.521750°S, 119.105946°E	6/7	N	300.4°, 01.3°	12.8°	5.824	28.4	27.8°N, 041.9°E	-	340.1°, -39.1°	12.8°	5.824	28.4	71.5°N, 023.6°E	-	-
	KUA6	21.520550°S, 119.106466°E	3/7	N	308.2°, -03.4°	26.9°	2.909	22.0	35.9°N, 043.3°E	-	343.8°, -47.8°	26.9°	2.909	22.0	73.6°N, 000.9°W	-	-
	KUA7*	21.520298°S, 119.106250°E	3/7	N	288.3°, 02.4°	61.6°	2.607	5.1	16.6°N, 037.2°E	-	330.9°, -29.6°	61.6°	2.607	5.1	61.9°N, 035.6°E	-	-
	KUA8	21.519767°S, 119.106075°E	2/7	N	326.9°, -31.2°	21.1°	1.993	142.7	58.4°N, 031.8°E	-	313.1°, -78.7°	21.1°	1.993	142.7	35.2°N, 041.6°W	-	-
	KUA9	21.519656°S, 119.105919°E	2/7	N	290.9°, -19.9°	25.2°	1.990	100.4	23.0°N, 026.8°E	-	309.7°, -44.5°	25.2°	1.990	100.4	44.0°N, 012.9°E	-	-
	Upper KUA mean	*~21.520°S, 119.106°E*	*4/5*	*N*	*306.0°, -13.6°*	*24.1°*	*3.806*	*15.5*	*36.3°N, 036.2°E*	*19.6°*	*329.8°, -53.3°*	*24.1°*	*3.806*	*15.5*	*59.1°N, 007.8°W*	*30.3°*	-
	KUB1	21.537091°S, 119.085237°E	7/12	R	175.6°, 35.6°	5.6°	6.948	115.5	85.5°S, 128.0°W	-	163.4°, 62.4°	5.6°	6.948	115.5	63.8°S, 147.0°E	-	-
	KUB2	21.536944°S, 119.085092°E	4/12	R	170.3°, 28.1°	12.7°	3.944	53.7	78.7°S, 116.9°W	-	173.6°, 55.4°	12.7°	3.944	53.7	74.5°S, 138.9°E	-	-
	KUB mean	*~21.537°S, 119.085°E*	*2/2*	*R*	*172.8°, 31.8°*	*19.1°*	*1.994*	*172.2*	*82.1°S, 119.9°W*	*15.1°*	*169.0°, 59.0°*	*19.1°*	*1.994*	*172.2*	*69.2°S, 144.0°E*	*24.3°*	-
	*Locality KUT**	*21.520174°S, 119.110247°E*	*0/30*	-	-	-	-	-	-	-	-	-	-	-	-	-	-
	N polarity mean	*~21.520°S, 119.106°E*	*4/5*	*N*	*306.0°, -13.6°*	*24.1°*	*3.806*	*15.5*	*36.3°N, 036.2°E*	*19.6°*	***329.8°, -53.3°***	***24.1°***	***3.806***	***15.5***	***59.1°N, 007.8°W***	***30.3°***	***3.265-3.235 Ga***
	R polarity mean	*~21.5°S, 119.1°E*	*5/6*	*R*	*159.5°, 19.2°*	*19.4°*	*4.757*	*16.5*	*67.7°S, 123.8°W*	*15.2°*	***183.2°, 63.4°***	***13.6°***	***4.877***	***32.6***	***65.7°S, 116.0°E***	***19.4°***	
	KUH-R pole (H mean)*	*~21.5°S, 119.1°E*	*9/11*	*both*	*144.4°, 17.4°*	*16.8°*	*8.224*	*10.3*	*54.2°N, 043.6°E*	*15.2°*	***166.2°, 60.1°***	***12.4°***	***8.554***	***18.0***	***65.6°S, 143.7°E***	***16.5°***	

KUH-R pole assuming 0° CW pre-folding rotation of SVS (minimum allowable value; as in Fig. S6A and tilt-corrected data above) ***65.6°S, 143.7°E 16.5°***

KUH-R pole assuming 20° CW pre-folding rotation of SVS (as in preferred reconstruction, Main Text Fig. 4) ***54.7°S, 163.5°E 16.5°***

KUH-R pole assuming 70° CW pre-folding rotation of SVS (maximum allowable value; as in Fig. S6B) ***19.0°S, 169.3°E 16.5°***

Table S2. Titanite U-Pb and trace element analyses. All ages are lower-intercept ages anchored to common Pb composition $^{207}Pb/^{206}Pb$ = 1.13.

Analysis	$^{238}U/^{206}Pb$	2σ	$^{207}Pb/^{206}Pb$	2σ	ρ	Concordance	Age (Ma)	2σ	Exclusions	Major/constituent elements (wt. %) Ca	Ti	Si	Fe	Al	Mg	Trace elements (ppm wt.) U	Th	P	Sc	V	Cr	Sr	Y	Zr	Nb	Sn	Sb	Hf	Ta	W	Rare Earth trace elements (ppm wt.) La	Ce	Pr	Nd	Sm	Eu	Gd	Tb	Dy	Ho	Er	Tm	Yb	Lu	Eu Eu*
KUB2-21	1.466	0.170	0.377	0.039	-0.286	0.878	**2837**	**421**		18.6	19.6	14.2	2.17	1.21	0.44	1.5	7.0	55	8.1	310	187	23.6	206	729	83	77	0.04	21.8	7.6	0.3	106	335	47	228	53.0	19.2	48.9	7.8	45.5	8.7	23.4	3.3	20.7	2.48	1.15
KUB1-44	1.295	0.055	0.460	0.014	0.078	0.896	**2860**	**159**		19.3	18.1	16.1	2.65	1.39	0.89	4.8	21.2	70	104.0	706	1820	73.1	315	506	118	139	0.30	14.0	8.4	4.6	128	460	70	370	93.0	37.3	80.0	12.9	79.0	13.2	32.1	4.4	23.4	2.37	1.32
KUB1-39	1.607	0.024	0.281	0.003	0.035	0.926	**2934**	**55**		19.3	19.1	16.2	2.52	1.42	1.28	27.8	46.8	114	17.1	423	452	43.1	410	679	177	100	0.27	13.9	21.5	1.7	222	812	103	503	106.0	43.5	94.3	14.8	90.0	16.4	43.4	5.8	33.3	3.32	1.33
KUB1-78	1.215	0.089	0.487	0.028	-0.274	0.921	**2940**	**308**		21.5	23.0	16.1	0.88	1.42	0.04	6.4	7.8	85	70.0	582	700	79.0	385	1242	194	163	0.19	21.8	9.8	5.0	94	480	74	346	91.0	39.7	78.0	12.5	81.6	14.5	38.8	5.0	24.2	2.31	1.44
KUB2-67	1.629	0.030	0.266	0.003	-0.302	0.941	**2952**	**68**		18.9	20.2	12.9	1.27	0.86	0.01	34.2	27.1	156	4.0	248	42	19.0	143	642	788	77	0.42	6.8	11.7	10.1	304	664	70	260	44.9	23.3	30.5	4.3	29.7	5.0	16.2	2.2	13.1	1.66	1.92
KUB2-22	1.622	0.025	0.267	0.003	-0.931	0.942	**2961**	**57**		19.2	20.8	13.7	1.20	0.78	0.01	24.3	8.2	93	2.0	194	8	21.7	123	489	566	86	0.22	3.8	16.2	5.9	339	870	99	356	51.4	27.7	37.8	4.7	26.6	5.4	15.2	2.1	13.5	1.35	1.92
KUB2-4	1.623	0.025	0.266	0.003	-0.551	0.943	**2964**	**58**		19.7	19.6	14.5	1.43	1.05	0.04	22.9	20.7	67	13.5	660	560	32.4	332	711	120	99	0.49	17.4	10.5	2.5	152	540	79	402	91.7	37.2	77.6	12.1	73.6	14.3	38.2	5.3	32.8	3.36	1.34
KUB1-52	1.541	0.039	0.306	0.006	-0.172	0.921	**2978**	**98**		18.9	20.1	14.1	1.17	0.96	0.17	8.7	24.5	47	5.2	324	433	20.2	300	296	176	46	0.10	6.3	12.5	0.3	88	360	54	277	67.7	22.2	67.2	10.4	65.5	12.7	32.7	4.4	23.0	2.17	1.00
KUB2-51-1	1.613	0.025	0.261	0.003	-0.175	0.956	**3008**	**61**		19.8	21.1	13.6	1.48	1.17	0.02	55.8	62.2	182	2.2	412	42	9.2	303	694	311	84	0.48	9.4	24.1	5.5	154	546	77	357	83.4	26.2	62.7	9.7	67.1	11.8	32.6	4.8	29.3	3.10	1.10
KUB1-73-3	1.592	0.032	0.270	0.003	0.429	0.951	**3018**	**79**		18.3	19.5	12.2	1.25	1.07	0.12	37.1	36.4	247	8.3	295	350	13.3	303	381	215	71	0.32	6.2	9.4	3.2	82	366	56	282	65.3	23.3	64.1	10.6	75.4	13.8	34.0	3.6	17.0	1.12	1.10
KUB1-63-2	1.560	0.040	0.287	0.006	-0.181	0.939	**3019**	**102**		18.3	20.1	13.6	1.93	1.60	0.56	19.9	69.1	166	6.6	216	1110	25.9	196	221	331	33	0.09	4.1	13.5	4.7	98	324	47	222	52.1	20.2	46.4	7.0	48.0	7.6	19.4	2.2	11.9	1.34	1.25
KUB1-19	1.449	0.027	0.346	0.012	0.092	0.917	**3022**	**95**		18.6	19.1	13.9	1.58	1.18	0.54	10.4	19.1	300	74.6	569	516	54.3	272	1367	211	124	0.22	31.4	9.5	4.0	125	452	66	319	77.7	30.2	69.7	10.2	62.0	11.9	31.0	4.2	24.7	2.68	1.25
KUB1-18	1.546	0.023	0.294	0.004	-0.239	0.936	**3025**	**60**		18.9	19.4	14.8	1.88	1.46	0.50	27.2	22.6	238	13.7	357	885	23.2	262	652	176	64	0.18	17.1	14.7	4.0	85	318	48	230	61.3	22.1	56.5	8.6	57.8	10.6	27.0	3.3	16.8	1.50	1.14
KUB2-10	1.593	0.023	0.267	0.003	-0.419	0.955	**3028**	**59**		20.6	21.2	14.3	1.12	0.59	0.13	26.3	2.1	123	2.6	86	59	39.4	21	376	174	150	0.20	2.5	17.6	3.6	135	217	18	62	7.4	6.5	5.4	0.7	4.6	0.9	2.6	0.3	2.6	0.32	3.14
KUB2-68	1.587	0.046	0.269	0.004	-0.412	0.955	**3035**	**114**		18.5	20.9	13.4	1.14	0.76	0.01	24.6	19.4	168	7.2	203	42	14.7	136	778	383	92	0.38	8.4	12.3	5.5	249	588	68	266	47.7	22.1	36.1	5.2	31.7	4.8	13.5	2.4	13.8	1.36	1.62
KUB2-69	1.575	0.047	0.275	0.003	-0.193	0.951	**3038**	**119**		18.2	21.7	13.4	0.92	0.45	0.02	23.5	0.8	115	3.4	85	21	27.9	26	380	209	175	0.32	2.7	15.0	4.3	114	206	21	67	9.4	6.4	6.6	0.8	5.7	1.0	2.5	0.4	2.8	0.40	2.47
KUB1-27	1.541	0.032	0.293	0.012	-0.864	0.939	**3039**	**101**		19.1	19.7	14.2	1.16	1.32	0.10	20.1	21.7	225	4.0	294	592	49.5	225	104	185	37	0.23	2.3	9.1	2.7	95	346	50	250	63.5	19.4	54.6	9.4	54.9	9.7	24.6	2.8	16.6	1.45	1.00
KUB2-38	1.479	0.057	0.326	0.009	-0.269	0.925	**3041**	**157**		18.3	19.9	14.0	1.26	0.75	0.08	5.7	7.4	107	7.2	178	93	18.3	77	517	157	68	0.10	6.5	9.0	3.0	136	336	41	145	26.3	13.1	20.6	2.8	17.1	3.3	8.5	1.3	6.5	0.75	1.72
KUB1-34	1.520	0.034	0.301	0.008	0.000	0.938	**3054**	**97**		18.8	19.1	14.5	1.30	1.30	0.25	11.4	25.5	131	6.6	226	304	17.2	179	232	190	50	0.20	5.5	8.8	1.6	69	278	41	193	45.5	17.2	44.0	6.7	40.7	7.6	16.5	2.1	11.3	0.92	1.17
KUB1-51	1.590	0.027	0.263	0.003	0.235	0.964	**3055**	**70**		19.5	18.7	16.0	2.60	1.78	1.04	13.4	25.2	320	7.1	188	527	28.8	138	285	183	27	0.15	7.6	9.8	3.1	73	260	33	161	32.8	14.3	32.0	4.9	33.4	5.5	14.2	1.7	9.4	0.97	1.35
KUB1-42	1.561	0.029	0.279	0.008	-0.455	0.951	**3056**	**81**		19.3	20.0	15.0	0.98	0.78	0.21	19.8	25.2	97	13.0	392	502	19.3	385	692	132	85	0.17	13.3	6.6	1.1	118	547	82	415	98.6	36.4	86.6	14.0	86.1	15.4	40.1	5.2	28.3	2.70	1.20
KUB2-46	1.577	0.032	0.269	0.003	-0.104	0.959	**3058**	**81**		19.5	21.0	13.6	1.14	0.83	0.04	26.4	4.6	124	3.4	180	309	30.2	56	342	377	80	0.17	3.4	7.0	21.5	183	345	34	117	20.2	12.6	15.2	2.1	13.7	2.3	7.2	0.9	5.7	0.63	2.20
KUB2-26	1.479	0.057	0.320	0.015	0.000	0.933	**3071**	**173**		19.4	19.6	13.9	1.67	1.05	0.27	8.9	6.9	700	5.3	237	850	39.6	97	634	273	87	0.20	11.5	9.7	6.8	134	331	39	163	32.1	16.9	26.7	4.0	25.1	4.2	12.2	1.6	9.3	1.12	1.76
KUB2-30	1.558	0.021	0.275	0.003	-0.209	0.959	**3080**	**56**		20.5	20.7	15.4	1.65	0.99	0.23	31.0	18.2	134	15.1	263	401	36.0	118	574	229	89	0.42	10.4	9.2	6.7	207	492	57	205	42.4	20.6	30.9	4.4	28.0	4.9	14.2	2.1	11.8	1.29	1.73
KUB1-60	1.475	0.036	0.318	0.008	-0.313	0.937	**3092**	**109**		18.4	19.3	14.6	1.27	1.35	0.12	6.9	5.2	80	12.7	326	262	14.2	233	199	123	63	0.09	4.0	7.1	1.5	44	190	31	166	43.8	16.1	42.9	7.4	46.7	9.7	24.3	2.9	12.8	1.12	1.13
KUB1-35	1.476	0.021	0.317	0.004	0.234	0.938	**3095**	**64**		19.6	18.8	15.6	2.17	1.65	0.77	19.7	25.3	198	28.2	611	1030	80.3	170	201	174	51	0.37	6.4	12.7	7.7	74	251	37	183	45.1	29.0	41.7	6.6	43.9	7.3	16.0	1.7	9.4	0.82	2.04
KUB1-64-1	1.572	0.027	0.264	0.003	-0.379	0.970	**3096**	**74**		17.7	19.3	12.4	1.21	1.55	0.02	25.6	33.5	282	7.6	219	316	21.3	116	94	154	25	0.07	1.8	9.5	6.4	69	227	30	124	24.4	15.0	22.5	4.5	27.2	4.8	9.8	0.9	5.8	0.53	1.95
KUB2-23	1.508	0.029	0.296	0.010	0.000	0.951	**3111**	**97**		18.8	19.6	15.1	2.09	0.84	0.66	57.0	14.4	196	33.8	217	397	45.4	126	852	1030	139	0.47	11.0	19.4	14.9	263	710	82	312	53.4	28.1	38.2	4.8	33.5	6.0	15.5	2.0	11.5	1.09	1.90
KUB1-16	1.439	0.034	0.333	0.014	-0.935	0.937	**3118**	**127**		19.6	19.0	16.0	2.60	1.42	1.19	27.4	51.4	78	9.8	426	339	32.3	411	990	186	78	0.25	18.8	14.3	1.5	248	910	123	571	118.2	43.6	110.8	15.1	93.7	17.5	44.5	6.0	37.4	3.53	1.16
KUB2-32	1.546	0.041	0.274	0.003	-0.695	0.966	**3119**	**115**		19.4	17.0	14.4	1.55	1.58	0.12	15.4	17.1	134	5.7	237	530	91.0	112	666	242	48	0.17	11.1	9.5	5.7	165	386	47	190	38.9	19.8	29.5	4.6	28.5	5.0	14.1	2.1	12.1	1.36	1.78
KUB2-62	1.553	0.046	0.270	0.004	0.294	0.970	**3119**	**128**		19.2	21.4	13.3	1.04	0.90	0.01	15.2	11.2	74	11.3	464	253	16.5	228	1600	192	96	0.32	30.8	15.9	0.6	89	395	56	286	63.5	24.2	54.4	7.9	55.0	8.6	27.5	3.4	21.3	1.97	1.26
KUB1-60	1.351	0.098	0.381	0.006	0.083	0.931	**3120**	**310**		17.4	20.3	13.3	1.19	1.21	0.13	7.3	12.0	57	61.0	577	318	37.2	254	443	123	125	0.29	9.9	6.1	6.4	77	288	47	238	63.2	24.9	55.1	9.0	60.0	10.8	27.0	2.9	17.8	1.64	1.29
KUB1-32	1.508	0.029	0.294	0.005	-0.737	0.953	**3121**	**86**		19.1	19.2	14.1	1.27	1.51	0.17	9.7	21.4	160	1.5	186	194	12.2	105	33	149	19	0.13	0.4	8.3	2.7	56	201	25	119	27.4	11.8	25.1	3.8	24.7	4.1	10.9	1.3	6.1	0.65	1.38
KUB1-28	1.342	0.035	0.385	0.015	-0.655	0.932	**3127**	**143**		19.5	18.5	14.4	1.47	1.38	0.51	12.7	11.7	1650	11.6	335	1698	79.0	189	233	150	43	0.17	7.4	10.1	2.2	78	247	34	176	47.0	18.8	45.1	6.8	42.0	7.5	17.6	2.1	11.2	1.00	1.24
KUB2-28	1.479	0.026	0.308	0.007	-0.768	0.948	**3130**	**86**		19.4	17.0	19.3	5.60	3.09	2.17	37.2	33.1	117	34.6	864	1770	77.8	415	933	151	129	0.61	25.0	9.9	6.6	196	785	113	499	120.4	53.1	106.0	16.3	103.6	19.1	48.9	6.5	42.1	4.91	1.43
KUB1-54	1.545	0.022	0.272	0.004	0.322	0.971	**3133**	**65**		18.9	21.4	14.2	1.10	0.68	0.14	18.8	19.7	56	4.0	496	310	13.6	359	271	81	85	0.09	3.7	7.8	0.4	137	631	95	471	93.8	41.9	87.8	13.4	86.5	16.2	41.3	5.7	32.1	3.02	1.41
KUB1-24	1.529	0.063	0.279	0.006	-0.406	0.966	**3138**	**181**		19.6	20.5	15.0	1.05	0.87	0.11	5.3	13.4	56	5.4	296	256	18.3	240	245	185	68	0.14	3.3	18.1	0.6	89	332	52	249	57.7	20.3	58.6	8.1	53.2	10.5	27.1	3.6	19.9	1.91	1.06
KUB1-30	1.466	0.035	0.313	0.008	-0.059	0.949	**3147**	**115**		19.4	20.5	14.4	1.12	1.15	0.22	6.3	22.9	370	5.2	320	637	34.0	253	166	193	34	0.17	3.4	9.2	0.6	88	339	49	252	64.7	19.6	59.2	9.5	57.9	10.3	26.1	3.4	17.6	1.80	0.96
KUB1-50	1.548	0.029	0.267	0.004	-0.517	0.978	**3149**	**83**		19.5	19.0	14.1	1.24	1.44	0.12	18.0	14.2	219	2.5	156	428	10.6	96	39	170	19	0.13	0.7	8.8	3.2	56	207	26	110	21.9	11.8	23.2	3.4	23.2	4.0	9.5	1.0	3.6	0.41	1.60
KUB2-27	1.389	0.054	0.355	0.021	-0.152	0.938	**3150**	**209**		19.4	20.5	14.9	1.82	0.90	0.31	7.0	8.6	99	4.3	127	194	37.2	57	569	197	85	0.21	6.6	9.3	4.8	148	291	31	107	19.7	10.2	15.6	2.0	13.9	2.6	7.3	1.0	5.5	0.74	1.77
KUB1-53	1.513	0.029	0.286	0.008	-0.847	0.964	**3151**	**96**		20.1	21.5	14.0	0.92	0.73	0.12	22.0	41.3	60	7.8	367	337	23.7	527	515	238	97	0.16	12.1	22.6	0.7	272	1072	149	682	141.8	59.6	121.6	18.3	113.8	21.6	54.1	7.1	40.1	3.72	1.38
KUB2-2	1.462	0.138	0.314	0.010	0.130	0.949	**3153**	**419**		19.4	19.7	14.2	1.49	1.11	0.01	2.3	5.7	68	11.1	294	113	13.2	87	267	71	29	0.27	5.4	7.1	2.1	95	220	25	114	22.2	14.1	20.3	3.1	19.2	3.6	10.8	1.6	9.7	1.07	2.02
KUB2-39	1.538	0.043	0.270	0.003	-0.242	0.976	**3157**	**125**		19.4	20.0	14.7	1.29	0.63	0.28	62.8	4.4	199	21.4	134	405	40.0	84	776	1480	190	0.27	7.0	20.3	12.3	444	1015	107	329	45.1	37.4	32.1	3.6	22.8	3.7	10.7	1.4	8.5	0.72	3.00
KUB2-18	1.462	0.026	0.311	0.013	-0.051	0.953	**3168**	**108**		19.4	19.7	17.2	3.52	1.70	1.05	39.9	24.6	211	11.1	255	361	57.9	254	1462	425	120	0.38	23.3	13.6	7.2	287	731	86	390	79.2	30.8	67.1	9.0	57.7	10.1	30.8	3.8	24.3	2.72	1.29
KUB1-66-1	1.466	0.052	0.308	0.011	0.000	0.955	**3171**	**171**		19.4	19.9	14.5	2.23	1.69	1.07	18.5	43.2	180	10.5	255	536	46.0	238	413	251	46	0.18	9.5	16.8	3.7	141	483	72	299	67.9	24.4	60.7	9.5	57.6	10.4	28.8	3.0	16.2	1.70	1.16
KUB2-33	1.418	0.060	0.334	0.015	-0.887	0.946	**3176**	**211**		20.0	18.6	16.3	2.67	1.05	1.09	15.4	6.2	79	20.5	229	680	42.8	91	440	230	86	0.25	8.6	9.0	1.7	170	406	45	166	30.4	19.3	23.6	3.7	23.5	4.3	9.9	1.5	8.6	1.15	2.20
KUB2-34	1.502	0.024	0.287	0.004	0.233	0.967	**3178**	**77**		18.9	18.5	14.9	1.62	0.86	0.25	18.5	27.1	155	29.0	243	203	41.4	171	613	140	84	0.26	9.5	7.7	6.8	350	761	78	278	60.5	29.3	45.3	6.8	44.4	7.9	19.2	2.9	17.9	2.05	1.71
KUB2-12	1.534	0.041	0.268	0.003	-0.544	0.983	**3185**	**123**		20.1	20.0	15.0	1.20	0.68	0.01	19.0	30.8	202	3.2	154	45	26.0	118	555	158	69	0.35	7.9	8.0	12.6	287	572	57	219	35.0	20.8	28.6	4.1	25.5	5.0	14.2	2.0	11.7	1.61	2.00
KUB2-76	1.433	0.073	0.323	0.024	0.000	0.952	**3193**	**274**		18.2	19.8	14.3	1.29	1.28	0.17	55.3	145.4	152	10.4	364	479	26.0	289	670	578	46	0.26	6.4	16.2	7.6	219	632	78	347	79.5	26.9	70.0	10.6	64.0	11.2	33.6	4.9	27.7	2.40	1.10
KUB2-25	1.416	0.039	0.332	0.017	0.000	0.950	**3194**	**162**		20.2	20.5	14.7	1.50	0.85	0.32	43.6	9.4	710	10.8	121	186	49.3	128	639	1060	140	0.36	6.7	13.1	17.5	407	989	108	387	57.5	36.8	44.3	5.4	35.0	6.2	15.9	2.1	12.5	1.43	2.22
KUB1-79	1.536	0.043	0.264	0.003	-0.104	0.989	**3199**	**131**		20.0	18.1	16.7	1.26	1.02	0.25	34.4	23.6	230	10.3	284	267	13.9	249	990	161	72	0.42	18.8	13.3	3.1	79	359	51	258	58.3	20.6	55.0	9.1	58.7	11.3	29.8	3.1	18.5	1.46	1.11
KUB1-4	1.294	0.020	0.400	0.009	0.000	0.944	**3199**	**93**		19.0	19.4	14.0	1.18	1.12	0.11	14.5	13.3	92	161.1	844	305	124.0	385	1043	128	142	0.33	24.2	5.7	7.5	144	502	81	388	96.7	43.0	92.1	13.7	86.7	16.4	46.4	5.9	32.9	3.29	1.39
KUB1-36	1.357	0.023	0.363	0.004	-0.413	0.946	**3206**	**83**		19.5	19.6	15.1	1.14	1.41	0.06	16.3	8.4	144	166.6	1061	717	154.6	347	803	221	380	0.45	23.4	10.7	10.3	110	465	77	407	118.0	59.3	90.9	15.9	96.3	14.7	32.8	4.5	23.5	2.50	1.75
KUB2-51-2	1.543	0.046	0.257	0.003	0.544	0.997	**3212**	**141**		19.6	20.9	13.0	1.07	0.84	0.01	20.4	65.0	165	4.3	360	76	10.5	223	1212	221	84	0.43	20.1	18.5	6.5	120	427	58	270	67.0	25.0	60.4	8.9	49.8	9.1	27.3	3.2	19.2	2.32	1.20
KUB1-31	1.462	0.053	0.303	0.011	0.000	0.964	**3213**	**185**		19.2	19.5	14.6	1.08	1.19	0.17	12.3	16.0	90	14.6	521	1484	42.3	234	370	125	86	0.23	10.6	10.6	3.8	103	401	56	273	70.0	34.3	59.2	9.1	58.6	9.8	22.5	3.0	16.7	1.60	1.62
KUB1-8	1.431	0.021	0.319	0.006	-0.684	0.958	**3221**	**81**		19.6	20.0	15.1	1.76	1.06	0.55	18.7	31.6	119	36.7	496	515	44.9	448	861	184	170	0.21	15.6	8.4	2.6	126	540	88	430	111.7	35.7	99.1	15.8	101.3	18.0	50.0	6.1	32.2	2.73	1.03
KUB1-75-1	1.490	0.049	0.284	0.005	-0.325	0.977	**3228**	**161**		17.8	21.0	12.4	1.41	1.01	0.39	16.4	33.7	72	3.1	423	243	14.8	362	444	211	79	0.15	12.8	40.5	0.9	219	810	117	513	112.4	43.2	93.0	14.1	86.9	16.9	40.9	5.2	31.3	2.70	1.29
KUB2-40	1.495	0.035	0.282	0.005	0.671	0.979	**3228**	**115**		19.2	21.0	13.6	0.94	0.55	0.01	12.7	6.0	125	2.3	128	35	30.9	27	304	74	103	0.28	2.3	18.1	8.6	108	189	18	55	8.9	6.0	7.8	0.9	5.8	1.4	3.6	0.5	3.4	0.41	2.18
KUB2-37	1.449	0.069	0.306	0.018	-0.208	0.966	**3237**	**256**		19.8	17.1	12.9	1.43	0.96	0.04	25.5	27.5	90	46.5	367	143	170.0	215	593	304	73	0.25	12.7	19.5	3.1	161	463	59	230	55.6	21.7	46.4	7.8	50.4	8.7	24.9	3.6	20.9	1.99	1.30
KUB1-14	1.449	0.022	0.306	0.005	-0.656	0.967	**3239**	**81**		19.4	19.2	14.6	1.30	1.12	0.17	18.1	43.7	211	9.3	323	642	21.5	321	714	164	86	0.06	13.2	14.1	2.9	105	459	71	340	84.5	35.3	76.7	12.0	73.3	13.9	37.4	4.4	22.8	1.89	1.34

Table S2 (continued). Titanite U-Pb and trace element analyses.

Analysis	^{238}U/^{206}Pb	2σ	^{207}Pb/^{206}Pb	2σ	ρ	Concordance	Age (Ma)	2σ	Exclusions	Major/constituent elements (wt. %) Ca	Ti	Si	Fe	Al	Mg	Trace elements (ppm wt.) U	Th	P	Sc	V	Cr	Sr	Y	Zr	Nb	Sn	Sb	Hf	Ta	W	Rare Earth trace elements (ppm wt.) La	Ce	Pr	Nd	Sm	Eu	Gd	Tb	Dy	Ho	Er	Tm	Yb	Lu	Eu Eu*
KUB1-2	1.511	0.027	0.270	0.003	-0.052	0.990	**3240**	**90**		19.4	19.7	13.8	0.97	1.14	0.01	13.8	46.1	199	16.2	300	229	17.9	240	506	283	59	0.03	7.1	16.1	1.8	55	212	34	172	48.6	16.2	49.2	8.3	53.6	10.2	24.7	2.8	13.5	1.04	1.01
KUB1-9	1.504	0.046	0.274	0.006	-0.841	0.988	**3246**	**154**		19.8	19.8	13.9	1.04	0.90	0.07	15.3	39.0	780	5.4	365	387	42.0	384	396	104	42	0.13	7.1	8.6	1.3	115	444	69	339	88.2	28.2	83.7	12.5	80.4	16.1	43.1	5.5	29.5	2.44	1.00
KUB1-3	1.290	0.045	0.394	0.018	-0.624	0.952	**3252**	**215**		18.7	17.4	20.2	5.38	2.30	3.29	29.2	73.0	166	22.6	399	537	108.0	469	2940	286	109	0.23	72.4	28.3	2.0	268	902	116	566	127.1	40.1	112.6	16.9	103.5	20.0	53.2	7.1	42.9	4.24	1.02
KUB1-5	1.526	0.018	0.259	0.003	-0.411	1.002	**3254**	**61**		20.1	19.7	14.2	1.29	1.19	0.01	35.6	82.0	479	2.2	257	139	10.1	310	122	206	45	0.13	0.5	10.6	2.5	75	300	44	214	54.3	18.4	53.5	9.5	64.8	12.9	32.2	3.5	16.3	1.33	1.04
KUB1-13	1.361	0.026	0.349	0.006	0.000	0.959	**3284**	**107**		19.0	18.1	16.2	3.02	1.62	1.35	11.1	19.1	115	6.6	330	484	27.0	275	372	146	44	0.14	7.4	9.0	1.4	82	312	47	236	66.1	19.0	60.1	9.1	61.1	11.2	31.4	3.8	20.3	2.21	0.92
KUB2-42	1.389	0.037	0.332	0.011	-0.582	0.964	**3290**	**160**		19.4	19.0	15.9	2.07	0.76	0.83	11.4	6.9	117	14.2	219	534	33.2	84	433	99	103	0.43	4.7	18.9	7.7	99	244	31	119	25.3	9.1	20.1	3.0	19.6	3.3	9.7	1.3	8.7	0.93	1.23
KUB2-72	1.488	0.053	0.274	0.004	0.074	0.996	**3297**	**191**		18.6	18.9	13.9	1.53	1.33	0.27	15.4	30.0	225	20.2	336	743	19.8	124	513	161	30	0.22	9.6	11.2	4.2	66	213	28	123	31.3	13.1	27.7	4.4	25.6	4.4	13.7	1.8	12.0	1.17	1.36
KUB1-37	0.997	0.063	0.556	0.024	-0.684	1.018	**3298**	**403**		18.4	18.1	13.4	1.35	1.24	0.06	3.1	9.0	81	128.0	867	149	78.6	325	773	141	288	0.26	18.5	5.2	10.2	90	351	61	314	93.1	38.8	82.7	12.7	84.6	13.8	32.4	4.5	23.8	2.27	1.35
KUB2-52	1.495	0.153	0.270	0.008	0.319	0.999	**3299**	**545**		18.5	20.7	13.3	1.02	1.02	0.02	3.7	4.2	46	9.3	312	253	10.8	121	533	158	50	0.15	8.7	8.8	0.5	51	181	27	145	33.6	14.1	31.4	4.5	24.1	4.4	14.6	1.6	11.8	1.23	1.32
KUB1-76	1.490	0.051	0.272	0.005	-0.174	0.998	**3303**	**186**		18.5	20.7	12.9	1.04	0.80	0.24	15.3	35.2	63	4.7	340	273	21.9	413	527	202	86	0.18	14.4	37.7	0.3	232	892	127	562	126.0	49.5	103.4	16.6	99.2	18.1	47.0	5.9	34.3	3.33	1.32
KUB1-25	1.171	0.089	0.455	0.017	-0.297	0.970	**3306**	**427**		19.2	17.8	17.5	2.97	1.62	1.38	3.0	3.4	60	47.6	416	2437	66.7	130	1440	217	67	0.13	39.4	15.0	4.0	38	136	22	114	35.2	20.4	32.7	6.0	35.9	5.5	13.0	1.5	7.5	0.64	1.84
KUB2-9	1.488	0.030	0.271	0.004	0.365	1.000	**3314**	**114**		19.7	20.0	15.1	1.41	0.76	0.19	64.7	7.2	146	6.6	119	237	43.7	85	605	791	160	0.33	4.5	10.8	6.3	313	720	75	263	34.6	28.1	25.8	3.3	19.7	3.8	10.8	1.6	9.3	0.87	2.87
KUB1-75-2	1.395	0.049	0.325	0.009	-0.836	0.970	**3317**	**199**		18.1	20.3	15.1	2.12	1.29	0.97	15.2	22.9	58	8.6	450	407	27.1	362	331	159	66	0.25	8.8	21.8	1.1	144	566	83	411	84.9	31.6	77.0	12.2	83.9	14.7	37.9	4.6	23.5	2.58	1.19
KUB1-29	1.362	0.041	0.343	0.012	-0.646	0.965	**3319**	**184**		19.0	18.5	13.2	0.96	1.02	0.17	9.9	35.6	2900	21.4	406	529	135.0	324	245	207	67	0.21	5.6	9.4	2.9	150	447	66	343	87.4	24.4	84.2	12.4	76.5	13.6	33.7	4.1	22.5	2.15	0.87
KUB1-1	1.449	0.029	0.291	0.004	-0.587	0.988	**3331**	**115**		19.6	20.7	15.9	2.37	1.39	0.87	12.0	32.4	114	13.4	381	255	36.3	408	1410	196	61	0.10	24.2	10.8	1.6	114	432	67	349	92.3	24.2	91.2	13.6	87.1	16.6	44.6	5.2	30.2	2.93	0.80
KUB2-11	1.497	0.058	0.262	0.005	-0.316	1.012	**3338**	**221**		19.4	21.4	13.8	0.76	0.48	0.01	7.2	23.8	57	5.6	907	139	15.7	528	980	113	140	0.18	29.2	6.2	0.4	260	954	143	715	160.0	58.6	141.1	20.7	121.3	23.1	63.9	8.4	48.7	5.10	1.19
KUB2-15	1.495	0.031	0.261	0.003	-0.049	1.015	**3355**	**121**		19.9	20.5	14.4	1.42	0.90	0.07	15.3	44.6	179	6.3	248	118	15.3	238	1332	248	99	0.16	21.3	9.8	8.6	300	677	75	315	62.6	27.6	55.6	8.4	51.4	9.9	29.5	4.1	25.0	2.85	1.43
KUB1-33	1.217	0.090	0.422	0.023	-0.896	0.969	**3360**	**472**		19.4	17.7	20.5	5.96	3.10	3.48	9.1	21.9	182	20.8	365	566	73.0	227	335	145	42	0.15	8.8	11.9	1.8	104	379	56	272	63.3	20.8	53.4	8.0	51.5	9.2	24.1	2.9	17.2	1.95	1.09
KUB2-36	1.453	0.067	0.282	0.008	0.000	1.001	**3379**	**285**		19.2	19.0	14.4	2.17	1.14	0.24	12.7	19.5	263	9.0	311	279	18.0	118	436	106	51	0.30	10.2	9.1	5.2	121	304	34	145	30.0	18.5	28.2	4.1	26.7	4.7	13.4	1.7	12.2	1.38	1.94
KUB2-24	1.477	0.030	0.268	0.004	0.203	1.012	**3380**	**126**		19.7	20.7	14.2	1.33	0.80	0.02	16.3	31.6	231	6.6	312	132	17.2	265	1230	193	97	0.30	24.0	14.1	7.9	395	870	100	409	79.6	35.7	65.7	9.8	59.1	11.1	31.7	4.6	28.2	3.11	1.50
KUB2-29	1.344	0.107	0.343	0.026	-0.804	0.975	**3398**	**540**		20.6	21.2	13.7	1.08	0.61	0.04	4.4	2.7	108	11.0	162	184	29.2	45	379	49	113	0.14	5.1	8.0	5.2	63	142	17	69	13.2	6.4	11.2	1.5	11.5	2.0	5.9	0.7	5.5	0.62	1.61
KUB1-69	1.410	0.042	0.301	0.004	-0.171	0.994	**3423**	**199**		19.4	20.8	14.2	2.01	1.32	0.92	21.7	34.7	150	6.6	351	397	24.6	339	651	213	56	0.24	16.1	15.4	3.9	124	450	69	331	75.1	23.6	72.0	11.9	80.8	13.6	40.9	4.0	24.3	2.25	0.98
KUB1-71	1.422	0.037	0.292	0.004	-0.619	1.001	**3438**	**179**		19.0	19.8	13.2	1.61	1.23	0.54	21.7	37.5	197	6.4	257	467	28.0	301	146	212	39	0.34	2.4	8.5	3.8	104	371	56	279	70.0	19.3	62.5	10.5	62.7	11.8	29.7	3.4	15.4	1.41	0.89
KUB2-7	1.304	0.064	0.361	0.015	-0.535	0.978	**3445**	**363**		19.6	17.6	13.9	1.73	0.67	0.67	7.4	8.1	161	26.2	180	1180	81.0	53	468	73	66	0.34	8.6	7.0	7.1	114	221	23	88	17.0	10.7	14.6	2.0	11.3	2.3	6.3	1.0	5.7	0.79	2.08
KUB1-66-2	1.377	0.040	0.317	0.004	0.403	0.990	**3452**	**206**		18.6	19.5	13.0	1.24	1.36	0.09	21.1	35.9	189	85.4	711	405	82.4	285	730	189	175	0.21	19.7	11.0	7.2	109	404	61	318	82.9	33.4	70.0	11.5	76.5	12.2	30.8	3.4	19.0	1.69	1.34
KUB2-5	1.381	0.070	0.313	0.015	-0.755	0.993	**3465**	**385**		18.9	19.8	14.5	1.62	0.92	0.25	10.8	10.3	109	19.8	301	502	34.4	118	314	152	56	0.44	6.4	6.3	6.5	147	326	37	164	35.0	16.3	27.7	4.5	28.3	5.5	14.1	2.1	11.3	1.34	1.60
KUB2-3	1.247	0.042	0.392	0.023	-0.339	0.979	**3469**	**333**		19.6	19.7	14.9	2.05	1.29	0.31	4.1	13.6	116	8.6	270	333	28.4	210	568	103	61	0.13	14.3	9.2	0.7	106	329	46	234	53.2	17.3	46.4	7.3	47.5	8.9	24.3	3.7	19.5	2.28	1.06
KUB2-71	1.473	0.052	0.258	0.004	-0.197	1.033	**3472**	**257**		18.1	18.8	13.3	1.53	1.57	0.02	19.2	6.9	178	1.2	364	29	7.2	91	203	100	27	0.33	2.3	9.4	4.3	71	238	31	136	30.1	12.4	25.5	3.3	22.0	3.7	9.1	1.4	8.0	1.00	1.36
KUB1-77	1.435	0.051	0.276	0.004	0.197	1.021	**3517**	**290**		18.6	21.0	13.8	0.86	0.72	0.03	13.4	13.8	79	34.1	472	550	22.9	351	598	180	76	0.15	12.6	11.7	2.4	125	480	73	360	77.4	29.0	76.0	12.7	75.0	15.5	39.8	4.9	28.2	2.32	1.15
KUB2-43	1.372	0.026	0.311	0.010	-0.330	1.001	**3535**	**191**		19.4	21.0	14.0	0.75	0.45	0.01	120.1	55.6	146	4.0	504	2480	28.4	588	1000	202	415	0.54	19.3	6.8	2.4	694	2086	262	929	190.0	147.5	156.5	23.4	148.2	25.7	76.1	10.4	67.1	8.29	2.61
KUB2-6	1.418	0.062	0.281	0.005	-0.698	1.021	**3562**	**401**		19.3	19.0	13.2	1.74	0.96	0.12	22.5	51.7	1490	9.3	181	88	55.0	117	516	239	56	0.52	7.0	12.0	8.6	268	527	53	210	35.8	19.1	28.2	4.2	26.6	5.0	13.7	2.0	12.0	1.39	1.83
KUB1-73-2	1.215	0.047	0.402	0.013	-0.216	0.988	**3567**	**393**		18.2	19.6	13.6	1.10	1.52	0.08	11.9	9.9	118	58.6	823	521	111.4	207	271	105	68	0.43	8.6	7.6	6.9	61	180	29	148	38.9	21.2	44.7	7.0	47.8	9.2	23.9	2.6	14.2	1.65	1.55
KUB2-49	1.332	0.060	0.328	0.008	0.223	1.000	**3616**	**500**		19.1	19.8	11.8	0.80	0.63	0.03	15.3	19.5	61	12.3	395	194	67.0	328	818	134	119	0.08	14.4	9.6	1.0	201	647	89	441	96.0	39.0	83.0	13.4	76.2	14.4	38.4	5.0	28.8	3.18	1.33
KUB1-10	1.241	0.081	0.394	0.019	-0.836	0.981	**3886**	**520**	<15% Ti	20.2	12.1	10.3	1.17	0.74	0.37	11.1	19.1	278	19.1	282	125	470.0	216	572	172	72	0.05	10.1	10.3	2.6	91	322	46	241	57.2	20.1	51.1	8.0	49.3	9.8	25.0	3.3	17.3	1.66	1.13
KUB2-73	1.416	0.072	0.260	0.003	-0.095	1.060	**0**	**185**	>5% rev. disc.	17.9	21.2	12.5	1.13	1.19	0.02	11.4	30.7	175	2.1	468	504	9.5	180	331	127	46	0.32	5.2	8.4	3.2	82	291	39	184	47.1	17.1	43.4	6.6	39.7	7.4	20.4	2.6	15.4	1.72	1.15
KUB1-15	0.895	0.046	0.604	0.023	-0.813	1.070	**3416**	**432**	>5% rev. disc.	18.8	18.4	14.8	1.39	1.68	0.19	6.2	4.4	111	366.0	1501	350	253.0	350	1540	198	382	0.61	40.0	6.2	15.0	161	549	90	435	129.0	59.9	102.0	16.7	100.0	16.2	39.5	5.0	32.5	3.52	1.59
KUB2-1	1.024	0.101	0.364	0.043	0.000	1.166	**0**	**506**	>5% rev. disc.	19.8	18.5	14.3	1.80	1.42	0.27	5.1	8.3	56	25.3	603	470	26.9	345	360	48	35	0.21	9.8	5.4	1.3	75	317	53	276	76.3	34.3	69.4	12.0	76.8	15.1	44.6	5.7	36.0	4.36	1.44
KUB1-73-1	1.178	0.130	0.298	0.006	-0.465	1.146	**0**	**463**	>5% rev. disc.	18.0	20.1	12.5	1.03	1.17	0.03	5.8	16.5	122	10.0	309	287	12.4	230	232	168	72	0.19	5.1	7.1	3.0	50	223	39	205	47.8	18.5	44.9	8.6	51.1	10.9	28.5	2.7	13.9	1.42	1.22
KUB2-45	0.952	0.109	0.503	0.039	-0.665	1.089			>5% rev. disc.	19.3	15.9	17.3	3.90	0.95	1.98	18.1	8.5	95	55.7	256	902	64.0	108	742	452	79	0.53	13.9	13.6	4.8	199	495	57	218	43.0	24.9	32.2	5.3	30.4	5.4	12.8	1.9	10.1	1.19	2.04
KUB2-50	1.385	0.169	0.264	0.005	-0.121	1.072			>5% rev. disc.	19.2	20.4	14.0	1.33	1.02	0.04	7.9	8.9	98	2.5	296	69	11.0	110	500	124	53	0.30	8.5	15.7	1.8	144	348	35	183	33.1	16.9	26.6	3.4	22.3	4.8	13.5	1.9	10.0	1.27	1.74
KUB2-41	1.031	0.128	0.367	0.010	-0.480	1.157	**0**	**549**	>5% rev. disc.	19.2	19.9	13.4	0.83	0.53	0.03	2.5	5.9	65	3.9	146	198	42.2	98	341	42	94	0.12	7.4	9.8	1.4	81	218	29	125	28.3	9.7	24.9	4.1	23.6	4.4	10.9	1.3	9.9	0.96	1.11
KUB2-54	1.136	0.142	0.333	0.006	-0.220	1.120	**0**	**524**	>5% rev. disc.	19.5	19.8	12.9	1.27	1.29	0.02	4.1	8.7	54	31.4	496	52	20.4	173	470	86	31	0.43	11.4	10.3	2.9	80	227	35	162	39.4	19.2	35.6	5.5	37.4	7.0	18.6	2.8	18.2	2.44	1.56
KUB2-74	1.266	0.177	0.269	0.007	-0.635	1.136			>5% rev. disc.	18.8	19.5	13.2	1.09	1.14	0.01	2.8	5.6	41	6.3	386	84	10.4	146	633	170	46	0.36	11.9	7.9	1.1	36	167	26	121	34.2	11.1	34.0	5.4	32.0	5.7	17.8	1.8	13.1	1.43	0.99
KUB1-24	1.031	0.181	0.411	0.014	0.208	1.107	**0**	**732**	>5% rev. disc.	21.3	21.2	15.1	2.48	0.92	0.08	2.2	6.2	38	49.2	750	292	37.8	234	292	103	119	0.29	6.0	9.6	5.2	99	406	56	248	63.2	24.8	50.7	8.9	56.3	8.9	29.0	3.5	24.1	2.13	1.34
KUB2-14	0.826	0.178	0.562	0.030	-0.454	1.158	**0**	**904**	>5% rev. disc.	19.5	19.6	14.7	1.18	1.05	0.02	1.4	6.6	44	76.0	448	59	32.7	219	639	59	62	0.14	13.4	3.1	4.2	88	312	46	229	54.7	21.0	46.5	7.8	49.7	9.7	26.7	3.4	21.4	2.43	1.27
KUB1-79b	0.787	0.471	0.352	0.011	-0.182	1.422			>5% rev. disc.	18.8	20.4	13.3	0.66	0.61	0.01	1.1	3.5	43	10.8	326	446	14.9	206	603	110	105	0.15	10.6	7.8	0.7	57	292	44	197	50.5	21.4	45.6	7.4	43.4	8.0	24.8	3.5	17.0	1.79	1.36
KUB2-75	1.418	0.112	0.275	0.006	0.093	1.031	**3629**	**902**	high age error	19.4	21.6	13.3	1.22	1.22	0.01	6.2	18.2	116	12.8	440	71	9.5	156	563	98	45	0.20	10.2	7.6	1.6	47	181	26	128	32.3	13.6	34.1	5.5	34.1	6.2	17.8	2.4	13.2	1.37	1.25
KUB1-43	1.325	0.120	0.358	0.047	-0.900	0.969	**3370**	**649**	high age error	19.6	16.5	11.3	0.74	0.55	0.01	17.9	28.2	135	9.0	235	221	134.0	368	1180	212	105	0.16	15.0	14.9	0.7	97	499	79	400	97.5	37.0	85.8	13.5	87.1	15.7	37.8	5.1	24.5	1.99	1.23
KUB1-26	1.353	0.160	0.314	0.011	0.000	1.007	**3635**	**1389**	high age error	18.5	19.3	14.5	1.40	1.16	0.57	12.6	27.6	130	6.5	340	920	33.8	302	203	175	39	0.26	5.4	9.1	1.2	92	373	58	292	79.4	21.7	73.1	11.0	70.9	12.3	29.3	4.1	20.2	1.92	0.87
KUB1-63-1	1.318	0.160	0.343	0.008	0.285	0.991	**3543**	**1050**	high age error	17.7	19.3	13.1	1.04	1.24	0.22	3.6	11.1	52	23.9	287	415	23.8	162	263	199	77	0.10	5.4	7.2	1.9	43	170	29	149	40.5	17.0	36.8	6.1	39.7	6.8	16.8	2.0	9.1	0.78	1.34
KUB1-73-4	1.433	0.185	0.338	0.009	-0.241	0.934	**3111**	**548**	high age error	18.8	17.4	13.1	1.21	1.25	0.32	5.1	5.9	51	19.6	373	304	57.2	230	244	126	76	0.14	4.9	5.9	2.2	43	190	32	173	44.0	16.7	44.7	7.9	49.7	9.6	26.8	2.6	12.6	1.09	1.15
KUB1-17	0.990	0.157	0.559	0.032	-0.697	1.022	**3308**	**908**	high age error	19.5	19.8	13.9	0.92	0.86	0.01	1.8	7.1	51	39.3	435	195	20.7	306	366	87	116	0.05	7.7	3.7	1.9	64	300	51	251	67.9	27.0	66.3	10.5	64.5	12.0	32.6	4.2	22.7	1.94	1.23
KUB1-23	1.389	0.328	0.336	0.039	0.137	0.959	**3264**	**1222**	high age error	18.4	19.8	14.1	0.85	0.62	0.04	1.2	4.2	35	8.6	329	66	14.0	273	212	85	79	0.09	3.3	6.4	0.7	63	330	49	231	60.3	23.8	56.0	8.9	60.2	12.0	33.1	4.6	28.0	2.61	1.25
KUB2-64	1.351	0.913	0.406	0.017	0.256	0.908	**2985**	**2527**	high age error	17.6	19.3	11.4	0.99	0.84	0.02	1.7	1.9	48	12.2	543	212	57.7	166	580	82	68	0.00	12.4	5.3	0.9	42	183	29	150	41.2	16.2	40.1	5.8	37.9	6.9	18.6	2.3	15.2	1.79	1.21
KUB2-78	2.564	6.246	0.587	0.031	0.000	0.474	**1183**	**2747**	high age error	17.8	19.0	12.6	1.14	1.10	0.02	0.5	2.0	63	6.4	352	30	18.9	73	362	129	24	0.11	5.3	8.0	0.4	23	90	15	64	16.5	6.9	18.5	2.1	15.0	2.8	8.6	1.3	7.1	0.59	1.20
KUB2-53	9.091	80.17	0.390	0.013	0.000	0.174	**3871**	**181248**	high age error	18.9	20.5	12.3	1.13	0.92	0.13	1.0	5.2	56	33.2	363	530	20.1	185	911	87	61	0.25	26.2	8.5	1.4	67	224	36	181	46.8	14.9	39.1	6.8	44.8	7.4	21.9	3.1	17.5	1.92	1.06
KUB2-31	1.221	0.041	0.359	0.006	-0.294	1.030	**0**	**128**	no defined age	19.4	18.2	16.9	4.99	1.96	1.45	8.2	21.0	133	107.3	408	399	101.0	272	1281	186	96	0.30	30.7	11.3	1.5	126	444	68	303	70.1	23.2	61.6	10.1	66.0	11.8	30.2	4.5	28.8	3.09	1.08
KUB2-8	1.050	0.109	0.460	0.021	0.000	1.047	**0**	**411**	no defined age	19.0	16.5	13.3	1.54	0.59	0.49	2.9	3.8	112	20.8	231	369	205.0	92	553	60	59	0.21	10.8	6.3	3.5	61	181	24	116	24.1	11.5	21.3	3.2	22.2	3.7	11.7	1.5	9.5	1.20	1.55
KUB2-44	1.124	0.127	0.400	0.043	0.000	1.050	**0**	**492**	no defined age	20.0	20.2	14.0	1.33	0.77	0.18	2.7	6.5	37	11.2	412	300	20.1	294	1080	113	97	0.08	21.7	7.2	0.5	103	415	60	300	77.8	30.5	69.4	10.5	68.0	12.2	32.5	4.2	25.4	2.83	1.27
KUB1-64-2	1.176	0.180	0.377	0.014	-0.483	1.038	**0**	**587**	no defined age	18.1	20.6	13.1	1.10	1.16	0.24	4.2	11.6	48	32.8	416	1020	23.9	226	391	164	121	0.27	8.8	8.8	4.4	73	295	47	245	61.9	23.0	56.1	8.5	52.9	9.3	25.9	3.0	11.8	1.40	1.19

Table S3. Parameters referred to in our derivation of net rotation speed limits (Appendix S5).

Symbol	Values where used	Description
$\dot{\boldsymbol{\varepsilon}}$		Coupling zone horizontal strain rate
$\boldsymbol{\sigma}$		Coupling zone horizontal shear stress
η		Average coupling zone viscosity
$\boldsymbol{\tau}$		Torque on lithosphere applied by basal traction
θ		Polar angle (colatitude) relative to net rotation axis
ϕ		Longitude relative to net rotation axis
r		Earth radius
h		Coupling zone thickness
h_C		Coupling zone thickness under cratons
h_O		Coupling zone thickness under oceans
C	Today: ~7; Archean: ~7-20 or greater	Cratonic/oceanic lithosphere-mantle coupling ratio
A		Surface area of Earth
A_C		Surface area of cratonic lithosphere
A_O		Surface area of oceanic lithosphere
f	Today: 0.4; Archean: 0.05-0.4	Craton-occupied fraction of Earth's surface area
$\Delta\boldsymbol{v}$		Velocity difference across coupling zone
$\boldsymbol{v_L}$		Surface velocity field of lithosphere
$\boldsymbol{v_M}$		Horizontal velocity field at top of lower mantle
$v_{M,max}$		Velocity of fast mantle convection (under cratons)
v_{NR}		Velocity of lithospheric net rotation
v_{ML}	today: 10 cm/yr	Velocity of fast convection under mobile-lids
v_{SL}		Velocity of fast convection under stagnant-lids
Ra_i		Mantle Rayleigh number
Θ		Frank-Kamenetskii parameter
a_{RH}	2	Viscosity variability reduction under stagnant-lids
T_S	28°C = 300 K	Surface temperature
T_P	Today: T_{P0}; Archean: 1500-1600°C	Mantle potential temperature
ΔT		Mantle potential temperature contrast $= T_P - T_S$
T_{P0}	1350°C	Modern mantle potential temperature
c	0.07	Scaling constant for convection velocities
κ	1×10^{-6} m^2/s	Mantle thermal diffusivity
d	2890 km	Mantle thickness
η_0	10^{21} Pa×s	Reference mantle viscosity at T_{P0}
η_i		Effective mantle viscosity in convection
Q	300 kJ/mol	Creep activation energy
n	~1.7 to ~3	Non-Newtonian stress exponent
R	≡ 8.314 J/(mol×K)	Gas constant
ρ	4500 kg/m^3	Mantle density
α	3×10^{-5} K^{-1}	Mantle thermal expansivity
g	10 m/s^2	Gravitational acceleration

Dataset S1 (separate file). Component fit data for all samples. This Excel file lists component directional fits for all samples by type (H, HC, M2, etc.). Each fit direction is reported in *in-situ* and tilt-corrected coordinates (tilt-correction includes the within-SVS vertical axis rotations and fold unplunging). Full demagnetization data for all samples are also available via the publicly-accessible MagIC Database without restriction at earthref.org/MagIC/19546. Data files in the common CIT format are also available from the authors upon request.

SI References

1. Kirschvink J (1980) The least-squares line and plane and the analysis of palaeomagnetic data. *Geophysical Journal of the Royal Astronomical Society* 62(3):699-718.
2. Heslop D & Roberts AP (2016) Analyzing paleomagnetic data: To anchor or not to anchor? *Journal of Geophysical Research: Solid Earth* 121(11):7742-7753.
3. Schmidt PW (2014) A review of Precambrian palaeomagnetism of Australia: Palaeogeography, supercontinents, glaciations and true polar wander. *Gondwana Research* 25(3):1164-1185.
4. Evins LZ, Jourdan F, & Phillips D (2009) The Cambrian Kalkarindji Large Igneous Province: Extent and characteristics based on new 40Ar/39Ar and geochemical data. *Lithos* 110(1-4):294-304.
5. Brenner AR*, et al.* (2020) Paleomagnetic evidence for modern-like plate motion velocities at 3.2 Ga. *Science Advances* 6(17):eaaz8670.
6. Bradley K, Weiss BP, & Buick R (2015) Records of geomagnetism, climate, and tectonics across a Paleoarchean erosion surface. *Earth and Planetary Science Letters* 419:1-13.
7. Li Z, Guo W, & Powell C (2000) Timing and genesis of Hamersley BIF-hosted iron deposits: a new palaeomagnetic interpretation. MERIWA Project M242. *Minerals and Energy Research Institute of Western Australia Report* 199:216.
8. Rasmussen B, Fletcher IR, & Sheppard S (2005) Isotopic dating of the migration of a low-grade metamorphic front during orogenesis. *Geology* 33(10):773-776.
9. Cawood PA & Tyler IM (2004) Assembling and reactivating the Proterozoic Capricorn Orogen: lithotectonic elements, orogenies, and significance. *Precambrian Research* 128(3):201-218.
10. Strik G, Blake TS, Zegers TE, White SH, & Langereis CG (2003) Palaeomagnetism of flood basalts in the Pilbara Craton, Western Australia: Late Archaean continental drift and the oldest known reversal of the geomagnetic field. *Journal of Geophysical Research: Solid Earth* 108(B12).
11. Evans D, Smirnov AV, & Gumsley A (2017) Paleomagnetism and U–Pb geochronology of the Black Range dykes, Pilbara Craton, Western Australia: a Neoarchean crossing of the polar circle. *Australian Journal of Earth Sciences* 64(2):225-237.
12. Schmidt P & Embleton B (1985) Prefolding and overprint magnetic signatures in Precambrian (~ 2.9–2.7 Ga) igneous rocks from the Pilbara Craton and Hamersley Basin, NW Australia. *Journal of Geophysical Research: Solid Earth* 90(B4):2967-2984.
13. Tauxe L & Watson G (1994) The fold test: an eigen analysis approach. *Earth and Planetary Science Letters* 122(3-4):331-341.
14. Biggin AJ*, et al.* (2011) Palaeomagnetism of Archaean rocks of the Onverwacht Group, Barberton Greenstone Belt (southern Africa): Evidence for a stable and potentially reversing geomagnetic field at ca. 3.5 Ga. *Earth and Planetary Science Letters* 302(3-4):314-328.
15. Van Kranendonk MJ (2008) *Structural Geology of the Central Part of the Lalla Rookh Western Shaw Structural Corridor, Pilbara Craton, Western Australia* (Geological Survey of Western Australia).
16. McFadden P & McElhinny M (1990) Classification of the reversal test in palaeomagnetism. *Geophysical Journal International* 103(3):725-729.
17. Doell RR (1970) Paleomagnetic secular variation study of lavas from the Massif central, France. *Earth and Planetary Science Letters* 8(5):352-362.
18. Cox A (1970) Latitude dependence of the angular dispersion of the geomagnetic field. *Geophysical Journal International* 20(3):253-269.
19. Watkins N (1973) Brunhes epoch geomagnetic secular variation on Reunion Island. *Journal of Geophysical Research* 78(32):7763-7768.
20. Smirnov AV, Tarduno JA, & Evans DA (2011) Evolving core conditions ca. 2 billion years ago detected by paleosecular variation. *Physics of the Earth and Planetary Interiors* 187(3-4):225-231.
21. Efron B (1982) *The jackknife, the bootstrap, and other resampling plans* (Siam).

22. Panzik JE & Evans DAD (2014) Assessing the GAD hypothesis with paleomagnetic data from large Proterozoic dike swarms. *Earth and Planetary Science Letters* 406:134-141.
23. Biggin AJ*, et al.* (2020) Quantitative estimates of average geomagnetic axial dipole dominance in deep geological time. *Nature Communications* 11(1):6100.
24. Glenn DR*, et al.* (2017) Micrometer-scale magnetic imaging of geological samples using a quantum diamond microscope. *Geochemistry, Geophysics, Geosystems* 18(8):3254-3267.
25. Lima EA & Weiss BP (2009) Obtaining vector magnetic field maps from single-component measurements of geological samples. *Journal of Geophysical Research: Solid Earth* 114(B6).
26. Volk MWR, Fu RR, Mittelholz A, & Day JMD (2021) Paleointensity and Rock Magnetism of Martian Nakhlite Meteorite Miller Range 03346: Evidence for Intense Small-Scale Crustal Magnetization on Mars. *Journal of Geophysical Research: Planets* 126(5):e2021JE006856.
27. Kouketsu Y*, et al.* (2014) A new approach to develop the R aman carbonaceous material geothermometer for low-grade metamorphism using peak width. *Island Arc* 23(1):33-50.
28. Froelich AJ & Gottfried D (1988) An overview of early Mesozoic intrusive rocks in the Culpeper basin, Virginia and Maryland. *US Geol Surv Bull* 1776:151-165.
29. Ragland PC & Arthur JD (1988) Element mobility during alteration of early Mesozoic diabase sheets, Culpeper basin, Virginia. *Studies of the early Mesozoic basins of the eastern United States. U*.
30. Sutter JF, Froelich A, & Robinson G (1988) Innovative approaches to the dating of igneous events in the early Mesozoic basins of the eastern United States. *US Geological Survey Bulletin* 1776:194-200.
31. mindat.org (Vulcan Materials Company Crushed Stone Quarry [Manassas Quarry], Manassas, Prince William Co., Virginia, USA). url: https://www.mindat.org/loc-15214.html.
32. Kylander-Clark AR, Hacker BR, & Cottle JM (2013) Laser-ablation split-stream ICP petrochronology. *Chemical Geology* 345:99-112.
33. Spandler C*, et al.* (2016) MKED1: a new titanite standard for in situ analysis of Sm–Nd isotopes and U–Pb geochronology. *Chemical Geology* 425:110-126.
34. Spencer K*, et al.* (2013) Campaign-style titanite U–Pb dating by laser-ablation ICP: Implications for crustal flow, phase transformations and titanite closure. *Chemical Geology* 341:84-101.
35. Aleinikoff JN*, et al.* (2007) Ages and origins of rocks of the Killingworth dome, south-central Connecticut: Implications for the tectonic evolution of southern New England. *American Journal of Science* 307(1):63-118.
36. Schmitz MD & Bowring SA (2001) U-Pb zircon and titanite systematics of the Fish Canyon Tuff: an assessment of high-precision U-Pb geochronology and its application to young volcanic rocks. *Geochimica et Cosmochimica Acta* 65(15):2571-2587.
37. Kennedy AK, Kamo SL, Nasdala L, & Timms NE (2010) Grenville skarn titanite: potential reference material for SIMS U–Th–Pb analysis. *The Canadian Mineralogist* 48(6):1423-1443.
38. Paton C*, et al.* (2010) Improved laser ablation U-Pb zircon geochronology through robust downhole fractionation correction. *Geochemistry, Geophysics, Geosystems* 11(3).
39. Ludwig K (2008) Isoplot version 4.15: a geochronological toolkit for microsoft Excel. *Berkeley Geochronology Center, Special Publication* 4:247-270.
40. Jaffey A, Flynn K, Glendenin L, Bentley Wt, & Essling A (1971) Precision measurement of half-lives and specific activities of U 235 and U 238. *Physical review C* 4(5):1889.
41. Stacey Jt & Kramers J (1975) Approximation of terrestrial lead isotope evolution by a two-stage model. *Earth and planetary science letters* 26(2):207-221.
42. Sambridge M & Compston W (1994) Mixture modeling of multi-component data sets with application to ion-probe zircon ages. *Earth and planetary science letters* 128(3-4):373-390.
43. Strik GHMA (2004) *Paleomagnetism of late Archaean flood basalt terrains: implications for early Earth geodynamics and geomagnetism* (UU Dept. of Earth Sciences).
44. McFadden PL & McElhinny MW (1990) Classification of the reversal test in palaeomagnetism. *Geophysical Journal International* 103(3):725-729.

45. McElhinny M & Senanayake W (1980) Paleomagnetic evidence for the existence of the geomagnetic field 3.5 Ga ago. *Journal of Geophysical Research: Solid Earth* 85(B7):3523-3528.
46. Van Kranendonk MJ, Smithies HR, Hickman AH, & Champion DC (2007) Review: secular tectonic evolution of Archean continental crust: interplay between horizontal and vertical processes in the formation of the Pilbara Craton, Australia. *Terra Nova* 19(1):1-38.
47. Buick R*, et al.* (2002) Geochronology and stratigraphic relationships of the Sulphur Springs Group and Strelley Granite: a temporally distinct igneous province in the Archaean Pilbara Craton, Australia. *Precambrian Research* 114(1-2):87-120.
48. Hickman AH (2021) East Pilbara Craton: a record of one billion years in the growth of Archean continental crust. (Geological Survey of Western Australia), p 187.
49. Wingate MTD, Kirkland CL, Bodorkos S, & Hickman AH (2010) 160258: felsic metavolcanic rock, Orchard Well. in *Geochronology Record 840* (Geological Survey of Western Australia), p 4.
50. Brauhart CW, Huston DL, & Andrew AS (2000) Oxygen isotope mapping in the Panorama VMS district, Pilbara Craton, Western Australia: applications to estimating temperatures of alteration and to exploration. *Mineralium Deposita* 35(8):727-740.
51. Johnson BW & Wing BA (2020) Limited Archaean continental emergence reflected in an early Archaean 18O-enriched ocean. *Nature Geoscience* 13(3):243-248.
52. Drieberg S (2003) The magmatic-hydrothermal architecture of the Archean volcanic massive sulfide (VMS) system at Panorama, Pilbara, Western Australia.
53. Martindale J, Hagemann S, Huston D, & Danyushevsky L (2014) Integrated stratigraphic–structural–hydrothermal alteration and mineralisation model for the Kangaroo Caves zinc–copper deposit, Western Australia. *Australian Journal of Earth Sciences* 61(1):159-185.
54. Vearncombe S*, et al.* (1995) 3.26 Ga black smoker-type mineralization in the Strelley belt, Pilbara craton, Western Australia. *Journal of the Geological Society* 152(4):587-590.
55. Layer PW, Kröner A, & McWilliams M (1996) An archean geomagnetic reversal in the Kaap Valley pluton, South Africa. *Science* 273(5277):943-946.
56. Moyen J-F, Stevens G, Kisters AF, Belcher RW, & Baptiste L (2019) TTG plutons of the Barberton Granitoid-Greenstone Terrain, South Africa. *Earth's Oldest Rocks*, eds Van Kranendonk M, Bennett V, & Hoffman J (Elsevier), 2 Ed, pp 615-653.
57. Layer PW, Lopez-Martinez M, Kröner A, York D, & McWilliams M (1998) Thermochronometry and palaeomagnetism of the Archaean Nelshoogte pluton, South Africa. *Geophysical Journal International* 135(1):129-145.
58. Tarduno JA, Cottrell RD, Watkeys MK, & Bauch D (2007) Geomagnetic field strength 3.2 billion years ago recorded by single silicate crystals. *Nature* 446(7136):657.
59. Layer PW, Kröner A, & York D (1992) Pre-3000 Ma thermal history of the Archean Kaap Valley puton, South Africa. *Geology* 20(8):717-720.
60. De Ronde CEJ, Hall CM, York D, & Spooner ETC (1991) LASER step-heating 40Ar39Ar age spectra from early Archean (~3.5 Ga) Barberton greenstone belt sediments: A technique for detecting cryptic tectono-thermal events. *Geochimica et Cosmochimica Acta* 55(7):1933-1951.
61. Hickman A (1984) *Archaean diapirism in the Pilbara Block, Western Australia* pp 113-127.
62. Zegers T, Nelson D, Wijbrans J, & White S (2001) SHRIMP U-Pb zircon dating of Archean core complex formation and pancratonic strike-slip deformation in the East Pilbara Granite-Greenstone Terrain. *Tectonics* 20(6):883-908.
63. Van Kranendonk MJ & Collins WJ (1998) Timing and tectonic significance of Late Archaean, sinistral strike-slip deformation in the Central Pilbara Structural Corridor, Pilbara Craton, Western Australia. *Precambrian Research* 88(1):207-232.
64. Wingate MT & Evans DA (2003) Palaeomagnetic constraints on the Proterozoic tectonic evolution of Australia. *Geological Society, London, Special Publications* 206(1):77-91.
65. Wingate MT & Giddings JW (2000) Age and palaeomagnetism of the Mundine Well dyke swarm, Western Australia: implications for an Australia–Laurentia connection at 755 Ma. *Precambrian Research* 100(1-3):335-357.
66. Wingate M (2017) Mafic dyke swarms and large igneous provinces in Western Australia get a digital makeover. *Geol. Surv. Western Australia Rec* 2:4-8.

67. Krása D, Shcherbakov VP, Kunzmann T, & Petersen N (2005) Self-reversal of remanent magnetization in basalts due to partially oxidized titanomagnetites. *Geophysical Journal International* 162(1):115-136.
68. Ozima M & Larson E (1968) Study of self-reversal of TRM in some submarine basalts. *Journal of geomagnetism and geoelectricity* 20(4):337-351.
69. Readman P & O'Reilly W (1972) Magnetic properties of oxidized (cation-deficient) titanomagnetites (Fe, Ti, □)3O4. *Journal of geomagnetism and geoelectricity* 24(1):69-90.
70. Jamieson JW*, et al.* (2013) Sulfide geochronology along the Endeavour Segment of the Juan de Fuca Ridge. *Geochemistry, Geophysics, Geosystems* 14(7):2084-2099.
71. Lalou C, Reyss JL, Brichet E, Rona PA, & Thompson G (1995) Hydrothermal activity on a 105-year scale at a slow-spreading ridge, TAG hydrothermal field, Mid-Atlantic Ridge 26° N. *Journal of Geophysical Research: Solid Earth* 100(B9):17855-17862.
72. McElhinny MW & McFadden PL (1997) Palaeosecular variation over the past 5 Myr based on a new generalized database. *Geophysical Journal International* 131(2):240-252.
73. Doubrovine PV*, et al.* (2019) Latitude Dependence of Geomagnetic Paleosecular Variation and its Relation to the Frequency of Magnetic Reversals: Observations From the Cretaceous and Jurassic. *Geochemistry, Geophysics, Geosystems* 20(3):1240-1279.
74. Clement BM (2004) Dependence of the duration of geomagnetic polarity reversals on site latitude. *Nature* 428(6983):637-640.
75. Tominaga M, Sager WW, Tivey MA, & Lee SM (2008) Deep-tow magnetic anomaly study of the Pacific Jurassic Quiet Zone and implications for the geomagnetic polarity reversal timescale and geomagnetic field behavior. *Journal of Geophysical Research: Solid Earth* 113(B7).
76. Fu RR, Kent DV, Hemming SR, Gutiérrez P, & Creveling JR (2020) Testing the occurrence of Late Jurassic true polar wander using the La Negra volcanics of northern Chile. *Earth and Planetary Science Letters* 529:115835.
77. Glenn D, LeSage D, Fu R, Weiss B, & Walsworth R (2015) Micron-Scale Magnetic Imaging of Meteorites and Early-Earth Rocks with NV Centers in Diamond. *APS Division of Atomic, Molecular and Optical Physics Meeting Abstracts*, p 1088.
78. Alt JC, Honnorez J, Laverne C, & Emmermann R (1986) Hydrothermal alteration of a 1 km section through the upper oceanic crust, Deep Sea Drilling Project Hole 504B: Mineralogy, chemistry and evolution of seawater-basalt interactions. *Journal of Geophysical Research: Solid Earth* 91(B10):10309-10335.
79. Schoneveld L*, et al.* (2020) Oxide-sulfide-melt-bubble interactions in spinel-rich taxitic rocks of the Norilsk-Talnakh intrusions, polar Siberia. *Economic Geology* 115(6):1305-1320.
80. Ahmed AH & Surour AA (2016) Fluid-related modifications of Cr-spinel and olivine from ophiolitic peridotites by contact metamorphism of granitic intrusions in the Ablah area, Saudi Arabia. *Journal of Asian Earth Sciences* 122:58-79.
81. Schrader E & Furbish W (1980) Mineralogy and geochemistry of ore minerals from basalts related to spreading centers of the eastrn Pacific with speculations on ore-forming processes, Initial Rep. *Deep Sea Drill. Proj* 54:789-806.
82. Shaar R & Feinberg JM (2013) Rock magnetic properties of dendrites: Insights from MFM imaging and implications for paleomagnetic studies. *Geochemistry, Geophysics, Geosystems* 14(2):407-421.
83. Shau YH, Torii M, Horng CS, & Peacor D (2000) Subsolidus evolution and alteration of titanomagnetite in ocean ridge basalts from Deep Sea Drilling Project/Ocean Drilling Program Hole 504B9 Leg 83: Implications for the timing of magnetization. *Journal of Geophysical Research: Solid Earth* 105(B10):23635-23649.
84. Wirsching U (1981) Experiments on the hydrothermal formation of calcium zeolites. *Clays and Clay Minerals* 29(3):171-183.
85. Ageeva O, Bian G, Habler G, Pertsev A, & Abart R (2020) Crystallographic and shape orientations of magnetite micro-inclusions in plagioclase. *Contributions to Mineralogy and Petrology* 175(10):1-16.
86. Ottens B*, et al.* (2019) Exceptional Multi Stage Mineralization of Secondary Minerals in Cavities of Flood Basalts from the Deccan Volcanic Province, India. *Minerals* 9(6):351.

87. Mattioli M, Cenni M, & Passaglia E (2016) Secondary mineral assemblages as indicators of multi stage alteration processes in basaltic lava flows: Evidence from the Lessini Mountains, Veneto Volcanic Province, Northern Italy. *Per. Mineral* 85:1-24.
88. Woodruff LG, Froelich A, Belkin HE, & Gottfried D (1995) Evolution of tholeiitic diabase sheet systems in the eastern United States: examples from the Culpeper Basin, Virginia-Maryland, and the Gettysburg Basin, Pennsylvania. *Journal of Volcanology and Geothermal Research* 64(3-4):143-169.
89. Rosenbauer RJ, Bischoff JL, & Zierenberg RA (1988) The laboratory albitization of mid-ocean ridge basalt. *The Journal of Geology* 96(2):237-244.
90. Hövelmann J, Putnis A, Geisler T, Schmidt BC, & Golla-Schindler U (2010) The replacement of plagioclase feldspars by albite: observations from hydrothermal experiments. *Contributions to Mineralogy and Petrology* 159(1):43-59.
91. Schiffman P, Elders W, Williams A, McDowell S, & Bird D (1984) Active metasomatism in the Cerro Prieto geothermal system, Baja California, Mexico: a telescoped low-pressure, low-temperature metamorphic facies series. *Geology* 12(1):12-15.
92. Rasmussen B & Buick R (2000) Oily old ores: evidence for hydrothermal petroleum generation in an Archean volcanogenic massive sulfide deposit. *Geology* 28(8):731-734.
93. Tice MM, Bostick BC, & Lowe DR (2004) Thermal history of the 3.5–3.2 Ga Onverwacht and Fig Tree Groups, Barberton greenstone belt, South Africa, inferred by Raman microspectroscopy of carbonaceous material. *Geology* 32(1):37-40.
94. Franklin J, Gibson H, Jonasson I, & Galley A (2005) Volcanogenic massive sulfide deposits. *Economic Geology 100th anniversary volume* 98:523-560.
95. Mueller WU*, et al.* (2008) Characterisation of Archean Subaqueous Calderas in Canada: Physical Volcanology, Carbonate-Rich Hydrothermal Alteration and a New Exploration Model. *Developments in Volcanology*, eds Gottsmann J & Martí J (Elsevier), Vol 10, pp 181-232.
96. Morton RL & Franklin JM (1987) Two-fold classification of Archean volcanic-associated massive sulfide deposits. *Economic Geology* 82(4):1057-1063.
97. Hudak GJ, Morton RL, Franklin JM, & Peterson DM (2003) Morphology, distribution, and estimated eruption volumes for intracaldera tuffs associated with volcanic-hosted massive sulfide deposits in the archean sturgeon lake caldera complex, Northwestern Ontario. *Explosive Subaqueous Volcanism, 2003*, (Blackwell Publishing Ltd), pp 345-360.
98. Wooldridge AL, Haggerty SE, Rona PA, & Harrison CG (1990) Magnetic properties and opaque mineralogy of rocks from selected seafloor hydrothermal sites at oceanic ridges. *Journal of Geophysical Research: Solid Earth* 95(B8):12351-12374.
99. Nagy L, Williams W, Tauxe L, & Muxworthy AR (2019) From nano to micro: evolution of magnetic domain structures in multidomain magnetite. *Geochemistry, Geophysics, Geosystems* 20(6):2907-2918.
100. Nagy L*, et al.* (2017) Stability of equidimensional pseudo–single-domain magnetite over billion-year timescales. *Proceedings of the National Academy of Sciences* 114(39):10356-10360.
101. Usui Y, Shibuya T, Sawaki Y, & Komiya T (2015) Rock magnetism of tiny exsolved magnetite in plagioclase from a Paleoarchean granitoid in the Pilbara craton. *Geochemistry, Geophysics, Geosystems* 16(1):112-125.
102. Van Kranendonk MJ (2000) *Geology of the North Shaw 1: 100 000 Sheets: Sheets 2755* (Geological Survey of Western Australia).
103. Zegers T, Wijbrans J, & White S (1999) 40Ar/39Ar age constraints on tectonothermal events in the Shaw area of the eastern Pilbara granite–greenstone terrain (W Australia): 700 Ma of Archean tectonic evolution. *Tectonophysics* 311(1-4):45-81.
104. Wijbrans JR & McDougall I (1987) On the metamorphic history of an Archaean granitoid greenstone terrane, East Pilbara, Western Australia, using the40Ar/39Ar age spectrum technique. *Earth and Planetary Science Letters* 84(2-3):226-242.
105. Collins W & Gray C (1990) Rb-Sr isotopic systematics of an Archaean granite–gneiss terrain: The Mount Edgar Batholith, Pilbara Block, Western Australia. *Australian Journal of Earth Sciences* 37(1):9-22.

106. Roberts NM & Tikoff B (2021) Internal structure of the Paleoarchean Mt Edgar dome, Pilbara Craton, Western Australia. *Precambrian Research* 358:106163.
107. Van Kranendonk M (2003) *Geology of the Tambourah 1: 100 000 Sheet [sheet 2754]* (Geological Survey of Western Australia).
108. Huston DL*, et al.* (2002) The timing of mineralization in the Archean North Pilbara terrain, Western Australia. *Economic Geology* 97(4):733-755.
109. Doyle MG & Allen RL (2003) Subsea-floor replacement in volcanic-hosted massive sulfide deposits. *Ore Geology Reviews* 23(3-4):183-222.
110. Gibson H, Morton R, & Hudak G (1999) Submarine volcanic processes, deposits, and environments favorable for the location of volcanic-associated massive sulfide deposits. *Reviews in economic geology* 8:13-51.
111. Hocker SM, Hudak GJ, & Heine JJ (2003) Electron Microprobe Analysis of Alteration Mineralogy at the Archean Five Mile Lake Volcanic Associated Massive Sulfide Mineral Prospect in the Vermilion District of Northeastern Minnesota.
112. Gifkins CC & Allen RL (2001) Textural and chemical characteristics of diagenetic and hydrothermal alteration in glassy volcanic rocks: Examples from the Mount Read Volcanics, Tasmania. *Economic Geology* 96(5):973-1002.
113. Kuznetsov V*, et al.* (2006) 230 Th/U DATING OF MASSIVE SULFIDES FROM THE LOGATCHEV AND RAINBOW HYDROTHERMAL FIELDS (MID ATLANTIC RIDGE). *Geochronometria: Journal on Methods & Applications of Absolute Chronology* 25.
114. Kirschvink JL, Ripperdan RL, & Evans DA (1997) Evidence for a large-scale reorganization of Early Cambrian continental masses by inertial interchange true polar wander. *Science* 277(5325):541-545.
115. Ricard Y, Doglioni C, & Sabadini R (1991) Differential rotation between lithosphere and mantle: A consequence of lateral mantle viscosity variations. *Journal of Geophysical Research: Solid Earth* 96(B5):8407-8415.
116. Rudolph ML & Zhong SJ (2014) History and dynamics of net rotation of the mantle and lithosphere. *Geochemistry, Geophysics, Geosystems* 15(9):3645-3657.
117. Becker TW (2006) On the effect of temperature and strain-rate dependent viscosity on global mantle flow, net rotation, and plate-driving forces. *Geophysical Journal International* 167(2):943-957.
118. O'Connell RJ, Gable CW, & Hager BH (1991) Toroidal-poloidal partitioning of lithospheric plate motions. *Glacial isostasy, Sea-level and mantle rheology*, (Springer), pp 535-551.
119. Herzberg C, Condie K, & Korenaga J (2010) Thermal history of the Earth and its petrological expression. *Earth and Planetary Science Letters* 292(1-2):79-88.
120. Wu F-Y, Yang J-H, Xu Y-G, Wilde SA, & Walker RJ (2019) Destruction of the North China Craton in the Mesozoic. *Annual Review of Earth and Planetary Sciences* 47(1):173-195.
121. Seton M*, et al.* (2012) Global continental and ocean basin reconstructions since 200 Ma. *Earth-Science Reviews* 113(3-4):212-270.
122. Foley BJ & Bercovici D (2014) Scaling laws for convection with temperature-dependent viscosity and grain-damage. *Geophysical Journal International* 199(1):580-603.
123. Moresi L & Solomatov V (1995) Moresi, L.-N. & Solomatov, V. S. Numerical investigation of 2D convection with extremely large viscosity variations. Phys. Fluids 7, 2154-2162. *Physics of Fluids* 7.
124. Solomatov VS (1995) Scaling of temperature- and stress-dependent viscosity convection. *Physics of Fluids* 7(2):266-274.
125. Korenaga J (2009) Scaling of stagnant-lid convection with Arrhenius rheology and the effects of mantle melting. *Geophysical Journal International* 179(1):154-170.
126. Karato S-i & Wu P (1993) Rheology of the upper mantle: A synthesis. *Science* 260(5109):771-778.
127. Katsura T, Yoneda A, Yamazaki D, Yoshino T, & Ito E (2010) Adiabatic temperature profile in the mantle. *Physics of the Earth and Planetary Interiors* 183(1):212-218.
128. Abbott D, Burgess L, Longhi J, & Smith WH (1994) An empirical thermal history of the Earth's upper mantle. *Journal of Geophysical Research: Solid Earth* 99(B7):13835-13850.

129. Dong J, Fischer RA, Stixrude LP, & Lithgow-Bertelloni CR (2021) Constraining the Volume of Earth's Early Oceans With a Temperature-Dependent Mantle Water Storage Capacity Model. *AGU Advances* 2(1):e2020AV000323.
130. Christensen U (1984) Convection with pressure- and temperature-dependent non-Newtonian rheology. *Geophysical Journal International* 77(2):343-384.